Electron Beam Tomography of Recording Head Fields

by Yan Liu

UNIVERSITY
of
GLASGOW

Submitted for degree of Doctor of Philosophy at the Department of Physics and Astronomy, University of Glasgow.

December 1996

ProQuest LLC.
789 East Eisenhower Parkway
P.O. Box 1346
Ann Arbor, MI 48106 – 1346

To my beloved Fei,

to our dear son Xiaoxiao

Contents

Acknowledgements

This thesis was enabled by a scholarship funded by the University of Glasgow and supplemented by the Overseas Research Student Award Scheme, whose support I acknowledge. This thesis also would not have been possible without the help of many others throughout the course of this work. Foremost I would like to thank Prof. R. P. Ferrier for his excellent supervision and help at all times during the last few years and Prof. J. N. Chapman for his encouragement and provision of the research facilities in the Solid State Physics Group at the University of Glasgow. I am grateful to Dr. S. McVitie for his assistance in learning to operate the JEOL 2000FX (S)TEM and to Dr. W. A. P. Nicholson for the design of the tomography rod.

Special mention should also be given to Drs. D. Heim and L. Nunnelley at IBM SSD, the former for making available model recording head field data and the latter for supplying us with the thin film heads. I am also grateful to Dr. H. van Kestern at Philips Research Laboratories and Dr. J. Zweck at the University of Regensburg for the provision of the tape head samples used in this thesis and many informative discussions. Profs Kubalek and Balk of the University of Duisburg are thanked for making available the computer code for the RTM method.

During the past three years there are many people who made my research at Glasgow a lot easier than it could have been, particularly I would like to thank Mr. A. Howie for maintaining the computer facilities and the network; Mr. S. Conner and the late Mr. J. Simms for maintaining the electron microscopes; Mr. I. Selkirk for the construction of the specimen rod and the specimen stubs.

Finally it remains for me to thank my wife Fei for her continual support during my study years.

Declaration

This thesis is a record of the work carried out by me in the Department of Physics and Astronomy at the University of Glasgow during 1993-1996. The work described herein is my own, apart from the Radon transform tomography program which was initially provided by colleagues at the University of Duisburg in Germany and was modified by Prof. R. P. Ferrier. Some of the work given in this thesis can be found in the following papers:

"Electron beam tomography of magnetic recording head fields"
R. P. Ferrier, Y. Liu, J. L. Martin, T. C. Arnoldussen
Journal of Magnetism and Magnetic Materials **149**, 387-397, (1995).

"Quantitative evaluation of a thin film recording head field using the DPC mode of Lorentz electron microscopy"
Y. Liu and R. P. Ferrier
IEEE Transactions on Magnetics, Vol. 31, No. 6, 3373-3375, (1995).

"Investigations on the stray-fields of magnetic read/write heads and their structural reasons"
Ingrid Petri, Tanja Zimmermann, Josef Zweck and H. Hoffmann
Yan Liu and Robert P. Ferrier
W. Nichtl-Pecher
Submitted to *IEEE Trans. Magn.*, (1996).

This thesis has not previously been submitted for a higher degree.

Summary

The quantitative evaluation of inductive recording head fields has been achieved by electron beam tomography. The differential phase contrast (DPC) mode of Lorentz microscopy implemented on a 200 kV scanning transmission instrument provides a novel technique for recording head field investigations and in particular the acquisition of the experimental data sets required for field reconstruction. The absolute determination of the recording head field has been obtained by calibration of the DPC image contrast.

This thesis starts with a brief discussion of the basics of ferromagnetism and the application of magnetic materials in magnetic recording technology. Development trends and some recent advances in magnetic recording head design are also discussed.

The second chapter gives a review of two dimensional techniques developed previously for magnetic stray field measurement and particular attention is given to the DPC Lorentz microscopy, since it is the experimental basis of 3D field characterisation by means of electron beam tomography.

The fundamental principles and the realisation of electron beam tomography for recording head field study are discussed in chapter 3. The two reconstruction algorithms of the RTM and the ART are introduced. The emphasis of this chapter is put upon the derivation of the magnetic field vector ART algorithm and the experimental implementation of the electron beam tomography using DPC Lorentz microscopy based on the modified JEOL 2000FX (S)TEM. The acquisition of the experimental data sets for tomographic reconstruction is also described in this chapter.

The ART tomography program described in chapter 3 is tested and compared with the RTM in chapter 4. The performance of the tomography programs are evaluated by simulation of DPC data sets for a model thin film head using different reconstruction parameters. It is confirmed by these simulations that the ART and the RTM can produce satisfactory reconstruction of recording head fields. Reconstructions using fewer projections by the ART and using truncated input data sets by the ART and the RTM

can still provide reasonable information on the major field distributions; this situation is encountered in practice. The computer simulations also provide information on the suitable reconstruction parameters which may be adopted in the experimental reconstruction of recording head fields.

In chapter 5 the electron beam tomography method is applied to study the stray field from inductive thin film heads. A novel method of mounting the thin film head for data collection makes it possible to reconstruct the stray field on a plane ~0.25 μm from the head gap. By etching part of the alumina present in the vicinity of the poletips, it has proved possible to identify magnetic flux leakage from regions of the poles, other than the polegap. The saturation behaviour of the writing field can also be obtained by studying the integrated stray field in the head gap direction for different dc driving currents.

Chapter 6 presents the experimental results from the study of the stray field from tape heads. The specimens used in this chapter are a pair of Metal-in-Gap write/ferrite read heads and laminated alloy film tape heads. Electron beam tomography and the DPC experiments can provide quantitative information on the stray field gradient and the half height of the field amplitude. The results obtained also show that DPC Lorentz microscopy is the most powerful tool to observe stray field defects, such as the secondary gap effect from the MIG head and the remanence effect from both the MIG and the laminated alloy film heads.

A method to calibrate the relative value of the DPC signal acquired from a quadrant DPC detector is described in chapter 7. The actual value of the electron beam deflection at certain point(s) on the DPC image is measured in-situ as part of the DPC experiment. From the calibration data set obtained, which is consistent with the theoretical analysis of the detector response, the absolute determination of the 3D stray field is achieved.

Conclusions and suggestions for further work are given in chapter 8.

Chapter 1

Ferromagnetism and magnetic recording

1.1 Ferromagnetic and ferrimagnetic materials

In a broad sense a magnetic substance is one which can be magnetised, to a greater or lesser extent, by a magnetic field. However only those which possess spontaneous magnetisation in the absence of the external field, such as ferromagnetic and ferrimagnetic materials, have found applications in the field of magnetics. Research on the performance of ferro- and ferrimagnetic materials are the basis of applied magnetics.

A ferromagnetic material has a magnetic dipole moment associated with each atom. This atomic magnetic moment results predominately from the spin of unpaired electrons in the 3d and 4f shells; the orbital angular momentum having been effectively quenched. This is why ferromagnetism is mainly found in transition metals and rare earths as well as their alloys. In a ferromagnetic material the spins lie parallel to one another as a result of a strong positive exchange interaction between the neighbouring spins as shown in Fig. 1.1.(a). Such an alignment of spins produces a resultant magnetisation, or spontaneous magnetisation (M_s). The ordered arrangement of the spins is disturbed by thermal agitation. With increasing temperature, the net magnetisation decreases until a critical point, known as the Curie point T_c, where the thermal (kT) effect becomes greater than the spin interaction and the system is disordered.

To explain the physical origin of ferromagnetism a molecular field theory was proposed [Weiss, 1907]. Each atomic moment is assumed to be acted on by a molecular field, which is proportional to the magnetisation of the environment. The internal molecular field is so strong that it results in a nearly perfect alignment of the spins in spite of the thermal agitation at room temperature. The Weiss molecular field is purely phenomenological. In quantum mechanical terms the energy associated with the

parallelism of the spin vectors will be determined by the overlap of the wavefunction and the resulting exchange interaction; this was described by Heisenberg [1928] as:

$$E_{ex} = -2JS_i \bullet S_j \tag{1.1}$$

Ferromagnetic materials are unusual in that the exchange integral J is positive so that the lower energy state is such that the spins S_i and S_j are parallel.

It is also possible for the spins to be antiparallel ($J<0$) and materials with this type of magnetic moment arrangement, with no net magnetisation, are termed antiferromagnetic. One modification of antiferromagnetism is named ferrimagnetism [Neel, 1948], in which the antiparallel moments are unbalanced either from unequal numbers of antiparallel spins or from the difference of the magnitude of the antiparallel spin moments. Examples of ferrimagnetic materials are ferrites, garnets and some other non-metallic materials. In ferrimagnetic materials the antiparallel spin moments come from different magnetic ions which occupy two kinds of sublattice sites, A and B. The magnetisations on site A and B point in opposite directions because of a strong negative interaction, known as the superexchange interaction, the difference between the two magnetisations gives rise to a net magnetisation as shown in Figure 1.1 (b). This spontaneous magnetisation is thermally disturbed with the increasing temperature and vanishes at a certain temperature, the Curie point T_c. The temperature dependence of ferrimagnetism is much more complicated than that of ferromagnetism, since there are at least two different magnetic ions involved.

(a) Ferromagnetism (b) Ferrimagnetism

Fig. 1.1. Schematic diagrams of the alignment of atomic moment at low temperature.

In spite of their spontaneous magnetisations, bulk ferro- and ferrimagnetic materials usually appear in a demagnetised state or even magnetically neutral. This is because the spontaneous magnetisation is subdivided into domains. Within each domain, the magnetisation is uniform and equal to saturation magnetisation M_s at that temperature, but different domains are magnetized in different directions. The average magnetisation of a specimen could therefore be much less than its M_s value and even zero. If an external field is applied, the domain magnetisation, as a whole, is attracted to the direction of the applied field and therefore a bigger average magnetisation is obtained. Spontaneous magnetisation and domain structures are the most fundamental properties of ferro- and ferrimagnetic materials.

1.2 Micromagnetic theory and magnetic domains

The spontaneous magnetisation and domain structures arise from a simple truth, a material will always seek to be in a state in which its potential energy is a minimum. It has been mentioned in section 1.1 that the spontaneous magnetisation of ferromagnetism is the result of minimisation of the exchange interaction energy between neighbouring atomic moments. However, the form of domain structure is the result of much more complicated energy consideration. The spontaneous magnetisation and the domain structure determine the magnetisation distribution in a magnetic material. In theory, various magnetisation distributions found in magnetic materials could be described mathematically by considering different energy contributions, which build up the total energy of the magnetic system. But even for the simplest magnetic object, rigorous mathematical treatment will make the problem unmanageable and simplifications have to be made.

On the atomic magnetic dipole scale Brown [1962] developed the micromagnetic method describing the effects of various energy constrains. The magnetisation in a magnetic material is defined as:

$$\boldsymbol{M} = M_s \sum_i \boldsymbol{m}_i^2 \tag{1.2}$$

in which M_s is the spontaneous magnetisation and $\boldsymbol{m}_i^2 = 1$ is the normalised dipole distribution, which defines the micromagnetic structure of the material. The principle of the micromagnetic theory is to determine all energy contributions, and minimise the resultant total energy with respect to the distribution of the magnetic dipoles. The following energy contributions have to be taken into account to work out the total energy of a magnetic system.

Exchange energy

The exchange energy of a magnetic material arises due to the deviation from parallel alignment of neighboring atomic dipoles and, for a cubic structure, is expressed as:

$$E_{ex} = A \int_V \left[(\nabla\alpha)^2 + (\nabla\beta)^2 + (\nabla\gamma)^2 \right] \tag{1.3}$$

where α, β, γ are the direction cosines with respect to the crystal axes and A is the exchange constant of the material given by,

$$A = \frac{kJS^2}{a} \tag{1.4}$$

in which k is a constant depending on the crystal structure (k = 1 for s.c., 2 for b.c.c. and 4 for f.c.c. lattices), a is the lattice constant. J and S are respectively the exchange integral and the magnitude of the atomic magnetic dipole. For a ferromagnetic material, J is positive and so is the exchange constant A. From equation (1.3) the exchange energy E_{ex} is a minimum when the atomic dipoles align parallel to each other and is therefore the phenomenon responsible for the spontaneous magnetisation of ferromagnetism.

Magnetostatic energy

A large amount of "free poles" will be created on the end surfaces if a magnetic specimen is uniformly magnetised. The free poles are also formed within the volume of the magnetic material where there are discontinuities or divergences of the magnetisation. Such free poles generate both the external stray field and the internal field. As the internal field is always in the opposite sense to the material magnetisation, it makes the magnetisation configuration unstable and hence it is called the demagnetising field. The magnetic potential V_m associated with the demagnetising field is calculated by integration over the volume and the surface of the field source as

$$V_m = \frac{1}{4\pi}\int_V \frac{-\nabla \bullet \boldsymbol{M}}{r} dV + \frac{1}{4\pi}\int_S \frac{\boldsymbol{M} \bullet \boldsymbol{n}}{r} dS \tag{1.5}$$

in which $\nabla \bullet \boldsymbol{M}$ and $\boldsymbol{M} \bullet \boldsymbol{n}$ are the volume and surface charge respectively and the demagnetising field is therefore given by

$$\boldsymbol{H}_d = -\nabla V_m \tag{1.6}$$

As described by Chikazumi (1964), the energy contribution due to the demagnetising field is called the magnetostatic energy and is given by

$$E_d = -\frac{1}{2}\mu_0 \int_V \boldsymbol{M} \bullet \boldsymbol{H}_d dV \tag{1.7}$$

where μ_0 is the permeability of free space. The most effective way to decrease the magnetostatic energy is to divide the magnetic specimen into domains. The free poles get less as the specimen is subdivided into more and more domains and even vanish on the surface when closure domain structures are present.

Anisotropy energy

Anisotropy arises from the crystalline nature of most magnetic materials. A magnetic material is anisotropic if it has preferred magnetisation direction(s), along which the specimen is much easier to magnetise; the preferred direction is called the easy axis.

The anisotropy energy has been demonstrated by measuring magnetisation curves in single crystal specimens. It is suggested by these results that the anisotropy energy depends on the direction of magnetisation relative to the crystal lattice.

For a magnetic material, like Fe, which has a body-centred cubic crystal structure, the anisotropy energy is well defined by the first two terms of a series expansion of the direction cosines,

$$E_k = \int_V \left[K_1\left(\alpha^2\beta^2 + \beta^2\gamma^2 + \gamma^2\alpha^2\right) + K_2\alpha^2\beta^2\gamma^2 \right] dV \tag{1.8}$$

where K_1 and K_2 are constants dependent on the material and temperature.

In an uniaxial crystal such as cobalt which has the hexagonal crystal structure, the anisotropy energy is given by

$$E_k = \int_V \left[K_1\left(1-\gamma^2\right) + K_2\left(1-\gamma^2\right)^2 \right] dV \tag{1.9}$$

which is mainly determined by the angle between the magnetisation and the uniaxial symmetry axis; K_1 and K_2 are again constants. Anisotropy energy explains certain orientations of domain magnetisation.

Magnetoelastic energy

There are distortions associated with the magnetisation of the magnetic specimen and the magnetoelastic energy is the result of the interaction between the magnetisation and the elastic distortions. When the magnetisation of a magnetic material is changed, the specimen will undergo a small fractional change in its shape, typically in the region of 10^{-5} (linear). The specimens either expand or contract in the direction of the magnetisation with increasing magnetisation and the materials with such elastic distortions are said to have positive or negative magnetostriction respectively. The inverse effect also exists such that the material becomes easier or harder to be magnetised along the direction to which a stress is applied. There is no simple

expression for the magnetoelastic energy, but the domain structures in some cubic materials can be qualitatively explained by considering the magnetoelastic energy.

Magnetic domains domain wall energy

Landau and Lifshitz (1935) suggested that the existence of magnetic domains is a consequence of the energy minimisation in a magnetic material. Before that date two important experimental observations had confirmed the existence of ferromagnetic domains. The first confirmation was the indirect detection of the domain motion through the Barkhausen effect [Barkhausen, 1919], in which the domain rotation caused discrete changes in magnetic induction within the ferromagnet. The Barkhausen effect leads to other discontinuities of bulk material properties if the measurement accuracy is high enough. The second confirmation was well known as the Bitter method [Bitter, 1931], in which the domain patterns in the surface of the material were demonstrated by applying magnetic fluid with suspended fine magnetic powder to the surface of the material. The most recent developments in magnetic domain observation focus on two techniques, laser magneto-optical microscopy (LAMOM) based on the Kerr effect and used for domain studies in magnetic recording heads [Argyle and Herman, 1986; Herman and Argyle, 1987] and Lorentz electron microscopy based on (scanning) transmission electron microscopy ((S)TEM) for thin film specimens [Chapman *et al.*, 1983, 1987, 1990].

As an example, Fig. 1.2 shows schematically the development of domains in a magnetic specimen, which is originally in the saturation magnetisation state, as it is demagnetised. In Fig. 1.2, the magnetisation distribution is divided into domains as a result of reducing the magnetostatic energy. If the loss in the magnetostatic energy is greater than the increase in the exchange energy and the anisotropy energy due to the formation of the domains, the magnetisation in the specimen will be subdivided into more domains until a minimum energy status is reached. Meanwhile, the magnetisation in the domain at room temperature is not equal to the saturation magnetisation as a result of the thermal activation; it reaches perfect alignment at 0°K and the alignment is random above the Curie point.

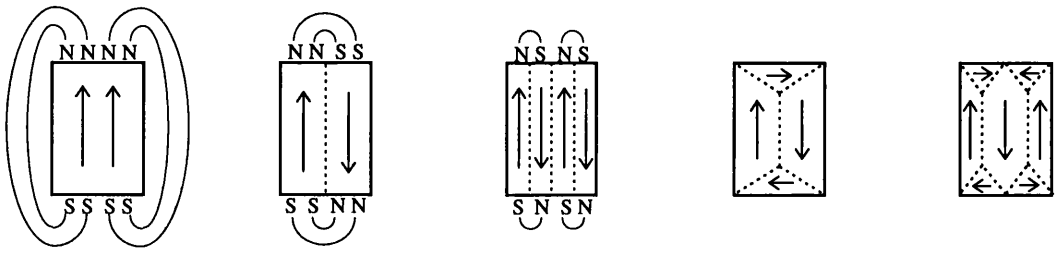

***Fig. 1.2.** Emergence of the domains as a result of the demagnetisation*

There is a transition region between domains, where the magnetic moments realign to minimise the associated energy increases. Domain wall energy, being a result of energy terms already considered, can be regarded as an independent energy term. The rotation of the magnetic moment in a domain wall produces an increase in exchange energy, depending on the type of wall, sometimes a magnetostatic energy. Magnetic anisotropy can also influence the domain walls, adding another contribution to the domain wall energy.

The realignment of the moments takes place over many atomic planes and this transition layer is called a domain wall. Most of the magnetic changes under the action of weak and moderate magnetic fields occur at the domain walls, the properties of which are very different from the rest of the domains. The occurrence of certain types of domain wall depend on the material properties. Fig. 1.3 shows some possible domain walls in thin film materials and the closure domains in cubic materials. The domains as demonstrated in Fig. 1.3.(a) are mainly the result of minimising the demagnetisation field, while in Fig. 1.3.(b) the domains tend to form 90° and 180° domain walls as the cubic anisotropy ensures that the directions at right angles to the magnetisation in a given domain are also magnetically easy axes, provided that the edges of the sample are along {100}. As an example, the magnetic moment transition in a Bloch wall is schematically illustrated in Fig. 1.4.

The equilibrium of the magnetisation distribution is determined by the minimisation of the total system energy in the magnetic material. Upon the application of the magnetic field, the external field energy E_H of the magnetic material is increased and the domain magnetisation will be aligned to the applied field direction to achieve a

new energy equilibrium, either by the rotation of domain magnetisation or by domain wall motion. Since no magnetic material is perfectly pure, there are strains and impurities which cause random potential energy fluctuations for domain wall motion or domain magnetisation rotation as shown schematically in Fig. 1.5. If the initial equilibrium is at x_0, the domain process is reversible only when the change of the domain structure is small (between *a* and *b*), otherwise the wall will not return to its original position x_0 after the applied field is removed. This irreversible process is called hysteresis in which the magnetisation of the magnet is the result of its magnetisation history and is fundamental to magnetic recording technology.

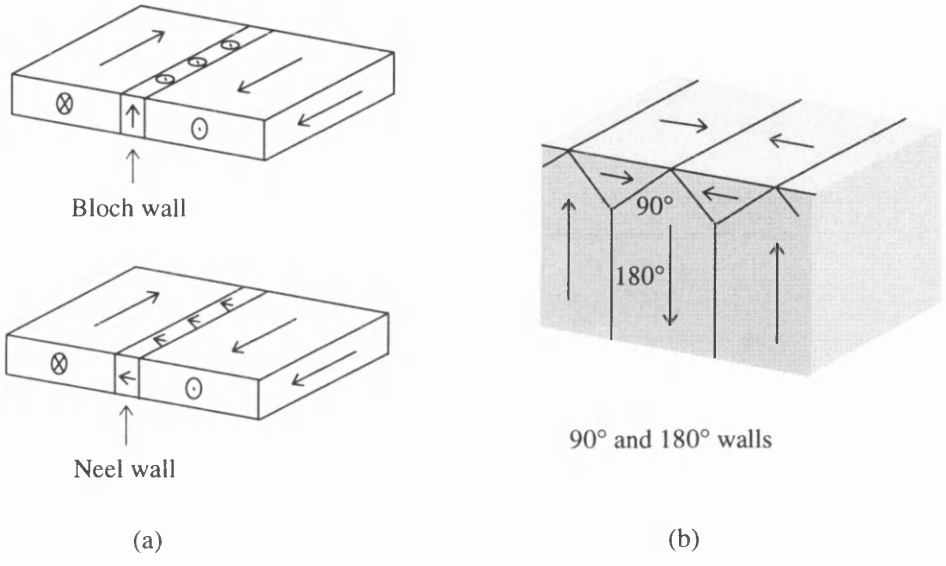

***Fig. 1.3**. Schematic of domains found in (a) magnetic thin films and (b) cubic materials.*

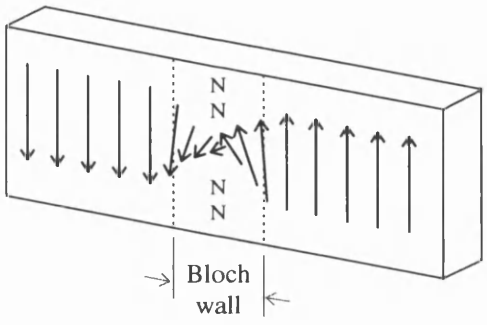

***Fig. 1.4**. Schematic diagram demonstrates the individual moment change in a Bloch wall.*

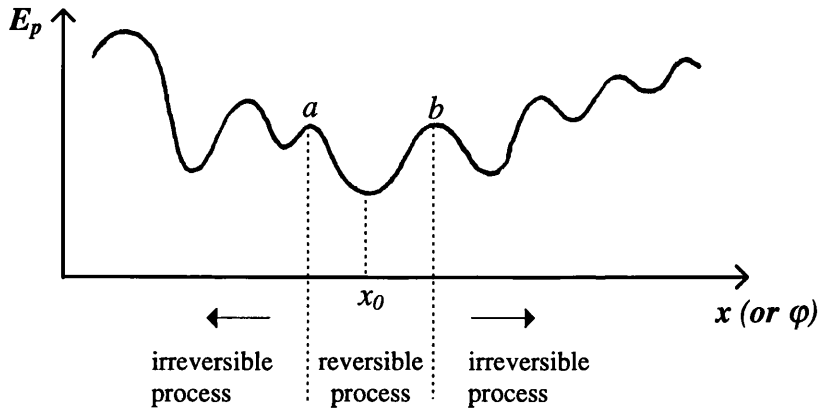

Fig. 1.5. Illustration of the potential energy as a function of distance or rotation angle seen by a magnetic domain wall movement, x_0 being the original position of the wall.

1.3 Magnetic recording

Magnetic recording is the central technology of information storage. For decades the magnetic storage industry has seen many breakthroughs under an unrelenting pressure to increase the amount and density of information which can be recorded using magnetic media. The combination of the inductive element and the magnetic recording media is still the main platform of this rapidly developed technology, and almost all the revolutions in recording density and data rate are the results of the minimisation of the inductive element and the evolution of magnetic materials for recording heads and media.

1.3.1 Magnetic recording materials

Magnetic materials may be evaluated by a VSM (vibrating sample magnetometer) measurement to determine the basic quantities of saturation magnetisation (M_s),

coercivity (H_c) and remanent magnetisation (M_r), which are defined in the saturation hysteresis loop as shown in Fig. 1.6. The hysteresis loop results from the irreversible magnetisation processes and is generated by first applying a saturating field in one direction that is large enough to align all the domain magnetisations to the direction of the applied field. The field is then reduced to zero, reversed and increased to saturation in the opposite direction. Sweeping the field in the opposite sense gives rise to a similar curve. The remanent magnetisation acts as a kind of memory of the last field maximum, both in magnitude and direction, experienced by the magnetic material. This hysteresis effect is used in magnetic recording technology to store information in digital form for computers and related devices, or in analog form in some audio and video signals recording.

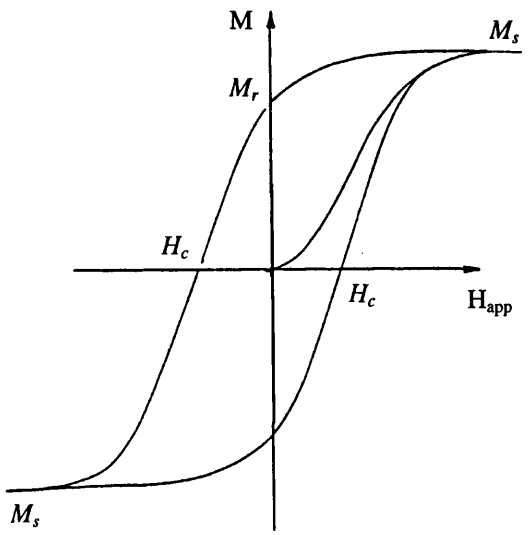

Fig. 1.6. *A typical hysteresis loop for a hard ferromagnetic material.*

The three quantities, M_s, M_r and H_c, provide the principal characterisation of a magnetic material, and determine the suitability of a ferromagnetic material for application in recording head or media fabrication. Another important property of ferromagnets, especially for use as soft magnets such as recording heads, is their high relative permeabilities. The permeability of a ferromagnet is not a constant as a function

of the magnetic field and the working frequency. Quantification of this property is rather difficult although it is defined in a simple form

$$\boldsymbol{B} = \mu_0 \mu_r \boldsymbol{H} \tag{1.10}$$

where μ_0 is permeability of free space and μ_r is the relative permeability of the material.

For applications as recording media, since the recorded information must be easily retrieved whenever necessary with minimum distortion, the materials must have sufficiently large coercivities to prevent the loss of or change to information due to extraneous fields. On the other hand, the coercivities have to be small enough to allow the materials to be erased and recorded by the recording head. The magnetic recording media ideally should have as a large saturation and remanence magnetisation as possible to provide a large signal during the reading process, especially with the increasing recording density achieved by scaling down the area of an information bit recorded on the media.

A recording head material must have high permeability and high saturation magnetisation to generate high magnetic induction for a given magnetic field and leave a large imprint on the media. The head must also have a low remanence to ensure that there is no writing when the current in the coil is zero. Other properties for head core material which must be considered include the electrical resistivity ρ, the thermal coefficient and the mechanical hardness [Mee and Daniel, 1987]. Suitable soft materials for recording head application include soft ferrites, Permalloy, Al-Fe (Alfenol), Al-Fe-Si (Sendust) and many recently developed alloys and amorphous materials.

1.3.2 Inductive recording heads

The recording process may easily be understood from the familiar inductive coil and magnetic core head design and an early 'ring head' for tape recording is illustrated in the simplified schematic in Fig. 1.7.

The writing process is accomplished by transferring the signal to be recorded, which is in electrical impulse form in the winding coil, into magnetised patterns on the storage medium. The electrical impulses generate magnetic field along the axis of the coil and the high permeability magnetic core guides the magnetic flux to a narrow head gap, where the flux emanates to form a stray field. The stray field from the head gap, which is proportional to the recording signal, magnetises the recording medium which passes in front of the head. Detailed analysis of the magnetisation in the medium is very difficult as the magnetic fields at different depths in the recording medium are different and the writing field is a function with time.

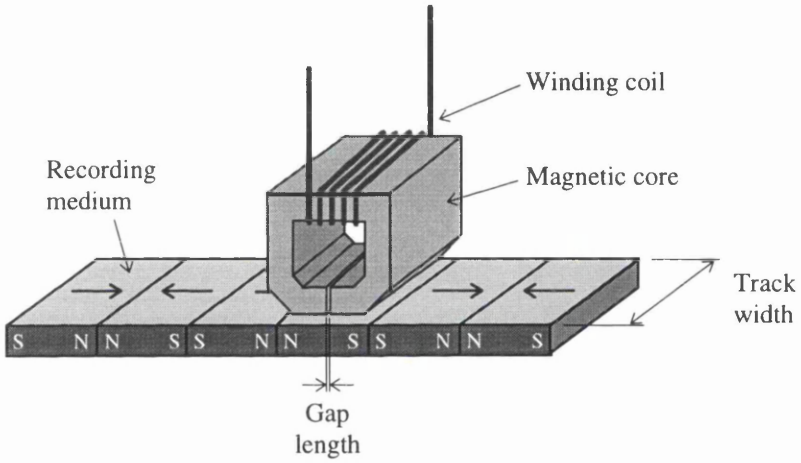

Fig. 1.7. *Schematic of the recording process of a ring head in tape recording.*

Recording heads are fabricated either with separated transducers to perform the write and read functions or with a shared inductive element for both functions. The reading process for both situations is essentially the same. The stray field which emanates from the magnetised medium after recording is representative of the recorded signal and the inductive head provides a low impedance path for the magnetic flux which passes in front of the head. The time change flux in the magnetic core threading the windings induces a voltage at the head terminals.

The magnetic stray field in the head gap region is the major concern in magnetic recording technology. The general trend has been to require smaller dimensions in gap length, track width, and core volume as recording densities and bandwidths have

increased. The evolution of materials for head cores and the introduction of thin film technology have had a significant influence on the fabrication process for head structures. Fig. 1.8 shows a head designed for high-data rate recording in a high density helical scan tape recorder [Ash, *et al.*, 1990], the gap length of which is sub micron (~0.25 μm), the gap width is between one and two orders of magnitude larger (~10-30 μm), and the head major dimensions are in the order of mm. The magnetic core in Fig. 1.8 is laminated parallel to the tape movement direction to allow for operation at frequencies ~150 MHz. Other tape head designs, commonly of the geometry shown in Fig. 1.8, include "Metal-in-Gap" heads for use on high coercivity media (Fe or metal evaporated tape) for video (8mm or DAT) or data recording [Jeffers, 1986; Iizuka, *et al.*, 1988].

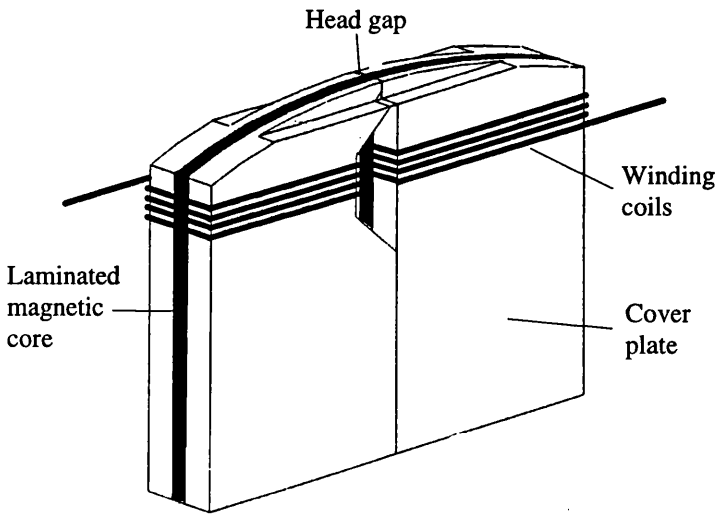

***Fig. 1.8.** A high data-rate, laminated magnetic core head for high density helical scan tape recorder (after Ash, et al. (1990)).*

In hard disk systems with 'flying' heads, thin film heads of permalloy predominate. These heads, as shown in Fig. 1.9, have head pole width ~5 μm and gap length ~0.2 μm, and are still under development to achieve narrower track width, reduced flying height, wider frequency response, and improved side-reading. Thin film heads can take advantage of high magnetisation alloy poles, high-frequency response of thin films and small inductance due to the small volume of magnetic core material. A

thin film head may be designed with suitable geometry in the polegap region to provide high write efficiency and high gap field approaching the saturation induction of the permalloy. It is now well known that if the domain structure in the poletip region is such that the domain magnetisation is parallel to the medium surface (and is therefore perpendicular to the magnetic flux from the recorded medium), as shown schematically in Fig. 1.10, the reading response is by domain magnetisation rotation rather than by domain wall motion. Hence a frequency response up to 100 MHz can be obtained [Kasiraj and Holmes, 1990].

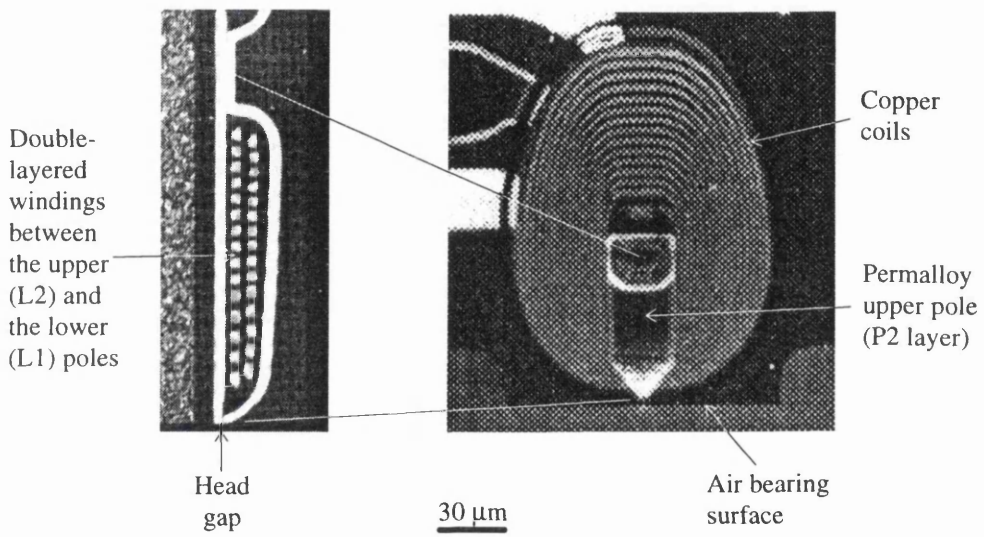

***Fig. 1.9**. Schematic of an inductive thin film head.*

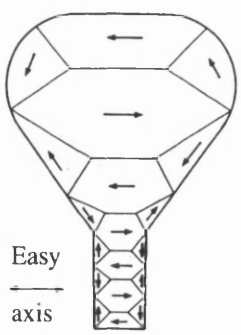

***Fig. 1.10**. Domain configuration in an inductive thin film head.*

1.3.3 Magneto-resistive heads

Disk recording technology has seen a ~60 % increase per year in areal density in the past five years. This has been made possible largely through the use of the magneto-resistive (MR) heads pioneered by IBM in 1991. Continuing to shrink the head gap geometry results in the reduction of the read back signal and consequently the inductive element design for reading becomes inadequate. An MR sensor, which exhibits a change in resistance in the presence of a magnetic field and works in a suitable biasing mode, can provide higher read sensitivity than inductive elements. In addition, the output of an MR sensor is proportional only to the magnetic flux and is independent of the head-disk velocity. This has favoured the recent shift to smaller disk diameters, which otherwise require more windings for an inductive element to read at a relatively low head-disk velocity. The basic design of the MR heads consists of separate read and write elements formed over each other and sharing a common material layer as shown in Fig. 1.11. The write element is a thin film inductive head. This optimised design is easier to realise than inductive heads which must perform both read and write functions, since it requires fewer copper coils, materials, photolithographic masking operations, and head-tolerance controls. The read element consists of an alloy film, usually NiFe, which exhibits the MR effect. Shielding layers protect the MR elements from other magnetic fields. The second shield also functions as one pole of the inductive write head. The first products by IBM using the MR technology have achieved an areal density of 0.132 Gbit/in^2 in 1991, and in 1996 IBM is shipping third-generation MR heads with areal density of 1 Gbit/in^2.

Advanced, high-areal-density heads will contain progressively thinner magnetic films and narrower MR elements. Head designers have avidly followed the recent discoveries in giant magneto-resistance (GMR) and spin valves (SV). These new materials allow MR heads to be scaled down to the very small dimensions needed for areal densities significantly greater than 1 Gbit/in^2 while maintaining good signal amplitude.

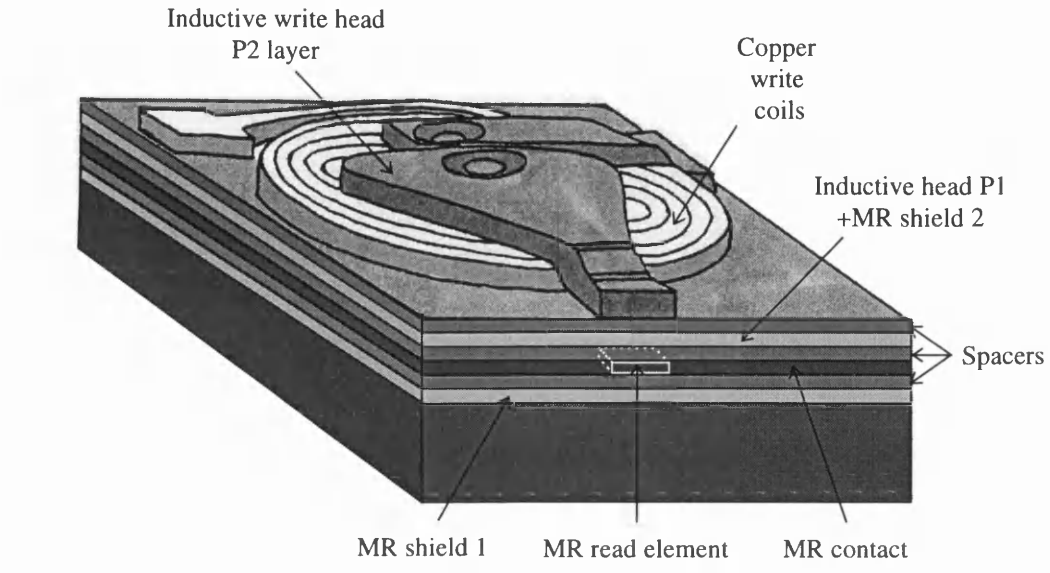

***Fig. 1.11**. Schematic of an merged magnetoresistive head.*

IBM has demonstrated data storage of three billion bits per square inch. There are however about 10 million billion atoms per square inch on the surface of the disk. Although thermal demagnetisation of the stored bits will ultimately limit the areal density attainable for room temperature magnetic storage, this limit is several orders of magnitude away from the present densities [Grochowski and Thompson, 1994]. In the foreseeable future, magnetic recording technology will still rely on the inductive element to write even smaller information bits on the media. The study of the stray field behaviour of the inductive head will eventually require an understanding of the micromagnetic structure in the vicinity of the poletips. This is beyond the ability of any current data modeling techniques as none of them are micromagnetic. However, electron probe techniques, witch have the high resolution and sensitivity, provide the suitable means to investigate the stray field of the write elements.

In this thesis, tomographic reconstruction methods based on Lorentz electron microscopy for recording head field study will be described and the experimental results of three dimensional stray field distributions of different inductive heads will be presented.

References

Argyle, B. and D. Herman (1986), *IEEE Trans. Magn.*, **22**, 772.

Ash, K. P. *et al.* (1990), *IEEE Trans. Magn.*, **26**, 2960-2965.

Barkhausen, H. (1919), *Physik Z.*, **20**, 401.

Bitter, F. (1931), *Phys. Rev.*, **38**, 1903.

Brown, W. F. (1963), "*Micromagnetics*", pubs. Interscience.

Chapman, J. N. and G. R. Morrison (1983), *J. Magn. Magn. Mater.*, **35**, 254-260.

Chapman, J. N., S. McVitie and I. R. McFadyen (1987), *Scanning Microscopy Supplement 1, Scanning Microscopy International, Chicago (AMF O'Hare),* 221-228.

Chapman, J. N., I. R. McFadyen and S. McVitie (1990), *IEEE Trans. Magn.*, **26**, 1506-1511.

Chikazumi, S. (1964), "*Physics of Magnetism*", John Wiley and Sons.

Grochowski, E. And D. A. Thompson (1994), *IEEE Trans. Magn.*, **30**, 3797-3800.

Heisenberg, W. (1928), *Z. Physik*, **49**, 619.

Herman, D. and B. Argyle (1987), *J. Appl. Phys.*, **61**, 4200.

Iizuka, M. *et al.* (1988), *IEEE Trans. Magn.*, **24** (6), 2623-2625.

Jeffers, F. (1986), *Proc. IEEE*, **74** (11), 1540-1556.

Kasiraj, P. and R. D. Holmes (1990), *IBM Res. Rept.* RJ-7805.

Kryder, M. (1985), *J. Appl. Phys.*, **57**, 3913.

Landau, L. and E. Lifshitz (1935), *Physik Z. Sowjetunion*, **8**, 153.

Mee, C. D. and E. D. Daniel (1987), *Magnetic Recording Vol. I: Technology*, McGraw-Hill.

Neel, L. (1948), *Ann. Physique* **3**, 137.

Weiss, P. (1907), *J. Phys.*, **6**, 661.

Chapter 2

Two dimensional methods for recording head field investigation

2.1 Introduction

The investigation of recording head fields is important for the characterisation of magnetic recording, as these fields influence the read/write properties of the recording system. This arises because the information density and the transfer velocity of the magnetic recording system are limited by the properties of the stray field caused by the magnetic structure of the recording head.

Several experimental techniques have been developed to attempt to measure the micromagnetic stray fields produced by magnetic recording heads. This chapter deals with the two dimensional techniques, in which only one or two components of the three dimensional magnetic field vector can be measured. The thrusts of the discussion are threefold. Firstly, a brief review of hitherto existing non-electron beam methods for stray field determination is given (section 2.2). Then, various modes of Lorentz microscopy utilising the scanning electron microscope (SEM) are introduced (section 2.3). Finally, the differential phase contrast (DPC) mode of Lorentz microscopy implemented on a modified JEOL 2000FX scanning transmission electron microscope (STEM) at Glasgow University is discussed in depth in section 2.4. The DPC Lorentz microscopy forms the experimental basis of this thesis for 3D field characterisation using the method of electron beam tomography.

In the study of recording head fields, two components are more important than the third, namely the component along the track direction $\boldsymbol{H_x}$ (the writing field for longitudinal recording) and the component normal to the head surface $\boldsymbol{H_y}$ (the writing

field for vertical recording mode). When the head gap length is much smaller than the gap width, the field component B_z , which is parallel to the gap width direction, and its variation along that direction are relatively small. An approximation of a two dimensional magnetic field ignoring B_z is therefore adequate. However, as the recording density increases, the recording head and its gap structure have to be made more and more compact and the two dimensional assumption becomes no longer acceptable. As a result a three-dimensional measurement is required to obtain a quantitative description of the head field and this will be introduced in chapter 3.

2.2 Review of non-electron beam techniques

The distribution of a micromagnetic field can be detected by utilizing various magnetic effects, such as Hall effect, magnetoresistive effect, electromagnetic induction and Lorentz force etc. The practicability depends entirely on the possibility of the miniaturisation of the sensor. The micro-sized sensors or probes using these magnetic effects convert the spatial distributed magnetic fields into relatively easily measured values like voltage, resistance, current or displacement of an electron probe.

Micro-sized Hall detector

The Hall detector has long been a traditional magnetic field measuring device. Because of the poor sensitivity, the detector has to be made relatively large, typically in the order of a few millimeters. Such a Hall detector can only be used in the situations of large-scale and slow-varying field distributions. To explore its micro-region application, one miniature Hall probe has been produced using a high accuracy fabrication method [Lustig *et al.*, 1979]. The active area of the Hall probe was 2×2 μm and it could be precisely positioned to a minimum separation of 1 μm from the surface of the measured object. Although this represents dramatic progress for the Hall probe technique, it is still inadequate for the decreasing dimensions of the recording head fields, where at least sub-micron resolution is required.

Magnetoresistive Transducers

Magnetoresistive transducers (MRT) are another form of sensor which can be used to measure the two dimensional micromagnetic stray fields. The essential requirements for the measurement system are the size of the MRT and a high precision positioner. Some preliminary work on the experimental equipment has been published [Fluitman, 1978; Fluitman and Groenland, 1979]. A more complete set up is shown in Fig. 2.1 [Groenland and Fluitman, 1981].

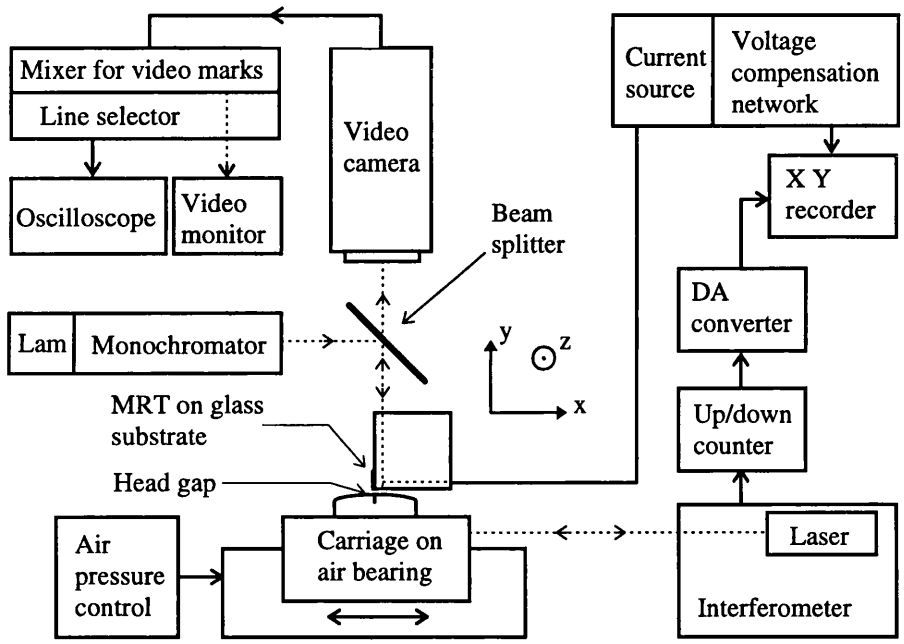

Fig. 2.1. *Scheme of the MRT measurement system (after Groenland & Fluitman, 1981)*

The MRT consists of a vacuum deposited permalloy strip and its typical dimensions are: length L = 50 μm; width w = 2.0 μm; thickness t = 0.02 μm. The MRT is placed at the edge of a glass substrate so that it can be positioned to face the two orthogonal field components $\boldsymbol{H_x}$ and $\boldsymbol{H_y}$ respectively. In this way the measurement of two-dimensional stray field is made possible.

To position the MRT and the measured head, an air bearing is used to adjust the separation between the transducer and the head surface. This separation is monitored

with the help of optical interference using monochromatic light. Either the MRT or the recording head can be set fixed, while the another one is positioned by a stepping motor (typically at 1 μm/s) and the displacement is measured by means of a Michelson-interferometer.

Compared to the Hall probe, the MRT has advantages in terms of sensitivity and ease of production. Even so the sensitivity of the MRT is proportional to the transducer current and this is limited by the heating effect of the transducer. The MRT is sensitive to magnetic field components which are in the plane of the permalloy strip. Perpendicular components are negligible due to the large demagnetising factor in this direction. Therefore, in Fig. 2.1, the sensor is also very sensitive to the field component H_z along the axis of the strip, which is parallel to the head gap direction. Unless the field component H_z is very small, one can not get a correct interpretation of the transducer response for H_x and H_y. For a recording head with very large gap width, H_z is negligible in the centre part of the gap. But with ever decreasing dimensions of the recording heads, this is no longer the case.

Inductive microloop

This is a relatively simple technique for direct measurement of the magnetic field from a recording head. It is also suited to investigations of the head performance at high frequencies. Again, the inductive loop has to be made small enough to afford decent spatial resolution of the magnetic flux. A high resolution inductive microloop developed by Hoyt *et al.* [1984] is shown in Fig. 2.2. The thin film microloop was produced by ion milling of Au-Ti film which had been evaporated onto a glass substrate, the masks for fabrication were produced by electron beam lithography. The finished dimensions of the sensor portion of the loop were 0.6 μm wide × 50 μm long × 0.2 μm thick. Such a sensor was applied to measure a ferrite head and a thin film head with gap lengths of 1.3 μm and 0.6 μm respectively.

A similar approach has been reported with slightly smaller sensor sizes to try to achieve higher spatial resolution in the x-axis direction [Brug *at el.*, 1988]. Electron beam lithography was used in conjunction with ion milling to construct the microloop from a 0.18 μm Au/Ti film. The finished sensor size was 0.3 μm wide and 0.18 μm thick.

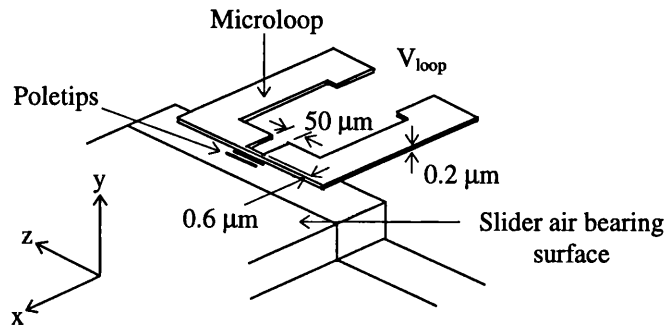

Fig. 2.2. Microloop positioned for inductive sensing of fields from a film head (not to scale) (Hoyt et al., 1984)

In Fig. 2.2, the thin film head under investigation is mounted onto a XYZ position stage. The height of the microloop above the ABS is adjusted by observing the interference fringes between the glass substrate and the ABS, which are at a small angle (0.4°) to each other. Movement of the head relative to the microloop is along x-axis direction. Therefore only perpendicular component $\boldsymbol{H_y}$ can be measured directly. For longitudinal recording, it is the field component $\boldsymbol{H_x}$ that couples to the magnetisation in the media. In the inductive microloop method, $\boldsymbol{H_x}$ is obtained from the measured $\boldsymbol{H_y}$ by means of Hilbert transform under the assumption that $\boldsymbol{H_z}$ is negligible. Thus it suffers the same disadvantage as the magnetoresistive technique.

2.3 Lorentz microscopy in a SEM

An electron beam can be focused by electromagnetic or electrostatic lenses to a very fine probe. As this charged probe passes through a magnetic field region, it will be deflected by the Lorentz force due to the interaction between the magnetic field and the moving electrons. The amplitude and direction of the electron beam deflection are related quantitatively to the components of magnetic field vector which are perpendicular to the electron beam trajectory. Therefore the integral of two dimensional micromagnetic stray fields along the electron trajectory can be inferred from the

measured deflections. Since it is possible to accelerate the electrons to very high energy and to control the beam current, the electron beam technique has the potential to achieve extremely high spatial resolution. The experiments are normally performed in commercially available scanning electron microscopes (SEMs) and are known by the general term Lorentz microscopy. In an SEM, the determination of the stray field distribution might be correlated directly to microscopic images of the magnetic structure by means of the magnetic contrast of backscattered electrons [Ferrier *et al.*, 1990]. This is a substantial advantage to understand the nature of the stray field, for the local domain structures will play an important role as the poletip dimensions of the head continue to shrink and the flight heights decrease.

The development of Lorentz microscopy technique for magnetic field measurement is associated with detecting the electron beam deflection. The electron beam deflection can be determined with the help of a reference grid [Thornley and Hutchison, 1969; Ishiba and Suzuki, 1974; Rau and Spivak, 1980; Wells and Brunner, 1983]. This method may be implemented in two forms as shown in Fig. 2.3. In the normal mode, shown in Fig. 2.3.(a), the incident electron beam passes through the head field to reach a reference grid placed below. The beam will be deflected by the head field. It hits the plane of the reference grid at a spot displaced from the position of incidence with no field present. This displacement of the beam will cause the image of the reference grid to appear distorted. The grid distortion vector is measured and the corresponding head field vector is calculated.

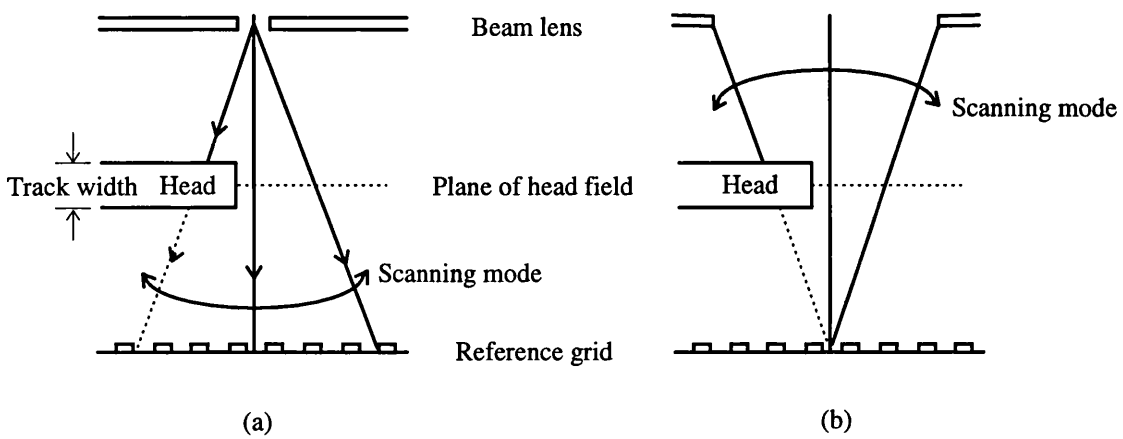

***Fig. 2.3.** Measurement of head fields in a SEM using (a) the normal mode and (b) the rocking mode (after Wells and Brunner, 1983)*

In the rocking mode as shown in Fig. 2.3.(b), the electron beam scans in such a way that it rocks about a fixed point on the reference grid. Therefore, in the absence of any head field, the beam strikes the same spot of the grid during the whole scanning cycle, giving rise to an image with constant intensity over the entire area. With a field present, the beam will be deflected and reach the plane of the reference grid at a point determined by its trajectory in the field region. The image shows a contour of equal field-times-distance integral, either for the total field or for a specified component of the field. If a rectangular reference grid is used and positioned properly with its sides parallel and normal to the head surface, as shown in Fig. 2.4.(a), the image reveals contours of constant H_x and H_y integral separately, shown in Fig. 2.4.(b).

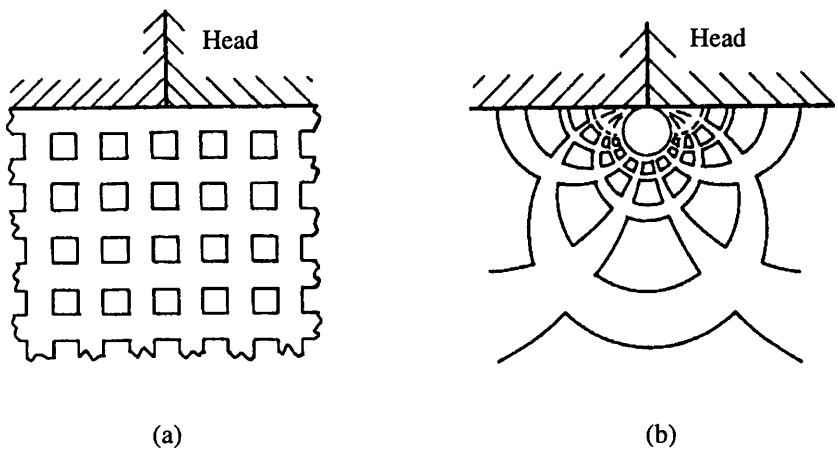

Fig. 2.4. *Distortion of (a) reference grid to produce a contour of constant x and y head field components (after Wells and Brunner, 1983)*

The spatial resolution of Lorentz microscopy can be improved by focusing the electron beam in the plane of specimen rather than in the reference plane [Rau, Spivak, 1980]. The image distortion methods can not result in direct interpretation of the components of the electron beam deflection.

By using a spatially resolving electron detector to sense the deflection of the beam, a fully automated experimental system may be set up as shown in Fig. 2.5

[Elsbrock and Balk, 1984]. This involves a microchannel plate (MCP) for locating the electron intensity distribution and a phosphor screen underneath it to convert the electron intensity to a light distribution. This is then collected by a TV-camera, a subsequent digital TV-frame memory and analysed by a process computer. Such a set up provides a real-time measurement of the two-dimensional stray field integral along the electron trajectory. Other benefits of this arrangement are that an electron beam chopper can easily be introduced to this system as shown in Fig. 2.5 by the broken line box [Elasbrock *et al.*, 1987]. This makes it possible to implement a stroboscopic technique to evaluate the dynamic magnetic stray fields up to 60 MHz with a time resolution of < 1 ns. Overall the sensitivity of this technique depends on the accelerating voltage, the camera length and the detector resolution.

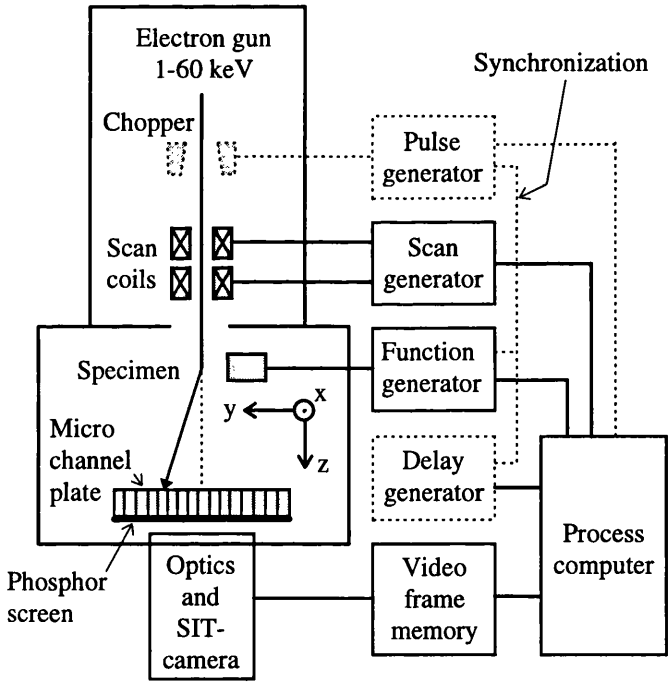

***Fig. 2.5.** Automated experimental set up for the static and the dynamic magnetic stray field determination (after Elsbrock and Balk, 1984; Elsbrock et al., 1987)*

For Lorentz microscopy, very careful sample preparation and adjustment of complex equipment are normally required. Most commonly, the specimen has to be coated with conductor (gold, aluminium or carbon) to prevent electrostatic charging. Therefore, in general, the Lorentz microscopy techniques are labor-intensive and time-consuming. This will be discussed in detail in chapter 5.

2.4 Differential Phase Contrast imaging in a STEM

In Lorentz microscopy, if the observed value is the phase shift of the electron wave rather than the deflection of electrons, this becomes the Differential Phase Contrast (DPC) mode. DPC microscopy was introduced by Dekkers and de Lang [1974, 1977] and subsequently applied to the study of magnetic domain structures by Chapman *et al.* [1983, 1987, 1990]. Because of its high resolution and linearity, it has also been developed for the study of recording head fields [Ferrier *et al.*, 1995; Liu and Ferrier, 1995].

The DPC mode of Lorentz microscopy is implemented on a scanning transmission electron microscope (STEM). The imaging principle of this mode can be explained classically (Fig. 2.6), although a quantum mechanical description is required for quantitative understanding of the electron-field interaction (section 2.4.2). In Fig. 2.6, electrons are focused to a small probe near the centre of the poletips of the recording head and are scanned over the area of interest. The incident electrons are deflected by the Lorentz force as they propagate through the field region. The deflection, in the term of Lorentz angle β_L, is proportional to the in-plane component of magnetic induction integrated along the electron trajectory. The detector used in this imaging mode is a circular detector, divided into four segments and positioned in the far field with respect to the specimen. The Lorentz angle β_L is determined by measuring the difference between the electrons falling on opposite segments of the quadrant detector. The descan facilities are used to excite a compensation field to ensure that in the absence of a recording head field (β_L=0) the electrons fall equally on all four segments

of the detector irrespective of the position of the electron beam during scanning. If the Lorentz angle β_L is much smaller than the probe semi angle α, a condition easy to realise in practice, the variation of the two differential signals provides direct information on the integrated spatial variation of the two orthogonal components of in-plane magnetic induction. In general, to ensure that the imaging system will respond linearly to the integrated induction, β_L/α has to be set to a value of about <0.1 [McFadyen and Chapman, 1992].

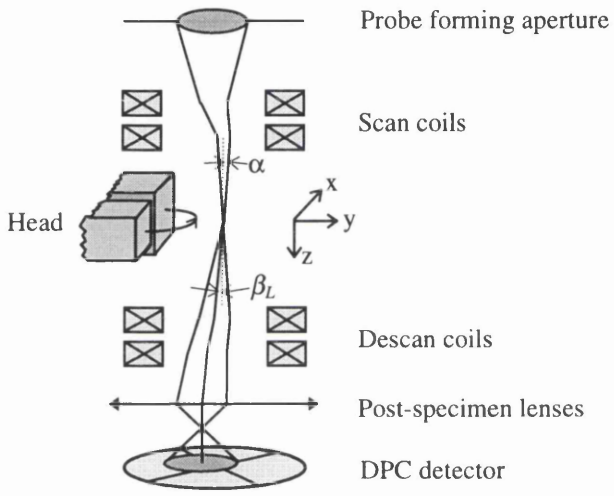

***Fig. 2.6**. Schematic of magnetic contrast generation for recording head field study in DPC Lorentz microscopy.*

2.4.1 Instrumental requirements and the modified JEOL 2000FX (S)TEM

To study the recording head fields using DPC Lorentz microscopy in a STEM, three major instrumental requirements have to be satisfied. Firstly, the STEM must be able to provide a small electron probe in the specimen region in the chamber of low (ideally zero) magnetic field. Secondly, the STEM must have a descan capability to ensure that

in the absence of a specimen equal numbers of electrons fall on each of the segments of the detector irrespective of the position of the probe in the scanning plane. Thirdly, post specimen lenses are needed to ensure that the electron distribution in the detector plane is matched to the fixed physical size of the quadrant detector.

All the DPC experiments detailed in this thesis in chapter 5, 6 and 7 were performed on a modified JEOL 2000FX (S)TEM. Fig. 2.7 shows the layout of this microscope with locations of coils and lenses, detectors, apertures etc. The principal features and modifications which are relevant to above mentioned requirements are discussed bellow.

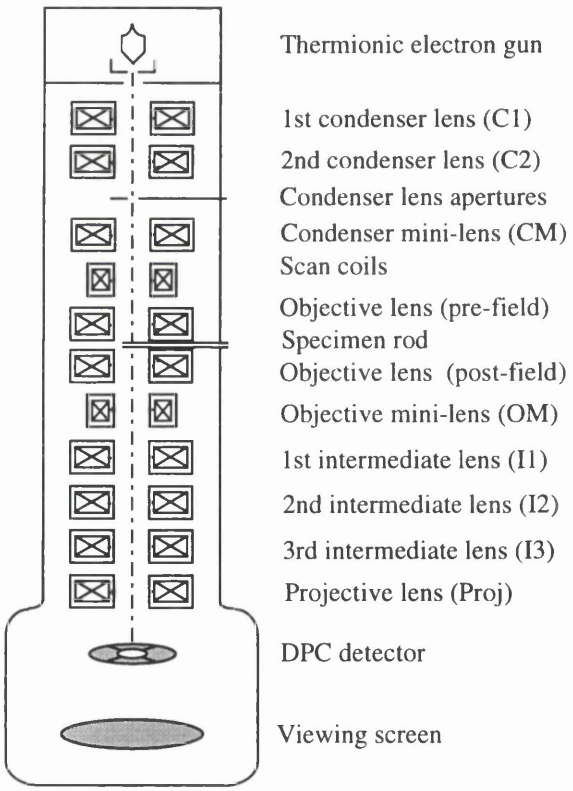

Fig. 2.7. *Layout of the JEOL 2000FX (S)TEM*

The JEOL 2000FX at Glasgow has a self-biased thermionic electron gun with precentred hairpin type tungsten (or LaB_6) filament. These thermionic sources,

compared with field emission electron guns, have relatively low brightness. This is considered a disadvantage for many applications where high brightness is desired. The thermionic sources do however have the advantage of improved beam current stability over field emission electron guns [Tuggle *et al.*, 1985; Troyon, 1987]. For recording head field studies, the area of interest is free space. Therefore the requirement for the gun brightness is less important. As will be noted in chapter 5, a full data set acquired in the STEM for tomographic reconstruction may take as long as a few hours and hence beam current stability is crucial to keep the experimental data self-consistent. The major drawback of the use of a thermionic electron gun is its relatively large beam cross-over diameter giving poor spatial resolution; even so a spatial resolution of 0.1 μm is still achievable as discussed in the following. This is suitable for the recording head field studies of current heads. For these reasons, the thermionic electron gun is a compromise choice.

The illumination of the specimen in the STEM is controlled by the condenser lenses, the condenser apertures and the pre-field of objective lens (Fig. 2.8). The condenser lens arrangement consists of a double-gap 1st condenser lens (C1), a 2nd condenser lens (C2) and a condenser mini-lens (CM). For a normal TEM/STEM microscope the specimen is located in the objective lens field, the amplitude of which is a significant fraction of one Tesla. This alters the magnetic structures of the specimen making any magnetic work impossible. At Glasgow the JEOL 2000FX has been built with an objective lens pole-piece assembly specially designed for magnetic microscopy [Tsuno and Inoue, 1984]. As shown schematically in Fig. 2.9, this assembly consists of three pole-pieces giving two lens gaps, both excited by the standard objective lens coils. The middle pole piece creates a magnetic shielded chamber, leaving the specimen inside it in effectively field free space. The pre-specimen gap allows a small probe to be focused on the specimen for STEM operation. In the present work, using the super focus mode (with CM lens switched off as in Fig. 2.8), a 40~50 nm probe can be obtained. This modification to the objective lens means that the performance suffers some losses for magnetic CTEM, STEM imaging [Craven *et al.*, 1993], but an essential requirement for DPC Lorentz microscopy, i.e. very low magnetic field in the specimen region, is satisfied.

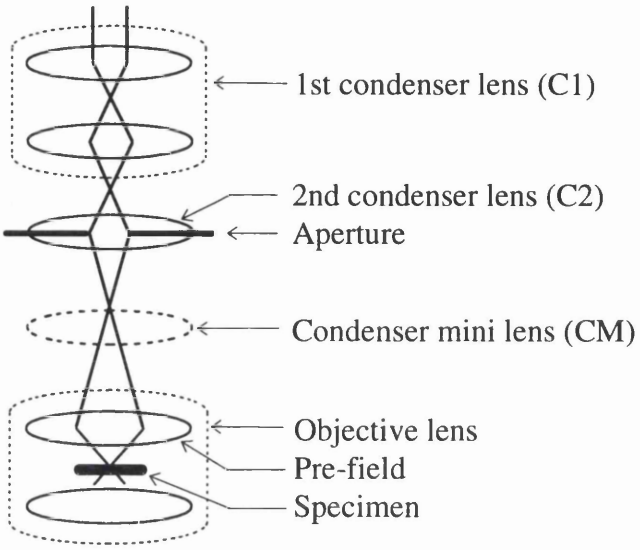

Fig. 2.8. *Ray diagram of the illumination system in JEOL 2000FX (S)TEM*

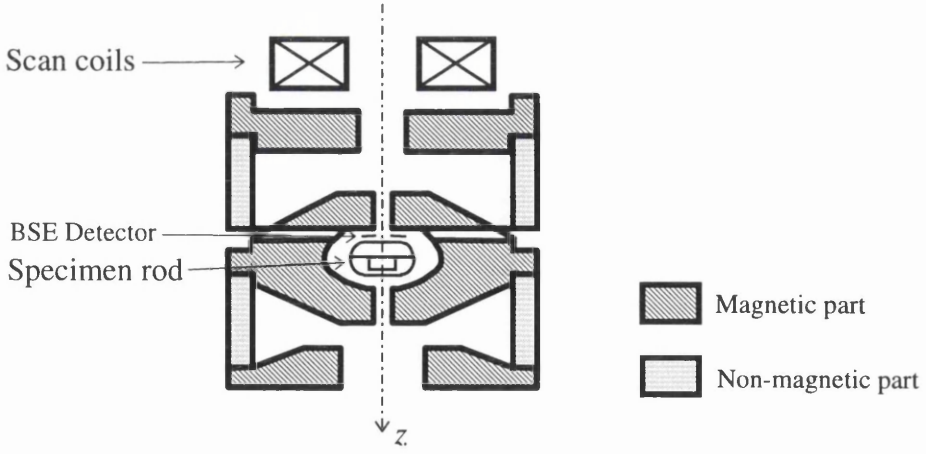

Fig. 2.9. *Schematic diagram of the specially designed objective lens pole-piece assembly for the JEOL 2000FX*

The image forming lens system of the STEM is composed of a 6-stage electromagnetic system with objective lens (post-field), objective mini (OM) lens, 1st, 2nd and 3rd intermediate lenses as well as projector lens. This provides a wide range of camera lengths or magnifications, which is important for DPC Lorentz microscopy

operation to obtain adequate size of the beam at the detector plane. The detector used in this work is an annular position sensor made from photodiodes. The detector is split into four segments with the inner and outer diameters of 9.2 mm and 18.2 mm respectively (Fig. 2.10). The size of the beam on the detector plane is set to ensure that in a full scanning cycle the maximum movement of the beam is restricted within the active detector area to avoid any signal discontinuities. This suggests, in Fig. 2.10, the spatial frequency vector $\boldsymbol{k_x}$ must fall in the range defined by the spot size and the detector geometry as

$$\left(k_{\alpha\max} - k_{\alpha 1}\right) \leq \left|\boldsymbol{k}_x\right| \leq k_{\alpha\max} \tag{2.1}$$

where $k_{\alpha max}$ and $k_{\alpha 1}$ are the outer and inner radii of the annular quadrant detector. In present work the size of the beam $k_{\alpha 2}$ is controlled by the first two intermediate lenses I1 and I2, while I3 is switched to zero and the projector lens is set to maximum excitation. This produces a camera length ~6m and is well suited for various head fields investigation. The response characteristic of such a DPC detector will be discussed in detail in chapter 7.

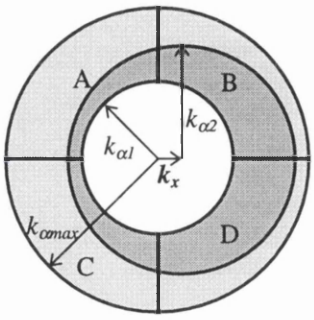

Fig. 2.10. *The geometry of the annular quadrant detector*

In addition, our JEOL 2000FX is fitted with a free lens current unit, external image shift unit and the external scan amplitude control. The lens current combinations for standard operations can be decoupled and hence all the lens currents may be

controlled independently. The JEOL 2000FX does not have descan coils. The balanced descan is achieved by fine tuning the scan amplitudes and the beam shift.

2.4.2 Wave-optical description of image formation in a STEM

The purpose of this section is to provide a brief discussion on DPC image formation in a STEM. This is achieved by analysing the propagation of the electron wavefunction through various stages of the electron-optical system and the electron-field interaction. The planes of interest are shown in Fig. 2.11.

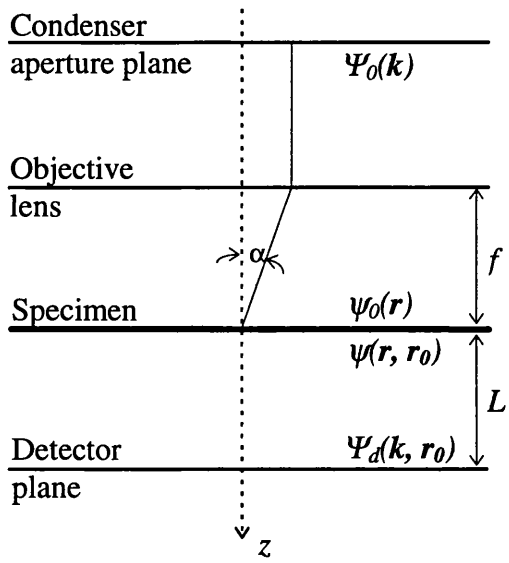

***Fig. 2.11.** Image formation in STEM*

We assume a plane-wave is incident on the condenser aperture plane and focused in the specimen plane. The wavefunction, considering the disturbance of the probe forming aperture and the aberration of the probe forming lens, can be written as

$$\Psi_0(\boldsymbol{k}) = A(\boldsymbol{k})\exp\left[-2\pi i\left(-\frac{C_s\lambda^3\boldsymbol{k}^4}{4}-\frac{\Delta z\lambda\boldsymbol{k}^2}{2}\right)\right] \tag{2.2}$$

where $\boldsymbol{k}$ is the position vector in the condenser aperture plane, $A(\boldsymbol{k})$ is the pupil function representing the condenser aperture which is unity within the aperture and zero elsewhere, C_s is the third order spherical aberration coefficient of the probe forming lens and Δz is the defocus of this lens.

On the specimen plane, the incident electron wavefunction can be expressed as a Fourier transform of the wavefunction at the probe forming aperture so that,

$$\psi_0(\boldsymbol{r}) = FT\left[\Psi_0(\boldsymbol{k})\right] \tag{2.3}$$

where FT denotes the Fourier transform and $\boldsymbol{r}$ is the position vector on the specimen plane.

As the beam passes through the stray field, the electron-field interaction introduces a transmission function $h(\boldsymbol{r})$ to define the electron wavefunction modulation due to the magnetic field. For a magnetic specimen, the amplitude contrast is negligible and the specimen can be treated as a pure phase object. The transmission function is therefore give by,

$$h(\boldsymbol{r}) = \exp\left[-i\phi(\boldsymbol{r})\right] \tag{2.4}$$

where $\phi(\boldsymbol{r})$ is the phase function which is defined by the thickness averaged induction components $\overline{\boldsymbol{B}}_{\perp}$ as [Chapman and Morrison, 1983],

$$\Delta\phi(\boldsymbol{r},\boldsymbol{r}_0) = -\frac{et}{h}\overline{\boldsymbol{B}}_{\perp} \tag{2.5}$$

in which $\boldsymbol{r}_0$ is the centre of the scanning probe, e is the electron charge, h is Planck's constant, t is the thickness of the field region.

A second Fourier transform gives the complex disturbance in the detector plane as,

$$\Psi_d(\boldsymbol{k},\boldsymbol{r}_0) = FT\left[\psi(\boldsymbol{r},\boldsymbol{r}_0)\right] \tag{2.6}$$

The signal on the detector plane can be obtained by taking the square modulus of the wavefunction (2.6) and considering the detector response ***R(k)***, the latter will be discussed in detail in chapter 7.

$$I(\mathbf{r}_0) = \int \left|\Psi_d(\mathbf{k},\mathbf{r}_0)\right|^2 R(\mathbf{k}) d\mathbf{k} \tag{2.7}$$

2.4.3 Imaging conditions for DPC Lorentz microscopy

To judge the performance of the DPC Lorentz microscopy for recording head field investigation, three quantities have to be discussed: the spatial resolution at the specimen plane, the linearity of the imaging system and the sensitivity of measuring the electron probe deflection. The discussions are based on the modified JEOL 2000FX, which is operated at 200 kV for all the DPC experiments described in this thesis.

The spatial resolution at the specimen plane is estimated approximately by the minimum electron probe diameter d_p, the probe broadening due to a certain probe semi angle α within the track width t of the head and the deflection of the probe by the stray field in terms of β_L as

$$R = d_p + t \cdot \tan\alpha + t \cdot \tan\beta_L \tag{2.8}$$

The minimum electron probe diameter d_p is limited by the size d_0 of the electron gun crossover, the spherical aberration of the probe forming lens which produces an error disc d_s, and the probe defining aperture which causes a diffraction error disc d_d as

$$d_p^2 = d_0^2 + d_d^2 + d_s^2 \tag{2.9}$$

The minimum electron probe diameter also depends on the probe current. Compared to normal specimen imaging in STEM, there is no need for large probe currents for studying stray fields and hence smaller probes are practical. In practice the JEOL 2000FX with a modified objective pole-piece for magnetic microscopy can provide probe diameters in the region 40~50 nm in field-free space.

The probe broadening is determined by the probe semi angle α, which is defined by the condenser aperture and examples are listed in Table. 2.1. The value chosen for α will depend on the Lorentz angle β_L of the specimen. The average Lorentz angle can be calculated from equation 2.5. Considering a typical thin film head with track width of ~5 μm and peak writing field of 0.5 T, the maximum Lorentz angle β_L is ~1.5 $\times 10^{-3}$ radian. It is believed that if the probe-semi angle α is set to a value ten times bigger than the Lorentz angle β_L, i.e., $\beta_L / \alpha < 0.1$, the linearity of the imaging system is satisfactory [McFadyen and Chapman, 1992]. However, for a strong phase object like a recording head field, this restriction can be relaxed simply by using a solid quadrant detector as opposed to annular type. In chapter 7 it is shown by analysing the response of the solid quadrant detector ($K=0$ in Fig. 7.3) that the imaging system can respond linearly to the integrated induction up to a value corresponding to $\beta_L/\alpha < 0.5$.

Table. 2.1.

Condenser aperture (μm)	Probe semi angle α (radian$\times 10^{-3}$)
200	7.2
120	4.7
70	2.7
40	1.4
20	0.7

In practice the probe semi angle α used is 4.7×10^{-3} radian (120 μm C2 aperture). For a typical thin film head with peak writing field of 0.5T and track width of ~5μm the spatial resolution at the specimen plane calculated from equation (2.8) is <0.1 μm.

The sensitivity to measure the electron probe deflection or the smallest stray field is limited by various measuring noises. DPC Lorentz microscopy has been successfully applied to study the magnetic domain structures in thin foils at Glasgow. For thin film samples typical Lorentz angles can be calculated from equation (2.5) and are in the region of 10^{-4} ~ 10^{-6} radian. Therefore for a typical thin film head as mentioned above a stray field of <10 Guess can be measured.

As an example, Fig. 2.12 shows a result of the measured integrated stray fields from a typical thin film head by using DPC Lorentz microscopy. In this case, the electron beam is parallel to the head gap (*z*-axis). Therefore the stray fields shown are the component in the track direction ($\boldsymbol{B}_x$) and the component normal to the ABS ($\boldsymbol{B}_y$). The component $\boldsymbol{B}_z$ is not measurable as the Lorentz force vanishes in this orientation.

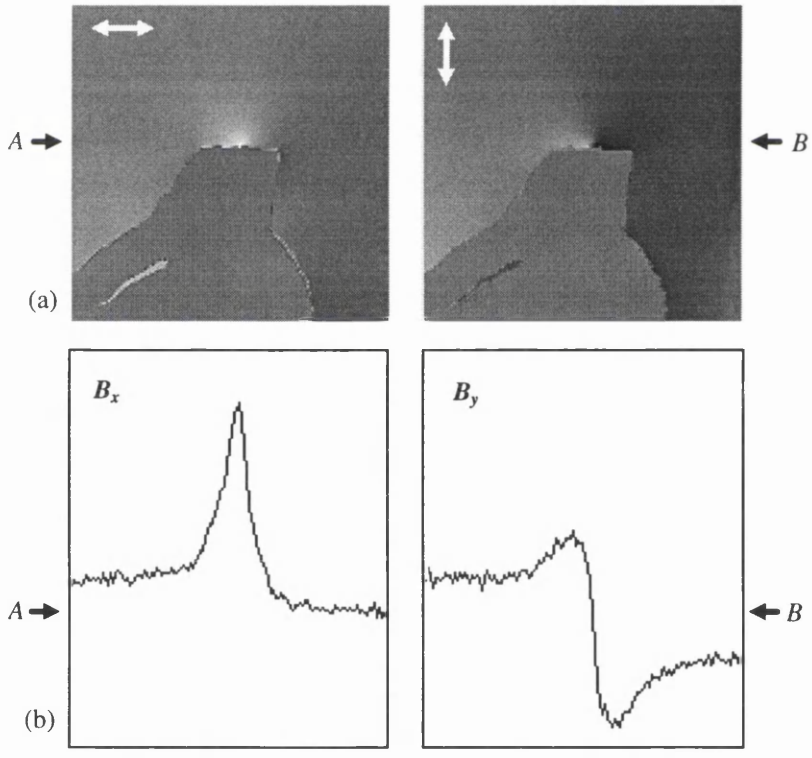

Fig. 2.12. *(a) The integrated stray fields measured by using DPC Lorentz microscopy, the mapping directions of the field components are indicated by the white arrows, (b) Line scans of the stray fields (a) taken in front of the head surface as indicated by the black arrows.*

2.5 Conclusion

The techniques which can be used to measure the magnetic recording head fields have been reviewed. Among them, the non-electron probe methods only provide spatial resolution in the micron range because of the difficulty of miniaturisation of the detectors. Lorentz electron microscopy results in much higher spatial resolution and it has the potential to achieve even higher resolution than currently demonstrated. Unlike the other modes of Lorentz microscopy, the DPC method can produce directly quantitative information on the stray fields. The DPC method has been discussed extensively in this chapter as it is the basis of all the DPC experiments described in this thesis. DPC Lorentz microscopy permits us to acquire the data sets necessary for the determination of the three dimensional recording head field and this will be discussed in next chapter.

References

Brug, J. A. *et al.* (1988), *J. Appl. Phys.* **63** (8), 4039-4041.

Chapman, J. N. and G. R. Morrison (1983), *J. Magn. Magn. Mater.*, **35**, 254-260.

Chapman, J. N., S. McVitie and I. R. McFadyen (1987), *Scanning Microscopy Supplement 1, Scanning Microscopy International, Chicago (AMF O'Hare),* 221-228.

Chapman, J. N., I. R. McFadyen and S. McVitie (1990), *IEEE Trans. Magn*, **26**, 1506-1511.

Craven, A. J., S. McVitie and J. N. Chapman (1993), *Microsc. Reseach and Technique* **24**, 316-332.

Dekkers, N. H. and H. de Lang (1974), *Optik* **30**, 452.

Dekkers, N. H. and H. de Lang (1977), *Philips Tech. Rev.* **37**, 1-9.

Elsbrock, J. B. and L. J. Balk (1984), *Scanning Electron Microsc. I, SEM Inc., AMF O'Hare (Chicago),* 131-139.

Elsbrock, J. B. *et al.* (1987), *J. Appl. Phys.*, **61**(8), 4185-4187.

Ferrier, R. P., Y. Liu, J. L. Martin, T. C. Arnoldussen (1995), *J. Mag. Magn. Mater.*, **149**, 387-397.

Ferrier, R. P., S. McVitie and W. A. P. Nicholson (1990), *IEEE Trans. Magn.* **26**, 1337-1339.

Fluitman, J. H. J. (1978), *IEEE Trans. Magn.* **14**, 433.

Fluitman, J. H. J. and J. P. J. Groenland (1979), *IEEE Trans. Magn.* **15**, 1634.

Groenland, P. J. and J. H. J. Fluitman (1981), *J. Phys.* E **14**, 503-508.

Hoyt, R. F. *et al.* (1984), *J. Appl. Phys.* **55** (6), 2241-2244.

Ishiba, T. and H. Suzuki (1974), *Jpn. J. Appl. Phys.*, **13**, 457-462.

Lazzari, J. P. and R. H. Wade (1971), *IEEE Trans. Magn.*, **MAG-7**, 700-704.

Liu, Y. and R. P. Ferrier (1995), *IEEE Trans. Magn.*, **31**, 3373-3375.

Lustig, C. D. *et al.* (1979), *Rev. Sci. Instrum.*, **50**, 321.

McFadyen, I. R. and J. N. Chapman (1992), *EMSA Bulletin*, **22:2**, 64.

Rau, E. I. and G. V. Spivak (1980), *Scanning*, **3**, 27-34.

Thornley, R. F. M. and J. D. Hutchison (1968), *Appl. Phys. Lett.*, **13** (8), 249.

Thornley, R. F. M. and J. D. Hutchison (1969), *IEEE Trans. Magn.*, **MAG-5**, 271.

Troyon, M. (1987), *J. Microsc. Spectrosc. Electron.* **12**, 431.

Tsuno, K. and M. Inoue (1984), *Optik*, **67**, 363-376.

Tuggle, D. W., J. Z. Li and L. W. Swanson (1985), *J. Microsc.* **140**, 293.

Wells, O. C. (1985), *J. Microsc.*, **139**, Pt2, 187-196.

Wells, O. C. and M. Brunner (1983), *Appl. Phys. Lett.* **42** (1), 114-116.

Chapter 3

Fundamentals of electron beam tomography for the study of recording head fields

3.1 Instruction

Tomography is the term for the method used to reconstruct the interior of an object from its projections. Electron beam tomography, as the term suggests, is the technique which employs an electron microscope to collect the projections and uses these projections to reconstruct the object of measurement in its entirety. Electron beam tomography emerged some 25 years ago for three-dimensional imaging of non-crystalline biological structures, like ribosome and chromosomes [DeRosier and Klug, 1968; Gordon *et al.*, 1970]. The development of electron tomography is associated with the evolution of computers in the past decades, since computers make it possible to deal with a vast amount of data in an acceptable processing time. The 3D reconstruction of biological structures are derived from the projections of their density variations. These projections are acquired using transmission electron microscopy (electron tomography) or x-ray computerised axial tomography (CAT-scan imaging), the difference of these two lies only in the different radiation and detectors used.

Electron beam tomography of magnetic recording head fields arises from the requirement to characterise the 3D features of head fields to help achieve even higher areal density and data rate of magnetic recording systems. This work was pioneered by a research group in Duisburg [Elsbrock *et al.*, 1985; Steck *et al.*, 1990]. The most significant modifications of electron beam tomography for recording head field study are the mathematics of reconstruction and the techniques to acquire electron beam deflection data sets. Unlike the scalar density function of a biological specimen, the

magnetic field is a three-dimensional vector. The projection of a magnetic field in electron beam tomography is a planar vector, it takes the form of the electron beam deflection, which results from the electron-field interaction and is integrated along the electron beam trajectory (Lorentz microscopy).

The Duisburg group carried out their approach by using a scanning electron microscope (SEM) to collect the electron beam deflection data and a reconstruction algorithm based on the Fourier and Radon transforms [Radon, 1917]; we will refer to this as the Radon Transform Method (RTM). The beauty of this algorithm is that either component of the deflection data permits an independent determination of all three components of the field vector. Later, Matsuda and his co-workers [1990] were engaged in a similar determination in the SEM of deflection data sets for recording head field reconstruction. Their algorithm was based on the Algebraic Reconstruction Technique (ART), which was originally established by Gordon *et al.* [1970] for the 3D imaging of biological structures, but modified to deal with a vector rather than a scalar function. The major advantage of the ART is that it can produce considerable detail of the object of measurement with fewer projections, therefore an ordinary tilting stage (say ±30°) may be used.

At Glasgow, we have developed our own version of the ART algorithm, and the projections of the head fields are acquired in a STEM using DPC Lorentz microscopy [section 2.4]. The purpose of this chapter is to give a detailed introduction to the general principle, the mathematical description and the experimental implementation of electron beam tomography for the evaluation of recording head fields. Both RTM and ART methods will be discussed, but the emphasis will be put upon the ART as it is the basis of our algorithm used throughout this thesis.

3.2 The general principle of 3D reconstruction

In principle, the 3D reconstruction is achieved by reducing the problem from three dimensions to two to make the problem tractable; the measured values in two-dimensional space are then used to synthesise the 3D object . Two methods, Fourier and

Algebraic Reconstruction Techniques (ART) have been employed to deconvolve the interior of an object from its projections. As they are different in principle and have gained practical importance in electron tomography, they will be discussed separately. We start from the basic scalar forms of the algorithms in density electron beam tomography, in which a density function is appropriate to define the object of measurement. The derivation of the tomographic algorithms for vector magnetic field will then be introduced in section 3.3.

3.2.1 The Fourier method

The Fourier transform provides an alternative representation of an object by breaking it down to a series of trigonometric basis functions. For the convenience of mathematical treatment, complex exponential functions of form $exp(-2\pi i\boldsymbol{k}\boldsymbol{r})$ are used instead of sine and cosine functions. The argument $\boldsymbol{r}=(x, y, z)$ is the position vector of the object and the argument $\boldsymbol{k}$ is the so-called spatial frequency, which gives the direction of the electron wave and its inverse wavelength. The object $f(\boldsymbol{r})$ is built up from such waves by linear superposition as

$$f(\boldsymbol{r}) = \sum_i F(\boldsymbol{k}_i) \exp\left(-2\pi i \boldsymbol{k}_i \boldsymbol{r}\right) \tag{3.1}$$

In this discrete form of the Fourier transform the complex coefficient $F(\boldsymbol{k}_i)$ contains information on the amplitude A_i and the phase (or phase shift with respect to the origin) ϕ_i of the associated wave as

$$A_i = \left|F(\boldsymbol{k}_i)\right| \tag{3.2}$$

$$\phi_i = \arctan\frac{\mathrm{Im}\{F(\boldsymbol{k}_i)\}}{\mathrm{Re}\{F(\boldsymbol{k}_i)\}} \tag{3.3}$$

In turn, $F(\boldsymbol{k}_i)$ can be written in discrete form of the inverse Fourier transform of $f(\boldsymbol{r})$ as

$$F(\boldsymbol{k}_i) = \sum f(\boldsymbol{r}) \exp(2\pi i \boldsymbol{k}_i \boldsymbol{r}) \tag{3.4}$$

We then obtain a pair of functions f and F. One of the most important results relating f and F to each other is the so-called central section theorem, which states that the Fourier transform of a 2D projection image is equal to a central section of the 3D Fourier transform of the object [Crowther *et al.*, 1970]. Thus the measurement of the projection offers a way to acquire the Fourier transform of the object. Fig. 3.1 shows how the object of measurement is retrieved by inverse Fourier transformation from a series of central sections through the origin of Fourier space superimposed on an array of equally spaced sampling points.

It can be seen that the samplings on the central sections become more widely separated with the distance from the centre. To ensure that their maximum separation is consistent with the reconstruction resolution required, the angular spacing of the projections must be close enough to prevent information loss. If the resolution of the measurement is set to a value d, the region in Fourier space in which the data must be acquired will be a sphere of radius $1/d$. This sphere must be bigger than the size of the reconstructed object D, i.e., $1/d>D$. Hence the minimum number of the equally spaced projections has to be [Bracewell and Riddle, 1967; Crowther *et al.*, 1970]

$$N = \frac{\pi D}{d} \tag{3.5}$$

3.2.2 The Algebraic Reconstruction Techniques

In the Algebraic Reconstruction Technique (ART), the object under investigation is defined as a spatially distributed density function. Using a tilt stage, we can rotate the object around a single axis. An incident radiation wave, e.g. an electron beam in a

microscope, is scanned across the object in such a manner that it creates a sectional plane through the object, perpendicular to the rotate axis. The interaction between the electron beam and the object projects into a line on the detector plane as shown in Fig. 3.2. We may reconstruct each section in turn from the projections in different views and combine these sections to get the three-dimensional reconstruction. Thus the problem of measurement is reduced from three dimensions to two.

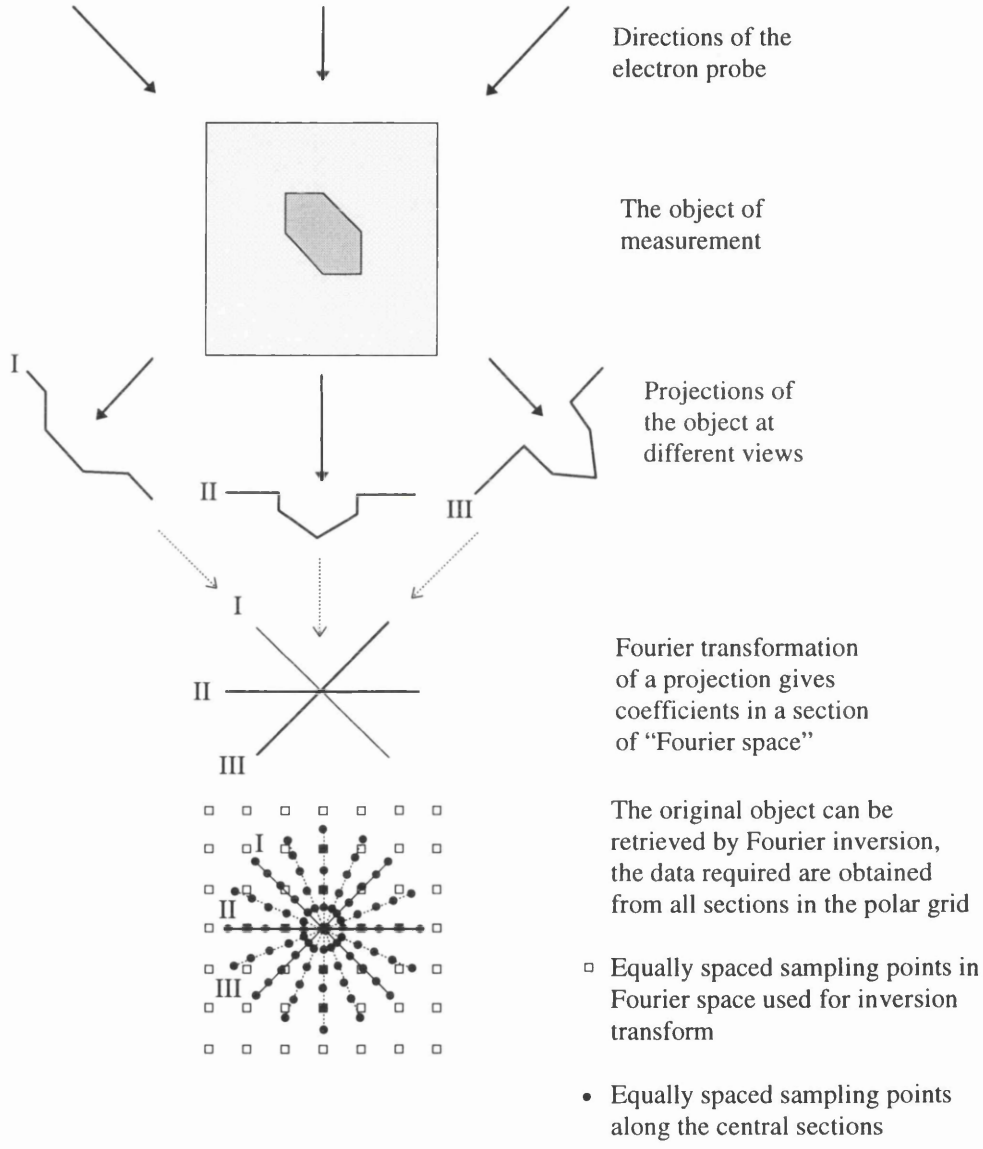

Fig. 3.1. *Schematic illustration of the 3D reconstruction using Fourier method.*

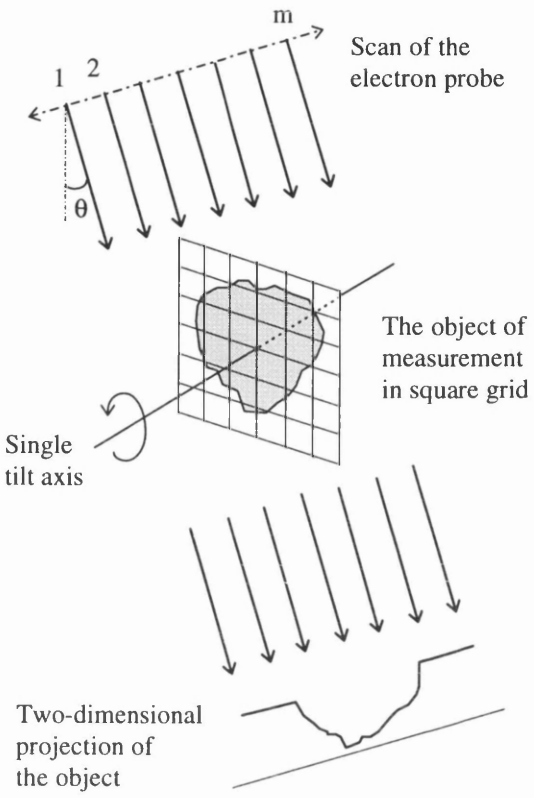

Fig. 3.2. *The incident radiation wave projects the three-dimensional object onto the detector plane.*

In Fig. 3.2, suppose the density function of the object is distributed in a square grid and we are satisfied with the reconstruction resolution of $n \times n$ points within the square. Thus the task is to find the density p_{ij} of the object at each point (i, j), $i, j=1, 2, \ldots, n$, associated with the grids. A electron beam ray penetrating the square with a incident angle θ will intersect a subset of the discrete points. The projection of the ray therefore has to be written as a distribution of these discrete points in the reconstruction. Each of the projection gives rise to a set of linear equations

$$R_{k\theta} = \sum_{(i,j)\in ray(k,\theta)} p_{ij} \qquad k=1, 2, \ldots, m \qquad (3.6)$$

in which m is the number of the rays in a given projection at angle θ. If m is set to be the same as the number n of the grid in a row and the number of different incident angles is

m_θ, we will have $m_\theta \times n$ linear equations of form (3.6) in the n^2 unknown p_{ij}. In general, the number of different incident angles is much smaller than the number of points in a row, i.e., $m_\theta << n$ ($m_\theta \times n << n^2$). Therefore equation (3.6) is highly underdetermined and the number of possible solutions is infinite.

The equation (3.6) does contain a certain amount of information about the three-dimensional structure of the object. The question is how to find a solution which is close enough to the real structure. Many iterative procedures may be applied according to the nature of the problem, and they have a simple intuitive basis: each projected density is fed back into the higher dimensional region from where it came (e.g. from 1D to 2D or 2D to 3D), with repeated corrections to bring each estimated projection into agreement with the corresponding measured projection. The reliability of reconstruction and computing efficiency are matters of utmost concern.

As the mathematics of the algorithm is intimately connected to the nature of the problem, we will present a detailed discussion of the ART algorithm associated with the representation of the recording head field in next section.

3.3 The realisation of 3D reconstruction of recording head fields

After the introduction of the fundamental principles of the 3D reconstruction algorithms, we discuss their application and realisation for recording head fields. The RTM is the first technique to be employed for the 3D determination of the magnetic stray field. Profs. Kubalek and Balk of the University of Duisburg have kindly provided us their computer code for the RTM method and we have adapted it to run on modern mainframe and UNIX platforms [Ferrier *et al.*, 1995]. We will give a brief introduction to their algorithm in section 3.3.1. The iterative procedure of our ART algorithm for recording head field reconstruction is based on the conventional ART. Therefore an introduction of the conventional ART algorithm will be presented in section 3.3.2, followed by the representation of the micromagnetic stray field in a modified iterative fashion (section 3.3.3).

3.3.1 The Radon transform method

We assume that a magnetic recording head is characterised within the Cartesian coordinate system shown in Fig. 3.3. The stray field from the polegap of the head is measured on the plane ∂G, which is the x-z plane and at a distance $y=-a$ from the ABS of the head. In the magnetic source free half space Ω ($y>0$), the magnetic induction $\boldsymbol{B}$ and the magnetic field strength $\boldsymbol{H}$ are described by the Maxwell equations as [Jiles, 1991]

$$\nabla \times \boldsymbol{H} = 0 \tag{3.7}$$

$$\nabla \cdot \boldsymbol{B} = 0 \tag{3.8}$$

and $\boldsymbol{B}$ and the $\boldsymbol{H}$ are related by

$$\boldsymbol{B} = \mu_0 \boldsymbol{H} \tag{3.9}$$

where μ_0 is the permeability of free space. Because of (3.7), the magnetic field can be described by a scalar magnetic potential Φ.

$$\boldsymbol{H} = -grad\Phi \tag{3.10}$$

and

$$\nabla^2 \Phi = 0 \tag{3.11}$$

with equations (3.7) ~ (3.11) and the theory of harmonic functions, the magnetic field in Ω can be written as an integral over the plane ∂G as

$$\boldsymbol{B}(\boldsymbol{r}) = \frac{1}{2\pi} \iint_{\partial G} \frac{\boldsymbol{r} - \boldsymbol{r}_0}{|\boldsymbol{r} - \boldsymbol{r}_0|^3} \boldsymbol{B}_y(\boldsymbol{r}_0) dS \tag{3.12}$$

in which $\boldsymbol{r}$ and $\boldsymbol{r}_0$ are position vectors in Ω and ∂G.

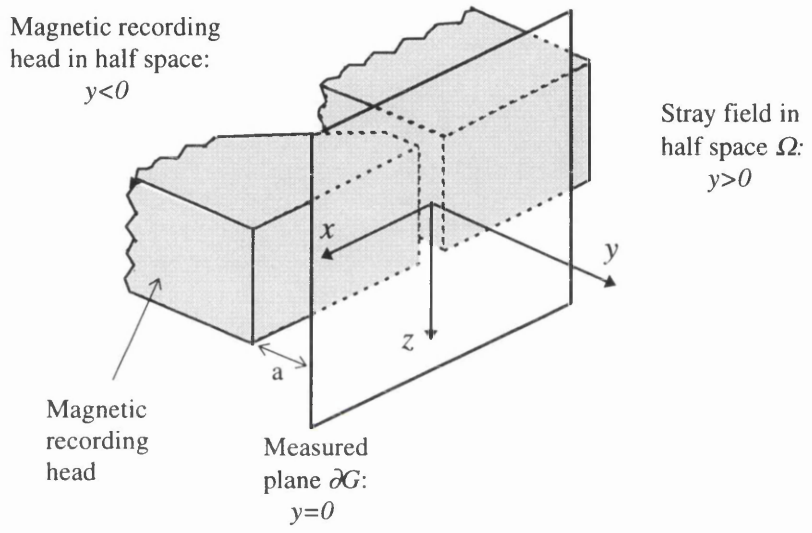

Fig. 3.3. *Model for the representation of the space of the magnetic stray field*

Applying two-dimensional Fourier transform (FT_2) to equation (3.12), we get equation (3.13) with the help of Fourier tables [Bracewell and Riddle, 1967]

$$FT_2\{\boldsymbol{B}(\bullet, y)\}(\boldsymbol{k}) = \left(-i\frac{\boldsymbol{k}}{|\boldsymbol{k}|} + \boldsymbol{e}_3\right) e^{-2\pi y|\boldsymbol{k}|} \cdot FT_2\{\boldsymbol{B}_y(\bullet,0)\}(\boldsymbol{k}) \tag{3.13}$$

where the symbol • represents the argument (in this case $\boldsymbol{r}$) relative to which the transform was performed. $\boldsymbol{k}$ is the two-dimensional spatial frequency vector and $\boldsymbol{e}$ is the unit vector along y axis. By (3.13) the magnetic field in Ω (i.e. $\boldsymbol{B}(\bullet, y)$, $y>0$) can be deduced if the values of the normal component ($\boldsymbol{B}_y(\bullet, 0)$) in ∂G is known.

Multiplication of equation (3.13) with an arbitrary unit vector in ∂G

$$\boldsymbol{e}(\theta) = \boldsymbol{e}_1 \cos\theta + \boldsymbol{e}_2 \sin\theta \tag{3.14}$$

leads to equation (3.15), where θ is the rotation angle about the normal axis y.

$$FT_2\{\boldsymbol{B}(\bullet, y)\}(\boldsymbol{k}) = \frac{\boldsymbol{k} + i|\boldsymbol{k}|\boldsymbol{e}_3}{\boldsymbol{k} \cdot \boldsymbol{e}(\theta)} \cdot e^{-2\pi y|\boldsymbol{k}|} \cdot FT_2\{\boldsymbol{e}(\theta) \cdot \boldsymbol{B}(\bullet,0)\}(\boldsymbol{k}) \tag{3.15}$$

With the aid of (3.15) a determination of the magnetic field $\boldsymbol{B}$ in Ω is attainable if the spectra of an arbitrary tangential component of the field in the plane ∂G is known. Therefore, the knowledge of the spectra, either of the normal or an arbitrary tangential component of the magnetic stray field in the measuring plane ∂G is sufficient to determine the stray field in the whole magnetic source free half space Ω.

The two-dimensional Radon transform of a function $f(\boldsymbol{r})$ is defined as [Ludwig, 1966]

$$RT_2\{f(\boldsymbol{r})\}(p, \boldsymbol{e}(\theta)) = \iint_{\Re^2} f(\boldsymbol{r}) \cdot \delta(p - \boldsymbol{r}\boldsymbol{e}(\theta)) d^2\boldsymbol{r} \tag{3.16}$$

in which p and $\boldsymbol{e}(\theta)$ together define a straight line ($p=\boldsymbol{r}\cdot\boldsymbol{e}(\theta)$), and only along this line is the Dirac delta function not equal to zero. Hence $RT_2\{f(\boldsymbol{r})\}(p,\boldsymbol{e}(\theta))$ is the integral of $\boldsymbol{f}$ along the line ($p=\boldsymbol{r}\cdot\boldsymbol{e}(\theta)$). In Lorentz microscopy (section 2.3) the electron beam is deflected by the component of the magnetic field perpendicular to the electron beam trajectory and the total deflection is obtained by integrating this field component along the electron beam trajectory. If the electron beam scans in the plane ∂G in front of the recording head and the corresponding electron beam deflection is small compared to the length of the electron beam trajectory, the measurement of the electron beam deflection in Lorentz microscopy can be treated approximately as the Radon transform of the field component perpendicular to and along the line defined by the scanning electron beam.

The Radon transform and the Fourier transform are connected by equation (3.17 [Ludwig, 1966]

$$FT_2\{f\}(se) = FT_1\{RT_2[f](\bullet,e)\}(s) \tag{3.17}$$

With equation (3.17), the equations (3.13) and (3.15) can be written using the Radon transform as

$$FT_2\{\boldsymbol{B}(\bullet,y)\}(se(\theta)) = (-i\cdot sign(s)\cdot \boldsymbol{e}(\theta)+\boldsymbol{e}_3)\cdot e^{-2\pi y|s|}\cdot FT_1\{RT_2[\boldsymbol{B}_y(\bullet,0)](\bullet,\boldsymbol{e}(\theta))\}(s) \tag{3.18}$$

$$FT_2\{\boldsymbol{B}(\bullet,y)\}(se(\theta)) = [\boldsymbol{e}(\theta)+i\cdot sign(s)\cdot \boldsymbol{e}_3]\cdot e^{-2\pi y|s|}\cdot FT_1\{\boldsymbol{e}(\theta)RT_2[\boldsymbol{B}(\bullet,0)](\bullet,\boldsymbol{e}(\theta))\}(s) \tag{3.19}$$

In (3.18) and (3.19), the Radon transforms $RT_2[\boldsymbol{B}_y(\bullet,0)](p,\boldsymbol{e}(\theta))$ and $\boldsymbol{e}(\theta)RT_2[\boldsymbol{B}(\bullet,0)](p,\boldsymbol{e}(\theta))$ are the normal and tangential components of the deflection vector, which can be measured using the Lorentz microscopy and are called input functions for determining the magnetic stray field. If one of these input functions is known for all p and $\boldsymbol{e}(\theta)$ (i.e. from the measurements along all angles of rotation), the stray field $\boldsymbol{B}(\boldsymbol{r}, y)$ in the whole half space $y\geq 0$ can be determined using inverse Fourier transform from equations (3.18) or (3.19).

3.3.2 The conventional ART algorithm

We assume that the object of measurement is defined as a density function in the reconstruction space Ω, which is divided into a finite number of non-overlapping elements as shown in Fig. 3.4. The unknown density distribution is approximated as the values assigned to each element by the reconstruction algorithm. This discretisation is ideally as fine as possible and the minimum fineness is related to the assumed spatial resolution in the projection. The projection is also divided into non-overlapping elements corresponding to the positions of the scanning electron probe.

Let P_j, $j=1, 2, ..., m$, be all the projection elements taken together. For every projection element P_j there is a corresponding sub-region δ_j in Ω of which P_j is the projection. Let r be a point in Ω and $f(r)$ be the unknown density function, then

$$\int_{\delta_j} f(r)dr \approx P_j \qquad j=1, 2, ..., m \qquad (3.20)$$

The approximation sign indicates that the process of measurement is not perfect as the result of the finite number of the discrete elements. This is the fundamental equation of ART from which all reconstruction algorithms for the unknown density function $f(r)$ are derived.

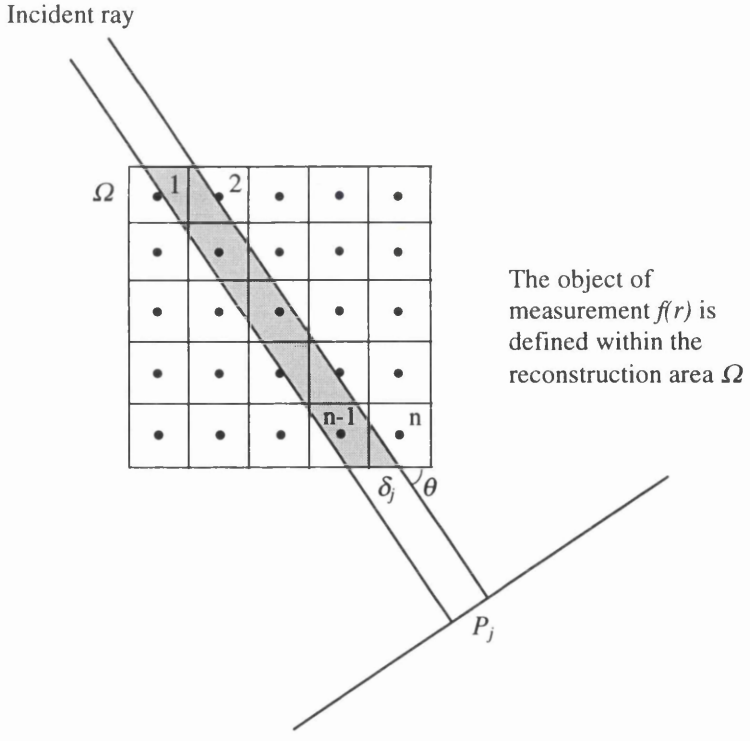

***Fig. 3.4**. Schematic Illustration of the geometry used in conventional ART*

To obtain a digital solution of equation (3.20), we have to represent the continuous space in a discrete fashion. As the first step, we may divide the integral for each projection into sub-regions associated with the reconstruction elements. Let n be

the total number of the elements and Ω_i be the i^{th} element. Equation (3.20) can be written as

$$P_j \approx \sum_{i=1}^{n} \int_{\delta_j \cap \Omega_i} f(r)dr \qquad j=1, 2, ..., m \qquad (3.21)$$

where $\delta_j \cap \Omega_i$ represents an area defined by the overlap region of the element Ω_i and the beam profile δ_j. In each Ω_i we assume that the unknown density function $f(r)$ is a constant. The best estimate of such a constant would be the average value of $f(r)$ over the sub-region Ω_i:

$$f_i = \frac{\int_{\Omega_i} f(r)dr}{\int_{\Omega_i} dr} \qquad i=1, 2, ..., n \qquad (3.22)$$

Under this assumption it is therefore reasonable to use the geometric fraction

$$w_{ij} = \frac{\int_{\delta_j \cap \Omega_i} dr}{\int_{\Omega_i} dr} \qquad \begin{matrix} i = 1,2,...,n \\ j = 1,2,...,m \end{matrix} \qquad (3.23)$$

to estimate the integral of the unknown density function in sub-region Ω_i. Multiplication of equation (3.23) with f_i leads to equation (3.24):

$$w_{ij} f_i \approx \int_{\delta_j \cap \Omega_i} f(r)dr \qquad i=1, 2, ..., n; j=1, 2, ..., m \qquad (3.24)$$

Thus equation (3.20) becomes a set of simultaneous linear equations of the unknown f_i :

$$P_j \approx \sum_{i=1}^{n} w_{ij} f_i \qquad j=1, 2, ..., m \qquad (3.25)$$

Equation (3.25) is highly underdetermined as $m << n$. The discrete solution is attained normally by iteration. Let f_i^q designate the q^{th} estimate of f_i and P_j^q be the q^{th} estimate value of the projection, we may rewrite equation (3.25) as

$$P_j^q \approx \sum_{i=1}^{n} w_{ij} f_i^q \qquad j=1, 2, ..., m \qquad (3.26)$$

The correction of f_i^q is achieved by comparing the difference between the estimated and the measured values of a projection and is weighted to take into account the area fraction value of the electron path in each element, so that

$$f_i^{q+1} = f_i^q + (P_j - P_j^q)\frac{w_{ij}}{N_j} \qquad i=1, 2, ..., n; j=1, 2, ..., m \qquad (3.27)$$

where P_j is the measured projection of j^{th} element, and N_j is the total intersection in Ω of which P_j is the projection, i.e.,

$$N_j = \sum_{i=1}^{n} w_{ij} \qquad j=1, 2, ..., m \qquad (3.28)$$

The choice of the starting values f_i^0 for iteration is arbitrary. They are often chosen to be identically zero or a constant. There is no evidence that the particular choice of starting values will affect the convergence speed of the calculation so long as they are consistent with the nature of the problem.

Gordon *et al.* [1970] showed that the discrete density f_i^q tends to a convergent solution if the discrepancy between the measured and the estimated projections

$$D^q = \sqrt{\frac{1}{m}\sum_{j=1}^{m}\frac{\left(P_j - P_j^q\right)^2}{N_j}} \qquad (3.29)$$

tends to zero or the entropy

$$S^q = \frac{-1}{\ln(n)} \sum_{i=1}^{n} \left(\frac{f_i^q}{\bar{f}} \right) \ln \left(\frac{f_i^q}{\bar{f}} \right) \tag{3.30}$$

tends to a minimum with increasing iteration q.

3.3.3 The magnetic field vector ART algorithm

Whilst a magnetic field is a three-dimensional vector, the interaction between the magnetic field and the moving electrons projects a two-dimensional vector on the detector plane. To utilize the ART algorithm to reconstruct the 3D stray field, one has to work out the vector field equivalence of equation (3.25).

We assume that the extent of the recording head field is within the scanning area of the electron beam in the microscope. In the field-free chamber, the half space in front of the recording head is divided into three parts along the electron beam trajectory, shown in Fig. 3.5. In the first part (I) the stray field $\boldsymbol{B}$=0, the incident electrons travel with a constant speed. As the electrons enter the second region (II) of the space, they are acted on by the Lorentz force and the trajectory of the electrons is modified according to the Lorentz law as

$$\boldsymbol{F}_L = -e \cdot (\boldsymbol{v} \times \boldsymbol{B}) \tag{3.31}$$

where e is electron charge, $\boldsymbol{v}$ and $\boldsymbol{B}$ are vectors of the velocity of electrons and the stray field respectively.

For clarity we employ two Cartesian co-ordinate systems (ξ, η, ζ) and (x, y, z) to define the microscope and the specimen coordinates. These two systems have a common origin at the centre of the polegap and on the ABS of the recording head. The former (ξ, η, ζ) is fixed with ζ along the electron optic axis and η, which is normal to

the ABS is the specimen rod tilt axis. The system (x, y, z) is tied to the head, with z along the head gap and y normal to the ABS and coincident with η; and x lies at an angle θ to the ξ axis according to the rotation position. The plane of electron beam scanning and the plane of reconstruction are in systems (ξ, η, ζ) and (x, y, z) respectively.

Because of the Lorentz force the electrons are deflected. Let s_i be a short distance in region II and $\boldsymbol{B}_i$ be the average value of $\boldsymbol{B}$ in s_i along the electron beam trajectory. The components of the electron beam deflection vector, which are parallel to the ξ-η plane as the electrons traverse the distance s_i, are calculated as

$$dD_{\xi i} = \left(\frac{e}{2mE}\right)^{1/2} \cdot \frac{s_i^2}{2} \cdot B_{yi} \tag{3.32}$$

$$dD_{\eta i} = -\left(\frac{e}{2mE}\right)^{1/2} \cdot \frac{s_i^2}{2} \cdot B_{xi} \tag{3.33}$$

The region III is again field free and the electrons travel in a straight line to the detector plane at a distance L from the centre of the head. We suppose that the field region (II) is divided to equal elements, $s_i \equiv s$, and the total number of rays of electron beam scanning is m. Thus the total deflection of the electron beam on the detector plane are given by

$$D_{\xi j} = \left(\frac{e}{2mE}\right)^{1/2} \left(\frac{s^2}{2} + sL\right) \sum_{i \in ray(j)} B_{yi} \qquad j=1, 2, ..., m \tag{3.34}$$

$$D_{\eta j} = -\left(\frac{e}{2mE}\right)^{1/2} \left(\frac{s^2}{2} + sL\right) \sum_{i \in ray(j)} B_{xi} \qquad j=1, 2, ..., m \tag{3.35}$$

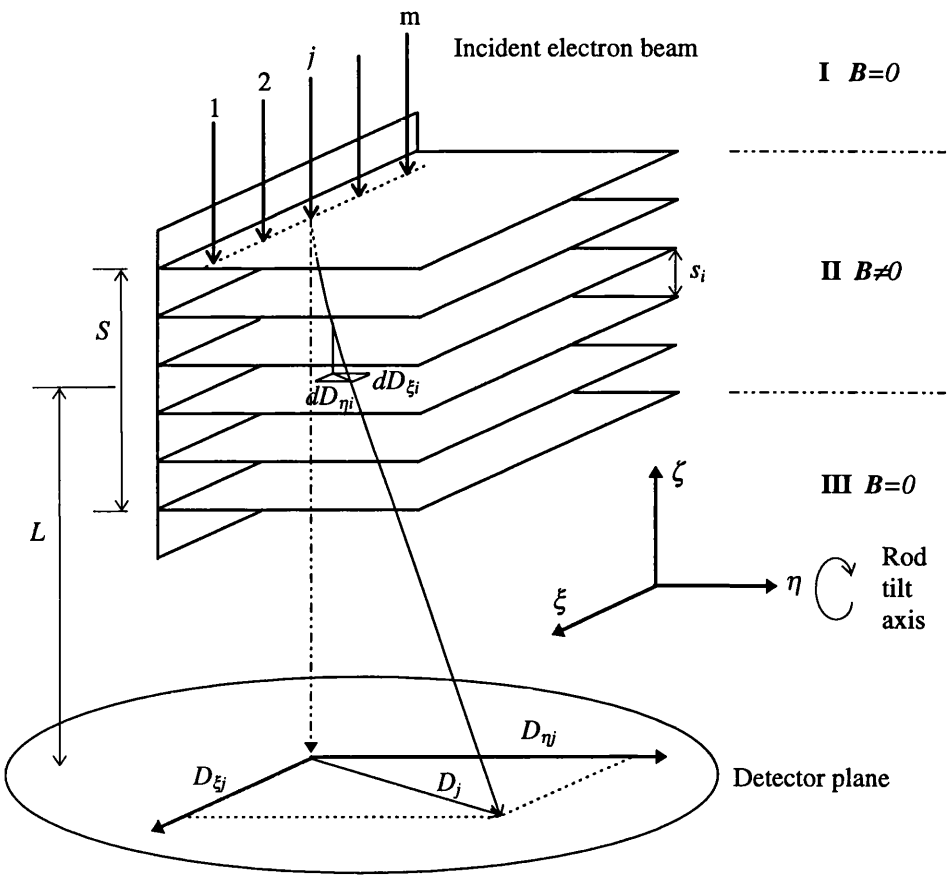

(a)

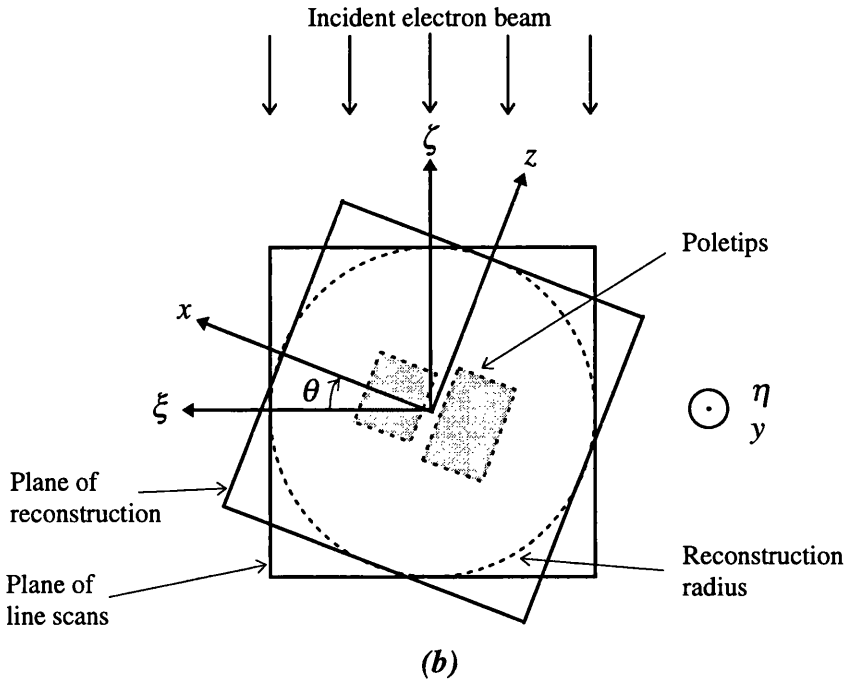

(b)

Fig. 3.5. *Model of the representation for the magnetic stray field in ART*

the sums are taken over all the elements through which the beam has passed. D_ξ is determined solely by component B_y of the stray field, while D_η is a function of B_x and B_z as we rotate the head through different angular positions θ with respect to the direction of incidence of the electron beam as shown in Fig. 3.5(b). Therefore, the general form of equation (3.35) is

$$D_{\eta j} = -\left(\frac{e}{2mE}\right)^{1/2}\left(\frac{s^2}{2}+sL\right)\left(\cos\theta_{m_\theta}\sum_{i\in ray(j)}B_{xi}+\sin\theta_{m_\theta}\sum_{i\in ray(j)}B_{zi}\right) \qquad (3.36)$$

$$j=1, 2, ..., m$$

in which the subscript m_θ denotes the m_θ^{th} rotation angle. Equation (3.34) and (3.36) are the magnetic field vector versions of equation (3.25). Therefore, a similar iterative procedure may be applied. Let

$$A=\left(\frac{e}{2mE}\right)^{1/2}\left(\frac{s^2}{2}+sL\right) \qquad (3.37)$$

The iterative form of equations (3.33) and (3.36) can then be written as

$$D_{\xi j}^{q} = A\sum_{i\in ray(j)}B_{yi}^{q} \qquad j=1, 2, ..., m \quad (3.38)$$

$$D_{\eta j}^{q} = -A\left(\cos\theta_{m_\theta}\sum_{i\in ray(j)}B_{xi}^{q}+\sin\theta_{m_\theta}\sum_{i\in ray(j)}B_{zi}^{q}\right) \quad j=1, 2, ..., m \quad (3.39)$$

As the electron beam deflection is proportional to the length of the electron path in the field region, it is reasonable to use the actual length of the electron trajectory in each elemental area as the weighting factor to assign the iterative corrections among the elements. Thus the iterative values of the components of the stray field are given by

$$B_{xi}^{q+1} = B_{xi}^{q} + \left(D_{\eta j} - D_{\eta j}^{q}\right) \cdot \cos\theta_{m_\theta} s_i / N_j \qquad j=1, 2, ..., m \quad (3.40)$$

$$B_{yi}^{q+1} = B_{yi}^{q} + \left(D_{\xi j} - D_{\xi j}^{q}\right) s_i / N_j \qquad j=1, 2, ..., m \quad (3.41)$$

$$B_{zi}^{q+1} = B_{zi}^{q} + \left(D_{\eta j} - D_{\eta j}^{q}\right) \cdot \sin\theta_{m_\theta} \cdot s_i / N_j \qquad j=1, 2, ..., m \quad (3.42)$$

in which

$$N_j = \sum_{i \in ray(j)} s_i \qquad j=1, 2, ..., m \quad (3.43)$$

In equations (3.40) ~ (3.42), the input functions, like that in the RTM, are electron beam deflection vectors measured from all electron beam viewing angles. Therefore the input data sets for tomographic calculation of the recording head fields are identical for both RTM and ART. This allows us to carry out a comparison study of the two methods for both model and real thin film head fields in chapter 4 and 5. The experimental acquisition of these input functions will be introduced in the following section.

3.4 Experimental implementation of electron beam tomography for recording head fields

To reconstruct a 3D recording head field from its projections using the techniques discussed in section 3.3, a complete set of digital data of the electron beam deflection vector at a series of angle positions has to be obtained. These data are extracted from the DPC image pairs of the stray field acquired in a STEM. The input data sets are subjected to appropriate processing to correct for any deficiencies, e.g. misalignment caused by the imperfect experimental arrangements.

3.4.1 The DPC image collection in the JEOL 2000FX (S)TEM

The fundamental principles of DPC Lorentz microscopy to measure the two-dimensional projections of the integrated stray field have been discussed in section 2.4. By utilising the specimen stage of the JEOL 2000FX we can rotate the recording head around the rod axis over ±45°. Whilst this angle may be enough for the ART method, it is certainly not sufficient for the RTM technique, the latter requiring views over ±90° to obtain a complete set of electron beam deflections as described in the previous sections. Since we hope to be able to compare the field reconstruction results obtained from both ART and RTM, we have designed a mounting stub for the recording head to extend the specimen tilt angle over the required ±90°, and this will be described later in chapter 5.

The geometry to obtain the electron beam deflection vectors, as the electron probe traverses the magnetic stray field at different rotations of the recording head using DPC Lorentz microscopy, is shown schematically in Fig. 3.6. The same Cartesian coordinate systems used in Fig. 3.5 are adopted. The electron beam scans parallel to the ξ-ζ plane at a fixed distance $\eta=y=y_0$ from the ABS; this forms a plane on which the stray field from the recording head is reconstructed. The orientation of the recording head is again defined in system (x, y, z), with z along the head gap and y normal to the ABS coincident with η, whilst x lies at an angle θ to the ξ axis corresponding to the rotation of the head.

The two components of the electron beam deflection vector are acquired by signal subtraction from opposite segments of the quadrant DPC detector. The detector orientation relative to the specimen axis and the excitation of the image forming lenses have been set properly so that the signal pairs (A-C) and (B-D) present the variations of the electron beam deflections which are perpendicular and parallel to the ABS respectively.

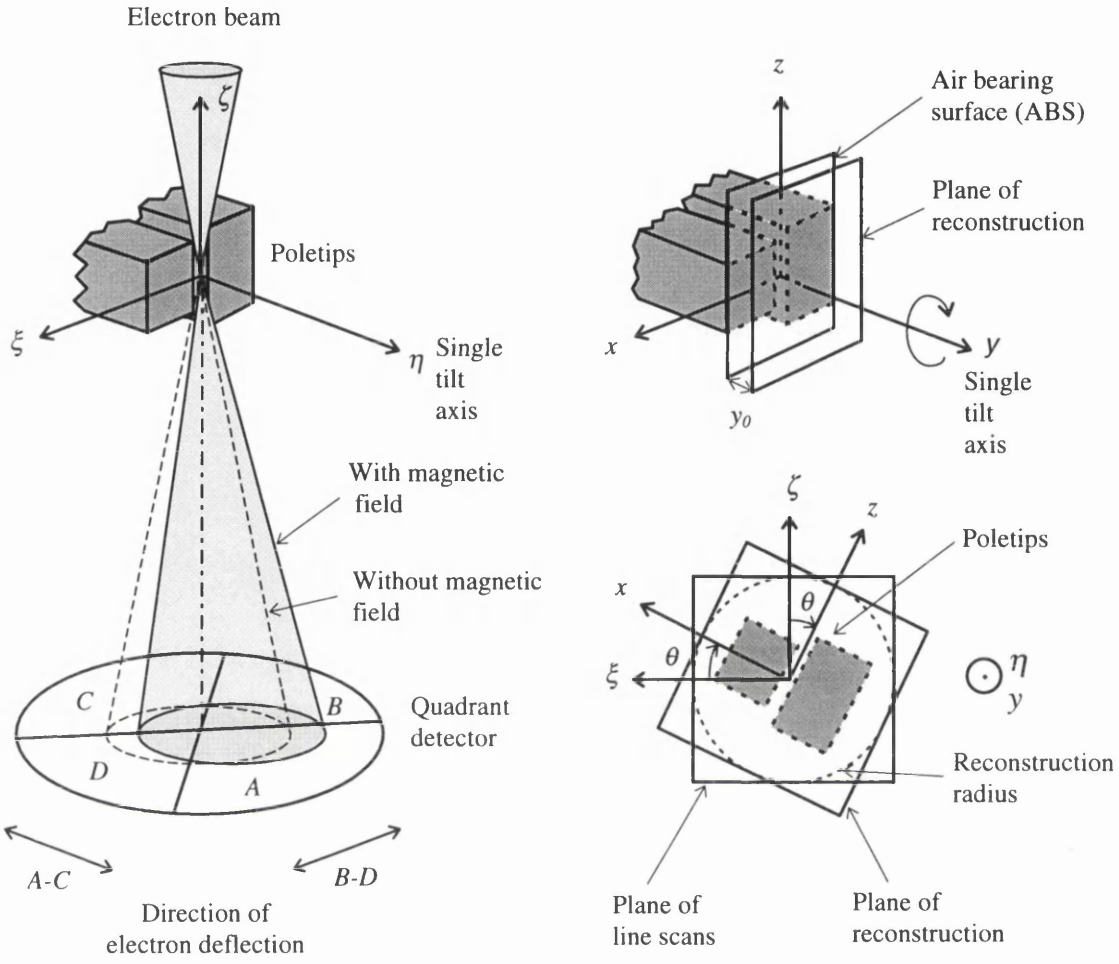

***Fig. 3.6**. Simplified schematic of the DPC Lorentz microscopy applied in tomographic studies for magnetic recording head fields*

Fig. 3.7 shows the hardware for acquiring the DPC image pairs. A Link AN10000 computer is used to control the scanning of the electron beam in the JEOL 2000FX. The current signals taken from all four segments of the DPC detector are fed into the matched pre-amplifiers and are converted to voltages. A main amplifier and mixer unit is used to process the voltage signals. All voltage signals used to form the DPC images in a complete data set are subject to the same gain to keep them internally-consistent. Amplification is chosen to make full use of the dynamic region of the image contrast. Signal monitoring and combination are also performed at this stage. The oscilloscopes are employed to monitor the DPC image pairs of (*A-C*) and (*B-D*), which

are then acquired and saved into the buffer of the Link AN10000. The acquisition process is repeated after the recording head is rotated about the single tilt axis by angular interval of a few degrees $\Delta\theta$ until the full angular region of $(180°\text{-}\Delta\theta)$ is covered.

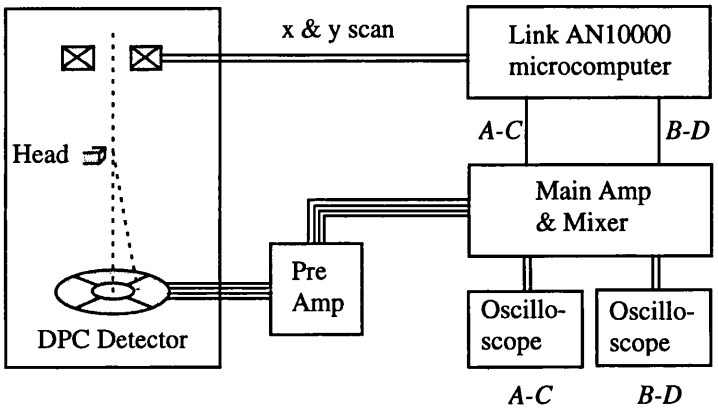

Fig. 3.7. *The hardware for acquiring the DPC image pairs*

Examples of the DPC image pairs of the magnetic stray field with the head driven by a DC current are shown in Fig. 3.8. Only for visualisation is the contrast of each image enhanced. These images are saved in a study and ready for further data processing.

3.4.2 Extraction of the input data sets from the DPC image pairs

The input data for tomographic calculation of the recording head field is a tilt series of electron beam deflection vectors as the beam scans in a plane in front of the head. The DPC image pairs shown in Fig. 3.8 are two components of the deflection vectors in a raster, from which line scans will be extracted at the same distance from the ABS. These line scans of different rotation angles define the plane in which the stray field from the

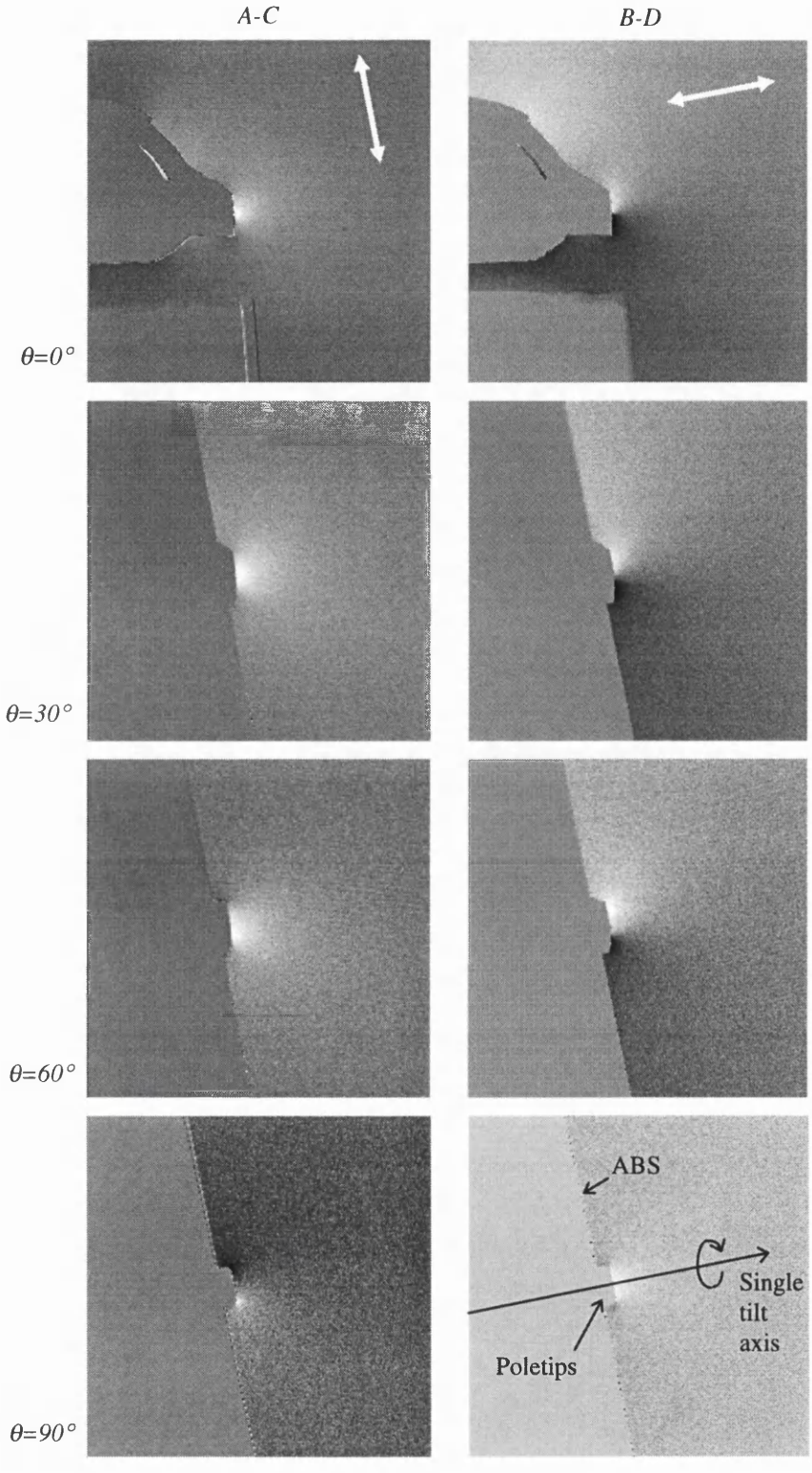

***Fig. 3.8**. Pairs of the DPC images of the integrated stray field from a thin film head taken at different angular positions, the single tilt axis is shown in the right-bottom image and the mapping direction of the stray field are indicated by the arrows*

recording head is reconstructed. There is no scan rotation relative to the specimen available in the JEOL 2000FX. Having fixed the directions of the deflection normal and parallel to the ABS the image is such that the ABS lies at an angle ~80° to the image raster lines [see Fig. 3.8]. Thus the image has to be rotated accordingly, using the image processing package IMPDEV, to simplify extraction of the required line scans. The flying height of commercial heads continue to decrease and hence we wish to take the line scans as close to the ABS as possible. The smallest distance depends mainly on two factors: the resolution we have set for acquiring the digital DPC images and a decent magnification matching the extent of the stray field. The surface roughness caused by any dust on the ABS during sample preparation is also a problem and can limit how close we can go to the ABS. One can easily make the quantum of the line scan movement smaller by using higher image magnification and suitable resolution. Nevertheless, the magnification is restricted by the fact that ideally the image must cover the extent of the stray field as this is strictly the requirement for the reconstruction algorithms and the image resolution has to be set to make the amount of data processing reasonable.

As an example, Fig. 3.9 shows the line scans extracted from the DPC image pairs of Fig. 3.8 at ~0.25 μm from the ABS. It can be seen from these line scans that the integrated stray field, especially the component of (*B-D*), do not go to zero and its effect to the reconstruction will be discussed later in chapter 4.

3.4.3 Alignment of the line scans

The lack of an immediately available common system of coordinates results from the microscope goniometer not been truly eucentric at high resolution and from imperfect mounting of the specimen head. Thus, the goniometer system is unable to provide sufficient control as the specimen is tilted in the microscope, and the precise relationship between the microscope coordinate system and the specimen coordinate system, as shown in Fig. 3.6, is lost. The Duisburg group has designed a precision stage for the SEM to permit automated data recording [Steck *et. al.*, 1990]. In the severely

restricted space in the vicinity of the specimen in JEOL 2000FX (S)TEM, it proved impossible to construct a specimen rod to achieve the required accuracy of alignment. In fact perfect precision matching is impossible and in any case the mounting of the head is subject to position error. Therefore an alignment of the line scans is a routine procedure in tomography studies.

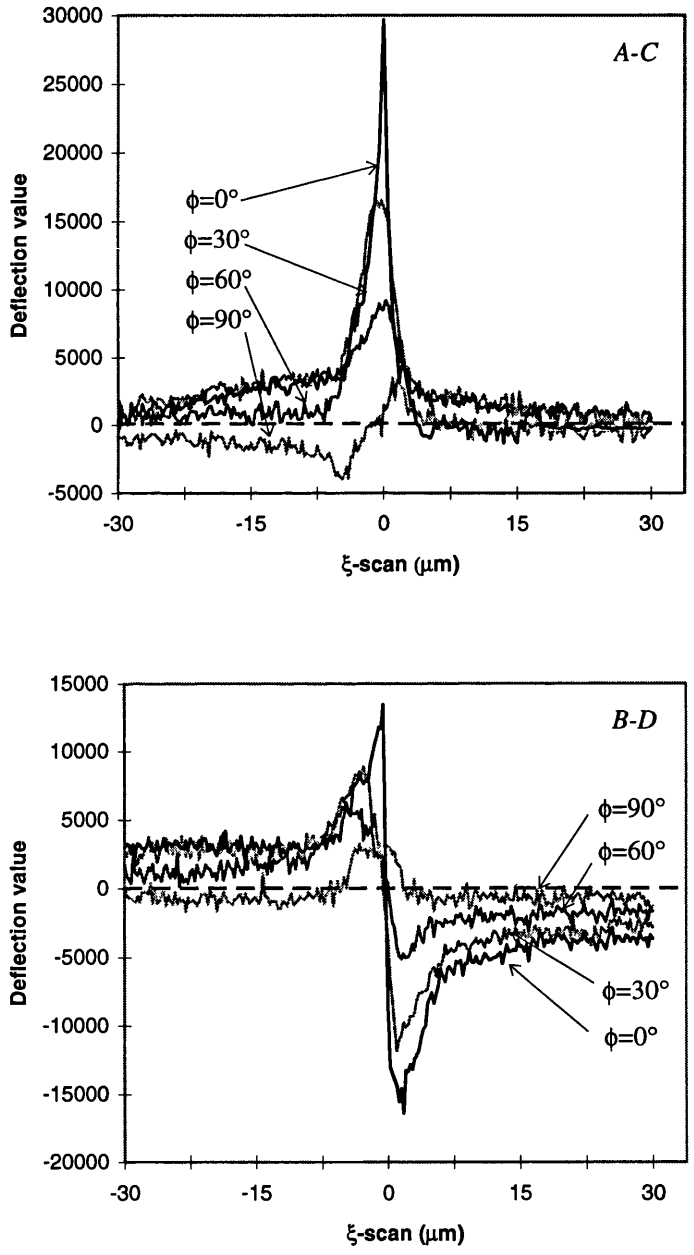

Fig. 3.9. *Line scans taken from the DPC image pairs in Fig. 3.8 at 0.25μm from and parallel to the ABS*

Methods used to determine a common coordinate system fall into two categories, those based on correlation functions and those based on fiducial markers. The cross-correlation alignment [Frank, 1980; Guckenberger, 1982] relies on a common motif which exists in two projections, a cross-correlation function (CCF) is used to search the motif and compute the shift vector. To bring the two motifs in to registration, the second projection is shifted by a vector of equal magnitude, but in opposite direction to that of the shift vector. The fiducial marker method [Lawrence, 1983; Luther *et al.*, 1988] aligns the projections of different views by triangulation from positions of gold markers which have been placed on the surrounding support film of the object of measurement. The relationship between the specimen and digital raster coordinate systems is then determined from a least-squares analysis of the positions of the fiducial markers measured from the projections. The projections are transformed to a common coordinate system and the pixels are resampled by interpolation.

As the property of the magnetic stray field changes with rotation, there is no reliable motif of the field exists. Therefore the CCF peaks will become too broad and noisy to be used effectively to compute the possible axis shift between two projections of the integrated stray field. The fiducial marker method is a possible tool for alignment of the recording heads, but could require the development of an experimental technique to add micro-sized markers near the centre of the polegap on the ABS.

In all the experiments described in this thesis we use the intrinsic feature of the field structure to align the translational displacement. Since the projections of the stray field from a recording head change smoothly as the head rotates, the profiles of the line scans must vary in a continuous manner. This has been confirmed from DPC images of the model thin film head fields as will be discussed in chapter 4. The alignment is done interactively by superimposing all the line scans of different views in one graph using image processing packages such as AXUM 4.0 or Microsoft Excel. The misalignment is gradually eliminated by digital interpolation on this graph. The two sets of line scans for the two orthogonal components are subject to the same interpolation. This method can achieve subpixel level accuracy of alignment. The aligned input data sets can then be used to reconstruct the 3D recording head field and this will be discussed in detail in chapter 5.

3.5 Conclusion

In the two reconstruction algorithms, the RTM is based on the Fourier transformation and hence requires ±90° rotation of the reconstructed stray field. In RTM the Radon transform of the stray field is approximated as a straight line in the measuring plane. Therefore, the RTM is a linear technique and will be subject to error if the stray field is strong. Besides, the algorithm of RTM is derived from a magnetic source free half space and any reconstruction must satisfy this condition.

The ART is purely an algebraic method, in principle it can be applied to any continuous or non-continuous spatial distribution. There is no limitation for particular magnetic source distribution, so long as the reconstruction region is big enough to contain the extent of the stray field. The nature of the algorithm also suggests that the ART can provide reasonable details of the object of measurement with fewer projections (<±90°).

References

Andrew, H. C. (1970), *Computer Techniques in Image Processing,* Academic Press, New York.

Bracewell, R. N. and A. C. Riddle (1967), *Astrophys. J.* **150**, 427-434.

Crowther, R. A. *et al.* (1970), *Nature (London)* **226**, 421-425.

DeRosier, D. and A. Klug (1968), *Nature (London)* **217**, 130-134.

Elsbrock, J. B. *et al.* (1985), *IEEE Trans. Magn.*, **21**, 5,1593-1595.

Ferrier, R. P., Y. Liu, J. L. Martin and T. C. Arnoldussen (1995), *J. Mag. Magn. Mater.*, **149**, 387-397.

Ferrier, R. P (1992), *Report on SUR Contract SL91459.*

Frank, J. (1980), *Computer Processing of Electron Microscopy Images* (P. W. Hawkes, ed.), Springer-Verlag, Berlin, 187-122.

Gordon, R. *et al.*(1970), *J. theor. Biol.* **29**, 471-481.

Guckenberger, M. (1982), *Ultramicroscopy* **9**, 167-174.

Jiles, D (1991), *Introduction to Magnetism and Magnetic Materials*, Chapman & Hall.

Lawrence, M. C. (1983), *Proc. Electron Microsc. Soc. S. Afr.* **13**, 19-20.

Ludwig, D. (1966), *Communications on pure and applied mathematics*, Vol.**XIX**,49-81.

Luther, P. K. et al. (1988), *Ultramicroscopy* **24**, 7-18.

Matsuda, J. *et al* (1990), *IEEE Trans. Magn.*, **26**, 5, 2061-2063.

Radon, J. (1917), *Math. phys. Klasse* **69**, 262-277.

Steck, M. (1990), *Ph.D. thesis,* University of Duisburg.

Steck, M. *et al.* (1990), *IEEE Trans. Magn.*, **26**, 5, 1343-1345.

Chapter 4

Computer simulation of 3D reconstruction of recording head fields

4.1 Introduction

The 3D reconstruction methods for recording head fields have been described in chapter 3. The purpose of this chapter is to investigate the performance of these reconstruction algorithms by means of computer simulation. It is practically impossible to have a direct experimental evaluation of the result of the electron beam tomography of recording head fields. However, if a model field distribution is known a set of electron beam deflection data (back projections) can then be computed, as the Lorentz interaction between the magnetic field and the moving electrons in free space in the microscope can be precisely calculated. Using such a simulated data set, computer modelling can be carried out to survey the 3D reconstruction algorithms for recording head fields.

In this chapter, model thin film head fields are adopted as the simulated field distributions and used to calculate the electron beam deflection data sets (section 4.2). 3D reconstruction of the model stray fields are performed with different reconstruction parameters. Using different iterations and field gradients, the convergence of our ART tomography program is investigated (section 4.3.1), and the reconstructed results are compared to those obtained by RTM (section 4.3.2). The reconstruction using the ART for different rotation angles is discussed in section 4.3.3. The effects of different numbers of angular position m_θ and the scanning points per angular position m are presented in section 4.3.4. The reconstruction using truncated input data sets is also studied (section 4.3.5). Finally the conclusions are given in section 4.4. These simulations provide not only the justifications for the performance of the 3D

reconstruction methods but also the knowledge to choose suitable measurement parameters for real recording head fields.

4.2 Numerical computation of the electron beam deflection data sets

As thin film recording heads for disk drives are the major category of our experimental specimens, a simulated thin film head field is an ideal field distribution for the evaluation of the reconstruction algorithms. Nevertheless, the calculation of the magnetic field distribution has always been a challenge. In general cases, numerical techniques have to be used to obtain a solution of the magnetic field over a volume. In most situations the problem amounts to solving either Laplace's or Poisson's equation over a finite region of space, which may be three dimensional or two dimensional, with an appropriate set of boundary conditions.

If the problem is set up in a spatial domain in which there are no field sources, the Laplace's equation of form (3.11) applies. In cases where field sources exist within the space of interest then the source distributions have to be known and included into the equation. The problem thus becomes finding a solution of Poisson's equation with the appropriate boundary conditions

$$\nabla^2 \boldsymbol{A} = -\mu_0 \boldsymbol{J} \qquad (4.1)$$

where the presence of the field sources are taken into account in the form of the current density $\boldsymbol{J}$.

Three general numerical methods, finite-difference, finite-element and boundary-element techniques, have been successfully used to solve the equation for the magnetic field [Chari and Silvester, 1980] [Trowbridge, 1988]. The finite-difference method (FDM) of magnetic field calculation was the principle numerical tool from the early days of digital computing in the 1940's until about 1970. The use of a regularly placed orthogonal or polar grid made it difficult for FDM to deal with complicated geometries and large field gradients. As a result, FDM has largely been superseded by

the finite-element method (FEM) since about 1970. In a finite-element calculation, the spatial domain is divided into triangle-shaped elements and the size of the elements can be varied over the regions of interest so that more elements can be generated in regions where the field gradient is large. Therefore FEM is more effective in obtaining sufficient accuracy for the calculation of magnetic fields. Boundary-element techniques (BEM) for magnetic field calculation are the most recent development [Brebbia and Walker, 1980] [Hoole, 1989]. The coupling of boundary-element and finite-element methods can greatly ease the computation of the magnetic field with complicated boundary conditions and an application of this method to a symmetric multi-body magnetic source problem has been reported [Liu and Yi, 1986].

There are a number of software packages based on FEM available. The model thin film head fields used in this reconstruction simulation were computed using a finite-element package called TOSCA by Dr. Heim at IBM Storage System Division. The stray fields were calculated on a series of square planes in front of the poletips at different distances and parallel to the polefaces of the model thin film head. These planes are equivalent to the measurement plane in Fig. 3.3 and the plane of reconstruction in Fig. 3.5.

The trajectory of electrons as they traverse through the stray field region has been discussed in section 3.3.3. With the help of equations (3.34) and (3.36), the electron beam deflection vectors for different scanning points and angular positions can be calculated. We use 200 kV to accelerate the electrons so that the electron beam deflection is very small compared to the electron path. For example, the peak value of these sets of simulated stray fields is ~1.5 T, which represents the writing component $\boldsymbol{B_x}$ at 0.1 μm from the centre of the polegap. If the length of the discrete element is set typically to be 0.25 μm, the maximum electron beam deflection for the peak value as the electrons traverse the elemental area is about 1.1×10^{-3} μm. Therefore a linear approximation that the deflection vector is integrated with the field component perpendicular to the electron beam in the same measured plane rather than along the real trajectory is acceptable. In fact, the electron beam trajectory in a STEM is not as simple as that shown in Fig. 3.5, there are electromagnetic lenses between the specimen stage and the detector. But the effect of all the imaging lenses can be regarded as a single

factor namely the effective camera length L. The determination of L will be discussed in chapter 7.

As an example, the model thin film head field at a distance of 0.5 μm from the ABS is shown in Fig. 4.1 in 3-D surface plot format. The display covers an area of 24.5 × 24.5 μm. The number of the grid nodes are 99 × 99 and therefore the side length of the elemental area is 0.25 μm. The model thin film head has poletip dimensions of 8.0 × 2.5 and 5.0 × 2.5 μm separated by a 0.5 μm gap (c.f. Fig. 3.5). As shown in Fig. 4.1, all three components of the stray field tend to zero at the boundaries of the display area. Therefore the stray field from the model thin film head lies within the square at this plane and the use of this plane as the measured plane or reconstructed plane will not result in information loss of the reconstructed stray field.

We assume that the electron beam scans along the ξ-axis at 0.5 μm from the ABS, whilst the head is rotated from -90° to +90° (as demonstrated in Fig. 3.6). The electrons will encounter the stray field shown in Fig. 4.1 from different angular positions and be deflected from its zero-field trajectories. Using equations (3.34) and (3.36), the tangential (ξ-axis) and the normal (η-axis) components of the electron beam deflection vectors in the detector plane can be calculated and are displayed in Fig. 4.2. In this simulation, the number of the scanning points per angular position is chosen to be the same as the number of the grid nodes in a row in Fig. 4.1. The data shown in Fig. 4.2 is a complete set of input data for tomographic computation.

If we overlap the line traces of Fig. 4.2 angle-by-angle in a plane, we can observe more accurately the variation trend of the electron beam deflection vector through different rotations. Fig. 4.3 are sets of such line traces taken from Fig. 4.2 and the curves are the line traces from 0° (the highest curve) to 80° with an interval of 10°. As we can see from Fig. 4.3. the profiles of both components of the deflection vector change smoothly with the head rotated about a single tilt axis, which is in the centre of the polegap and normal to the ABS. This is the field feature which helps us to understand how to align the translational displacement of the electron beam deflection data sets in practical 3D reconstruction of recording head fields as has been mentioned in section 3.4.3.

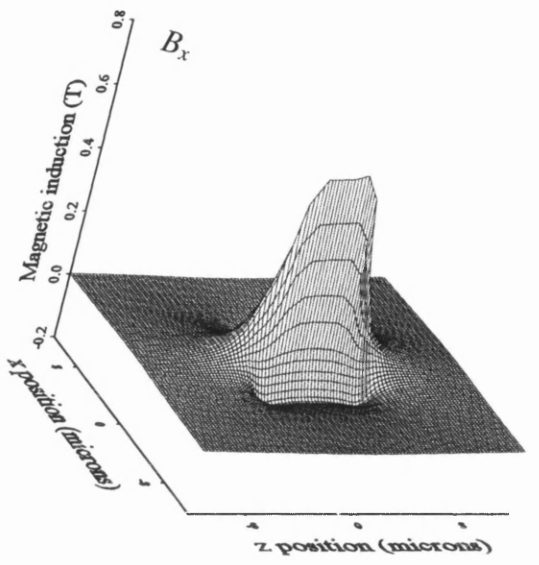

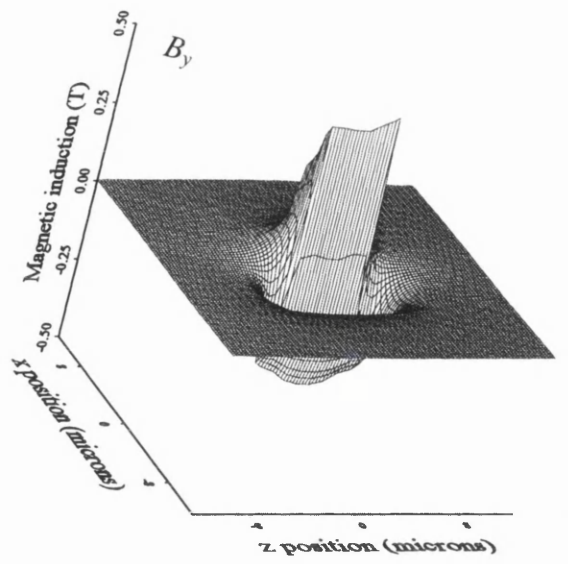

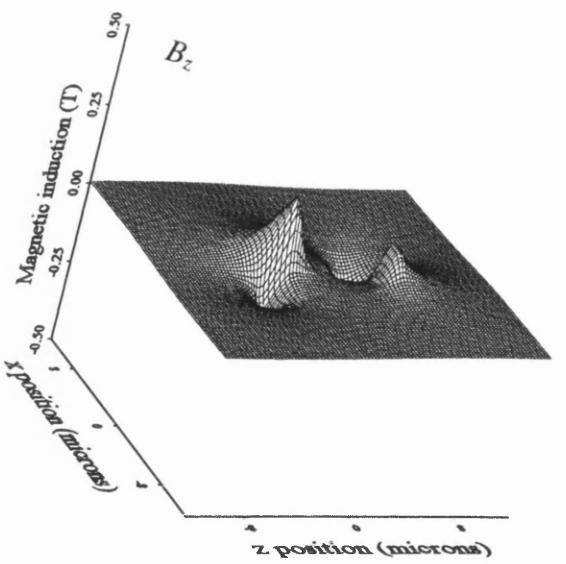

Fig. 4.1. The model thin film head field at a distance of 0.5 μm from the ABS.

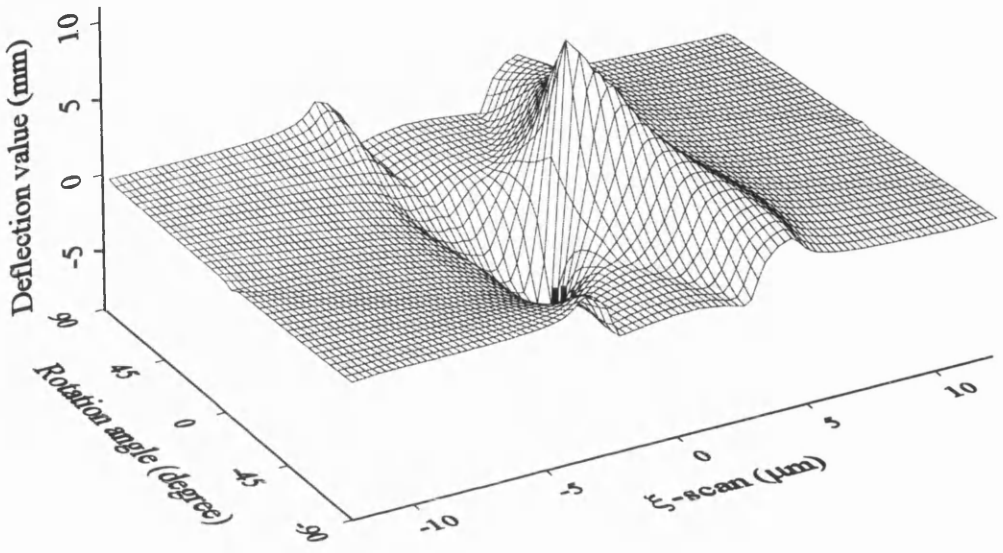

(a)

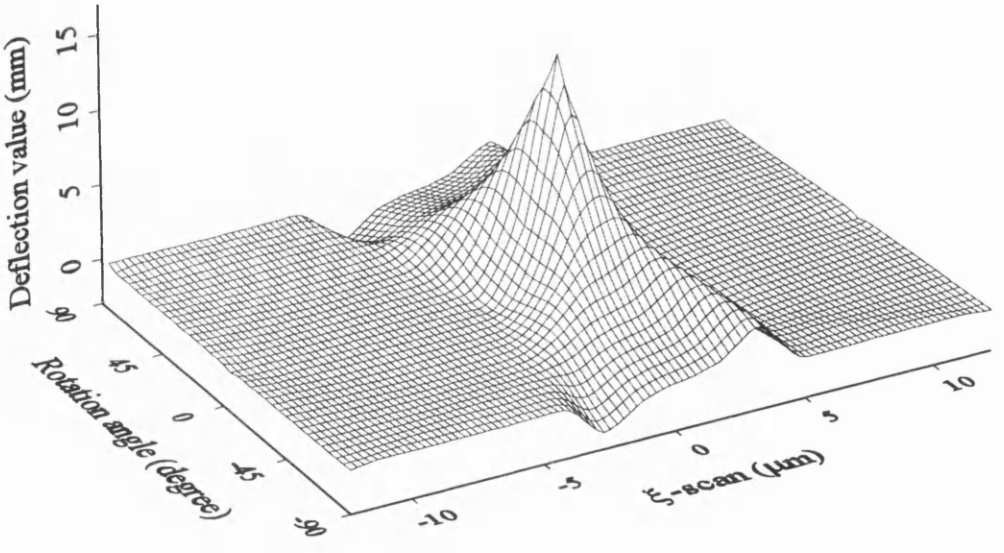

(b)

***Fig. 4.2**. Computed electron beam deflection data sets for the model thin film head field at a distance of 0.5 μm from the ABS; (a) deflections in the ABS plane, (b) deflections normal to the ABS plane.*

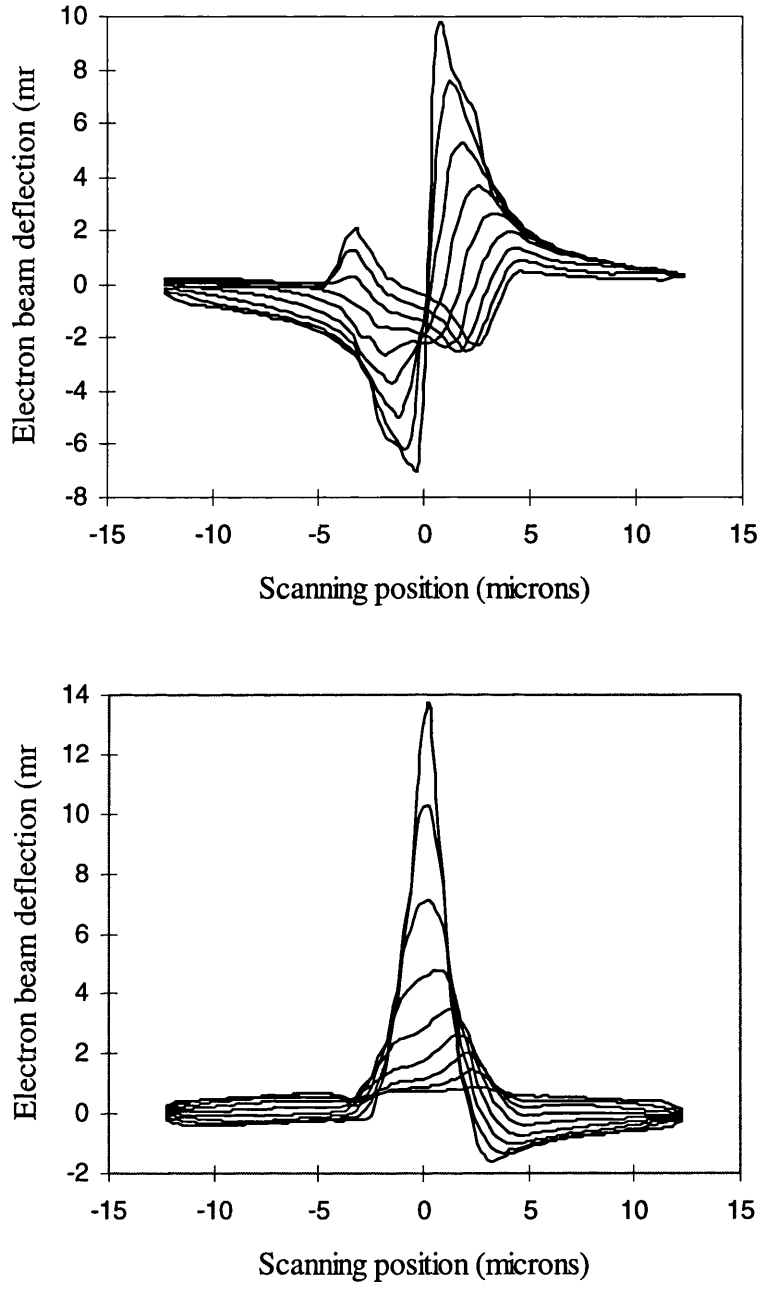

Fig. 4.3. *Line traces of electron beam deflection data extracted from Fig. 4.2; the curves are line traces from 0° (the highest curves) to 80° with an interval of 10°.*

The amplitude of the electron beam deflection vector is a function of the acceleration voltage of electrons ($E^{-1/2}$), the camera length (L) and the integrated stray field (B). The relationship among them is presented in Fig. 4.4. The linear

approximation is based on small deflection in field region. Therefore higher acceleration voltage is desirable. For all the simulations in this chapter and the practical reconstruction described in this thesis, 200 kV acceleration voltage is used.

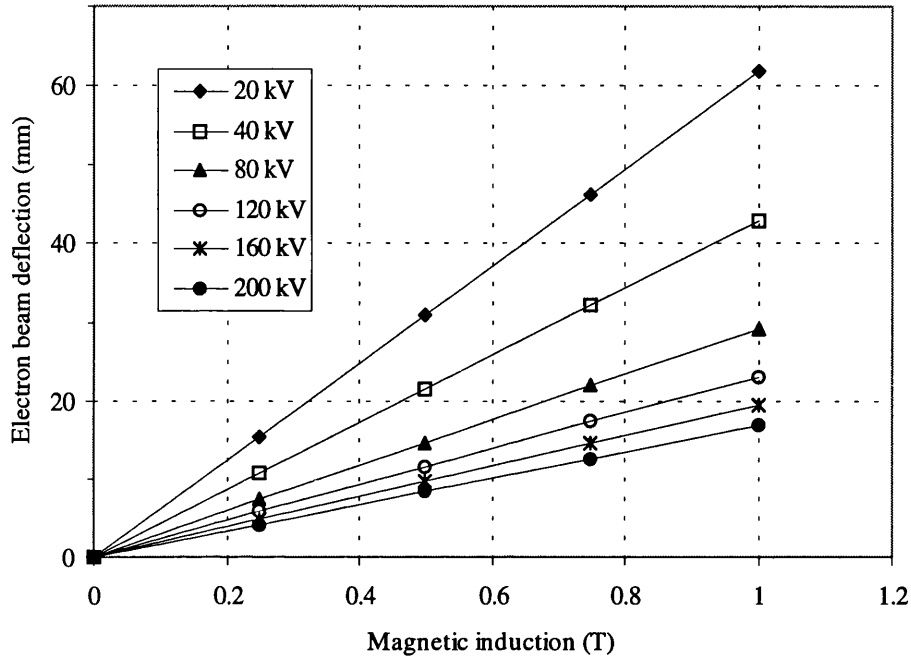

Fig. 4.4. *Electron beam deflection as a function of the magnetic induction and the acceleration voltage of electrons; the camera length L is 6 m.*

4.3 3D reconstruction simulation using ART and RTM

4.3.1 Convergence of the ART

The ART reconstruction algorithm is an iterative technique. Therefore the reliability and convergence are matters of utmost concern. I have written our own version of ART tomography program using the FORTRAN language, as it is particularly effective for scientific calculation. To test the reliability and convergence of our ART code, different

iterative starting points have been used to reconstruct model thin film head fields of different magnitudes and all of these reconstructions converge to steady solutions. Two kinds of error functions are employed as the measures of convergence of the reconstructed field B_{xyz}^{q} as

$$E_a = \frac{\sum_{i=1}^{n}\sum_{j=1}^{n}\left|B_{th}(i,j) - B_{rec}(i,j)\right|}{\sum_{i=1}^{n}\sum_{j=1}^{n}\left|B_{th}(i,j)\right|} \tag{4.1}$$

$$E_v = \sqrt{\frac{\left[\sum_{i=1}^{n}\sum_{j=1}^{n}\left|B_{th}(i,j) - B_{rec}(i,j)\right|\right]^2}{\left[\sum_{i=1}^{n}\sum_{j=1}^{n}\left|B_{th}(i,j) - \overline{B}_{th}\right|\right]^2}} \tag{4.2}$$

where B_{th}, B_{rec} and $\overline{B}_{th}$ are the theoretical, reconstructed and averaged theoretical magnetic induction respectively; n denotes the number of reconstruction grids. The relative reconstruction errors of E_a and E_v for different iterations using the data sets shown in Fig. 4.2 are presented in Fig. 4.5. It can been seen that both measures of reconstruction error decrease steadily and tend to a minimum at ~20 iterations. The minimum reconstruction errors are determined by the reconstruction parameters used as will be discussed in the following sections, and they are also a function of the magnitude or the gradient of the reconstructed stray field. Simulation reconstruction have been performed for the model thin film head fields at 1.0, 0.5 and 0.25 μm from the ABS and the corresponding peak values of the writing field B_{xmax} are 0.25, 0.58 and 1.07 T respectively, and the reconstruction errors after 20 iterations are shown in Fig. 4.6. As the distance from the ABS increases both the field, the field gradient decrease and it is the latter which has the biggest effect on the reconstruction accuracy. The parameters used for the reconstruction simulations shown in Fig. 4.5 and Fig. 4.6 are listed in Table 4.1.

Table 4.1

Acceleration voltage	200kV
Camera length	6m
Number of scanning points m	99
Number of angular positions m_θ	36
Rotation angle	175°

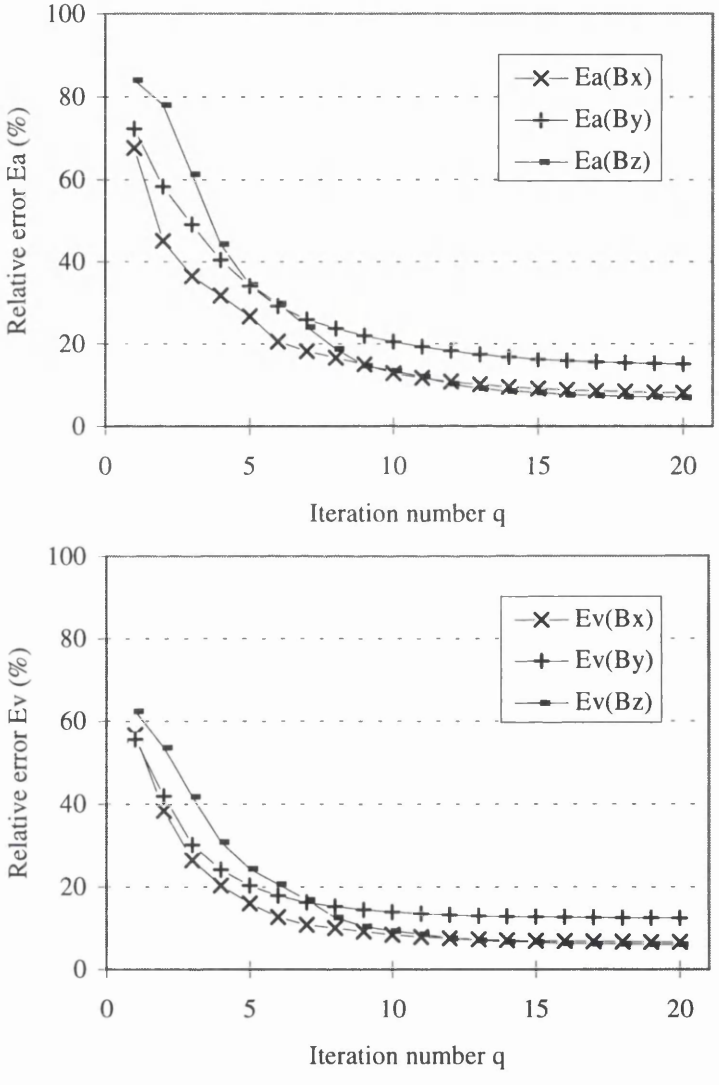

Fig. 4.5. *Reconstruction errors using the ART for different iterations.*

The parameters in Table 4.1 are typical values used for the practical reconstruction described in this thesis.

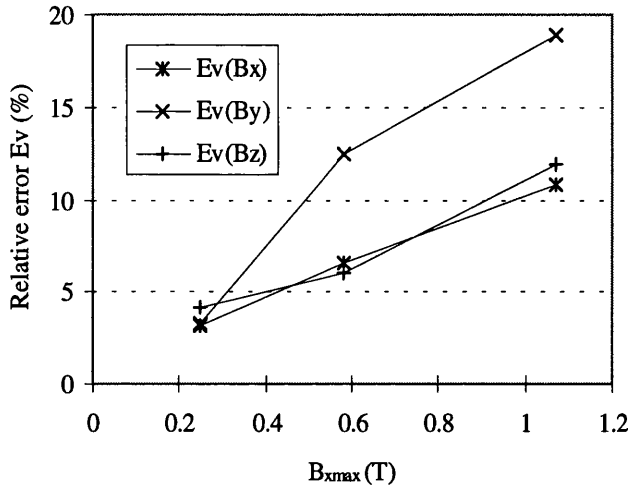

Fig. 4.6. Reconstruction error of the ART as a function of the magnitude of the reconstructed writing field, both the field and the field gradient increase with the decrease of the distance from the ABS.

The components of the stray field after 20 iterations together with the absolute errors, which are the subtraction between the reconstructed and the original (Fig. 4.1) components, are shown in Fig. 4.7. The reconstructed field is in very good agreement with the original. The major errors come from where the fields have greatest gradients, e.g. ΔB_y in the centre of the polegap. The ripples in the background are due to the finite number of viewing angles as will be discussed in section 4.3.4.

4.3.2 Comparison of the reconstruction using ART and RTM

As has been described in chapter 3, with RTM both components of the electron beam deflection vector allow independent determination of the 3D stray field. Fig. 4.8 shows the field components reconstructed by the RTM tomography program provided by our colleagues in Duisburg University, using the tangential (Fig. 4.2.(a)) and normal (Fig. 4.2.(b)) components of the electron beam deflection data. Although both sets of reconstructed fields look close to the original shown in Fig. 4.1, there are differences in magnitude and in some details of the reconstructed structures between them. The same

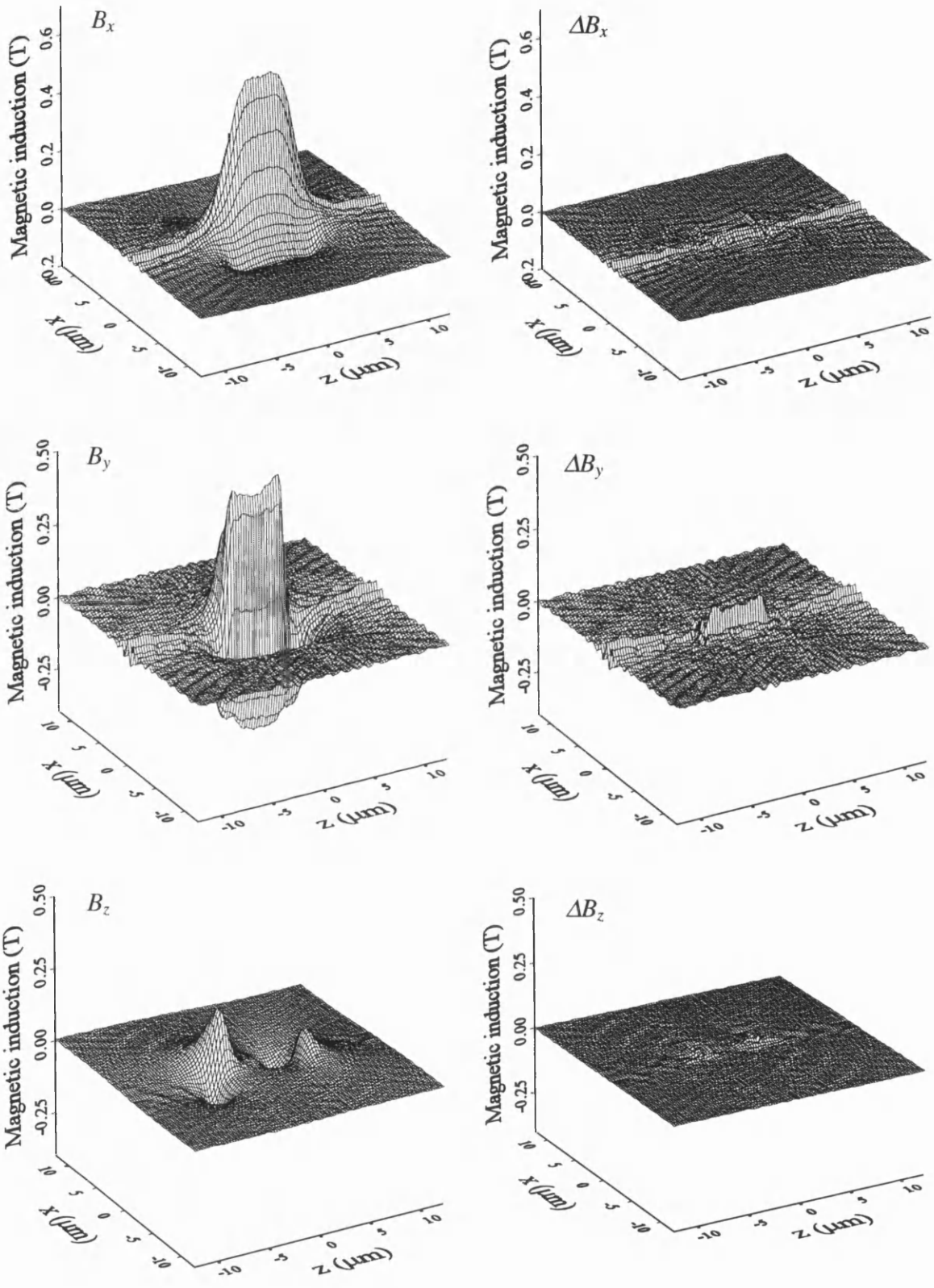

Fig. 4.7. *The field components reconstructed using ART and their absolute errors compared with the original shown in Fig. 4.1.*

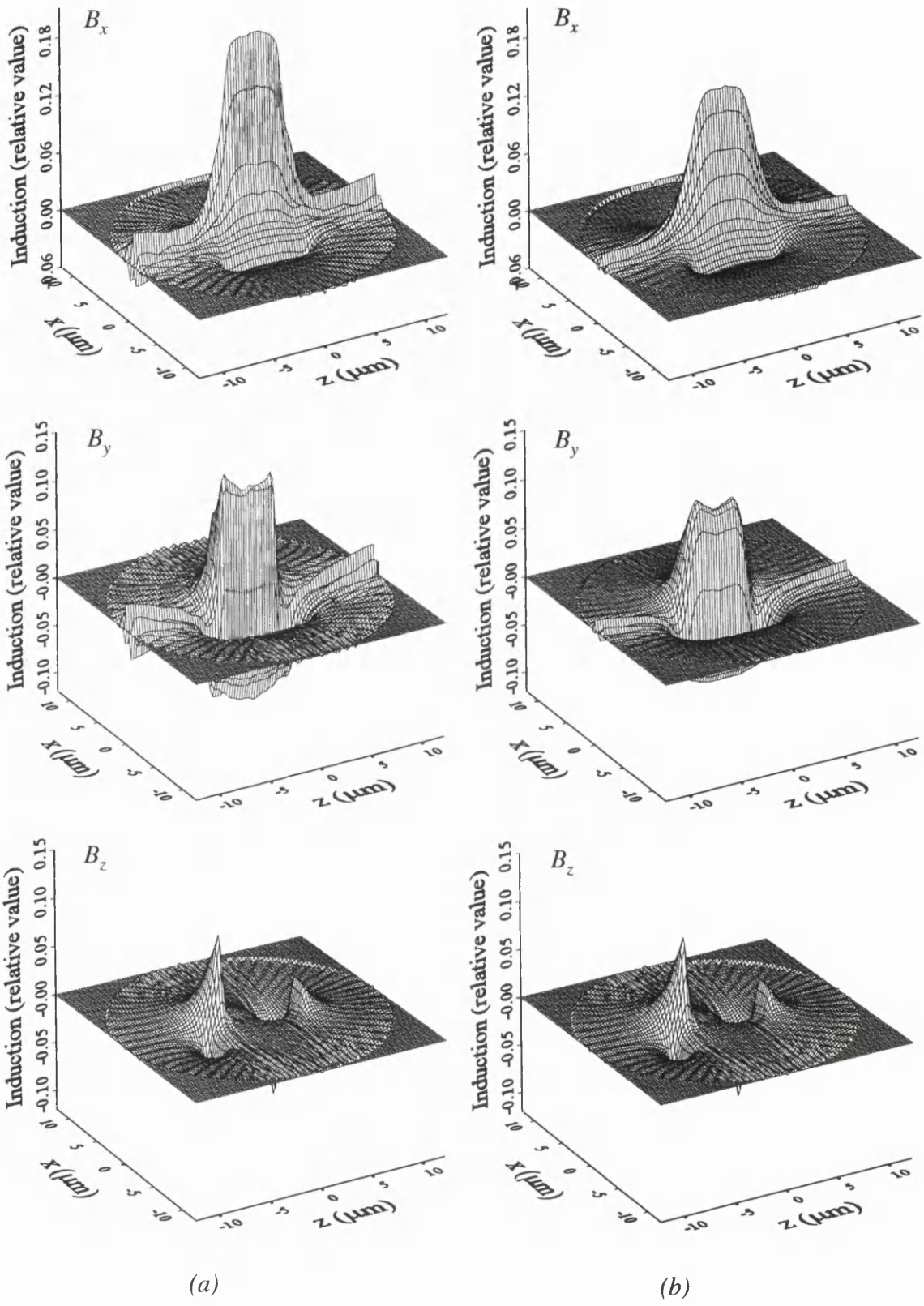

***Fig. 4.8**. Field components reconstructed by RTM using (a) tangential and (b) normal components of the electron beam deflection data sets at a distance of 0.5 μm from the ABS.*

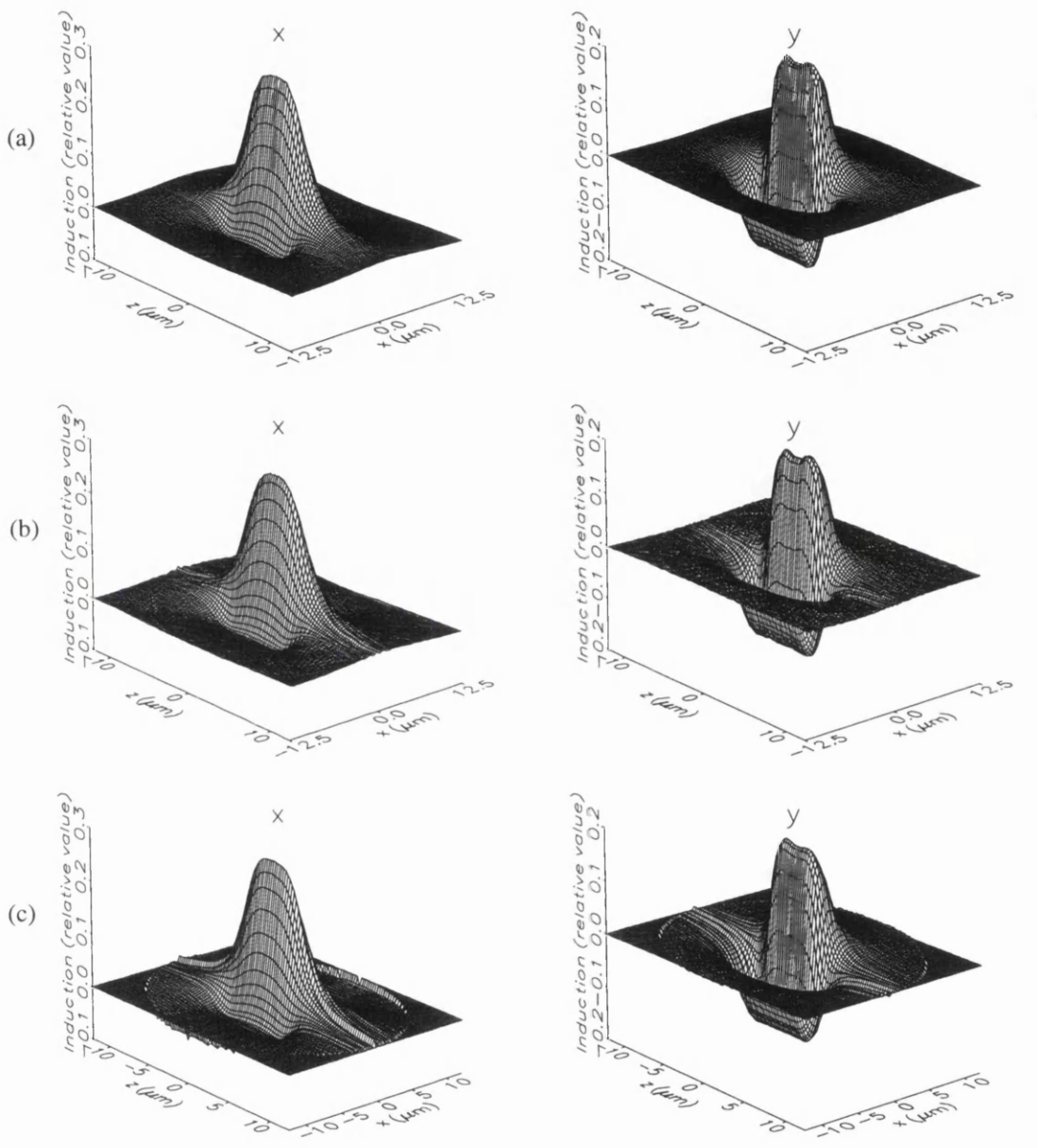

Fig. 4.9. *(a) The Bx, By field components of the model thin film head field at a distance of 1.0 μm from the ABS; (b) the field components reconstructed using ART; (c) the field components reconstructed using the RTM.*

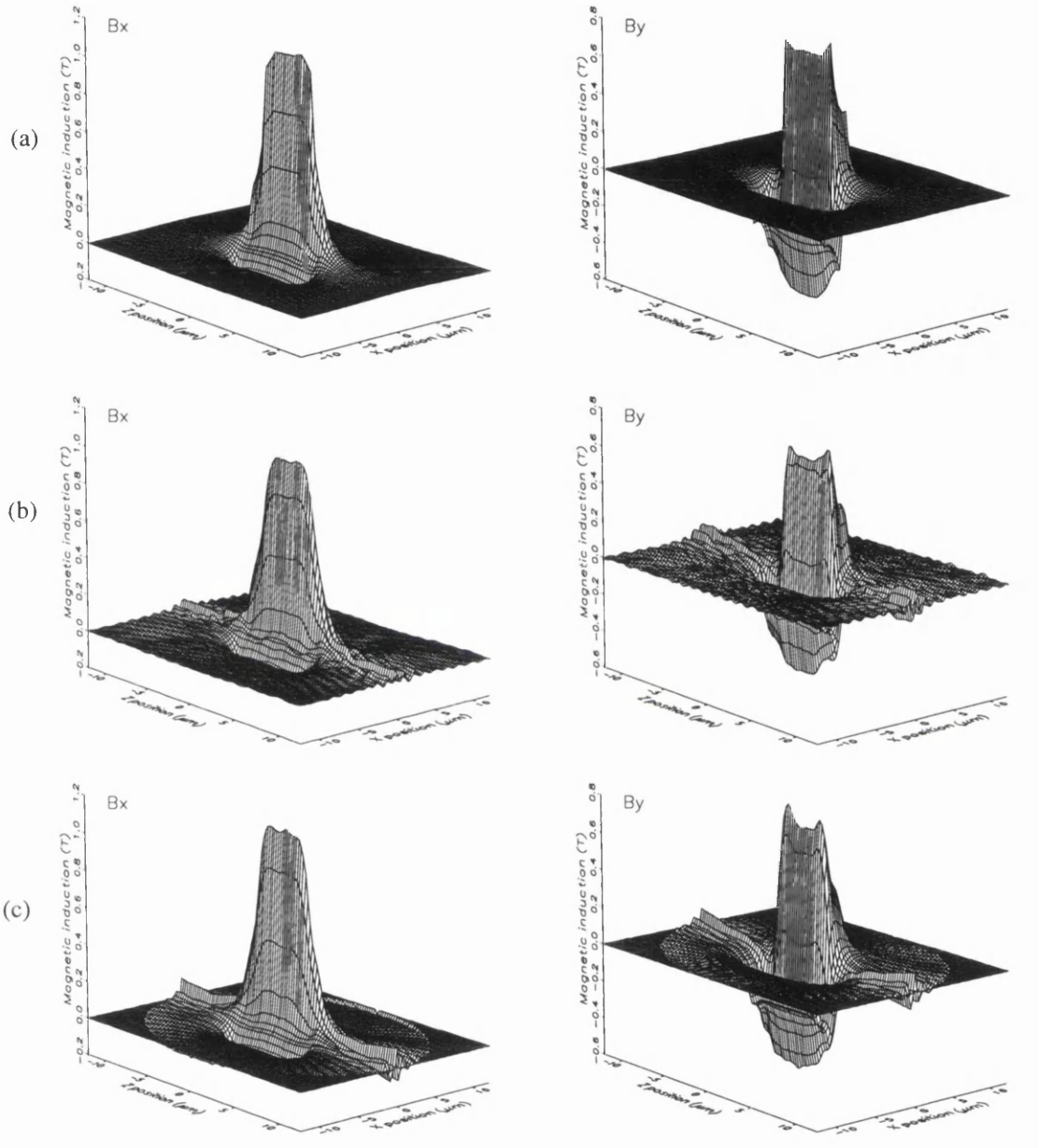

Fig. 4.10. *(a) The B_x, B_y field components of the model thin film head field at a distance of 0.25 μm from the ABS; (b) the field components reconstructed using ART; (c) the field components reconstructed using RTM.*

phenomena has been observed throughout the simulation and even some practical reconstruction. The nature of this problem is unclear as it is very difficult for us to go through the RTM code. The problem may be due to either some possible inconsistencies in dealing with the equations (3.18) and (3.19) in the RTM algorithm or the model thin film head fields are not perfectly harmonic, *i.e.*, the fields in the space outside the ABS are not perfectly consistent with equations (3.7) and (3.8).

Since the reconstructed results by the RTM are in relative values, we cannot evaluate quantitatively the reconstruction errors. However, comparing both Fig. 4.8 and Fig. 4.6 with the original field (Fig. 4.1), we can see that under the same reconstruction parameters the ART reproduces the original field better than the RTM. The reconstruction results from RTM have higher ripples along the head gap. Significant rippling effects were also observed by Steck [1990] in his simulations of a single turn coil field and the figures for the differences of ΔB_x, ΔB_y and ΔB_z reconstructed from both tangential and normal deflection sets are 14%, 8% and 9% respectively [Ferrier, 1992].

For not very defensible reasons the reconstructed fields by RTM were averaged for the x, y, and z components and field sets are consistent with the model field. These averaged fields together with the original and the reconstructed fields by the ART at distances of 1.0 and 0.25 μm from ABS are shown in Fig. 4.9 and Fig. 4.10 respectively. For both ART and RTM, the reconstruction are improved with the decrease of the magnitude of the stray fields. In general under the same conditions, the results from RTM reveal more ripple than those from ART.

4.3.3 Reconstruction by using different total rotation angles

An additional advantage of ART is that it can reconstruct the stray field with fewer projections. This may largely ease the experimental difficulties, as it is not always possible to have ±90° rotation of the object of measurement. We have tried to calculate the electron beam deflection data sets with different rotation angles and used them as the input to the ART tomography program. The reconstruction parameters are listed in Table 4.2 and the corresponding results are shown in Fig. 4.11.

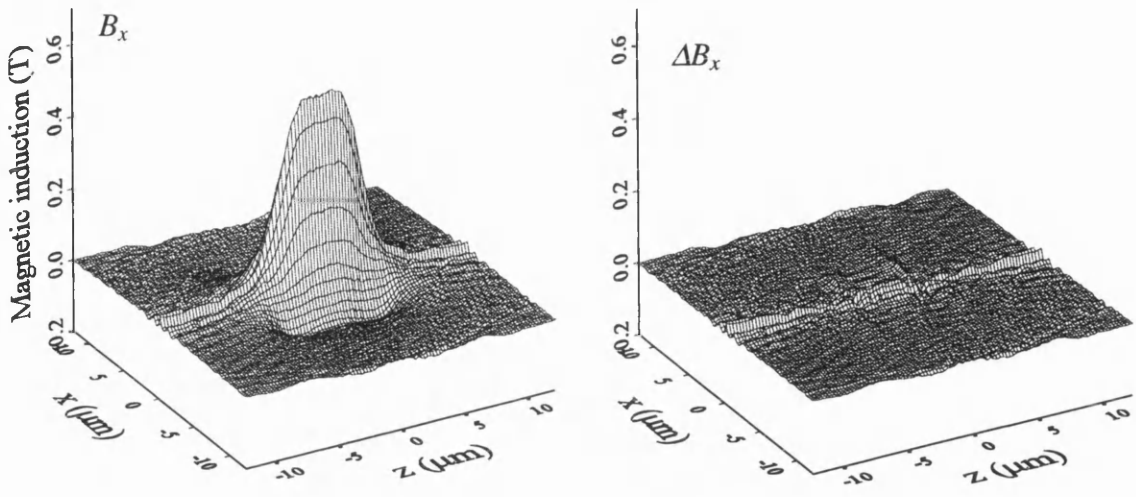

(a) 150°; m_θ=30

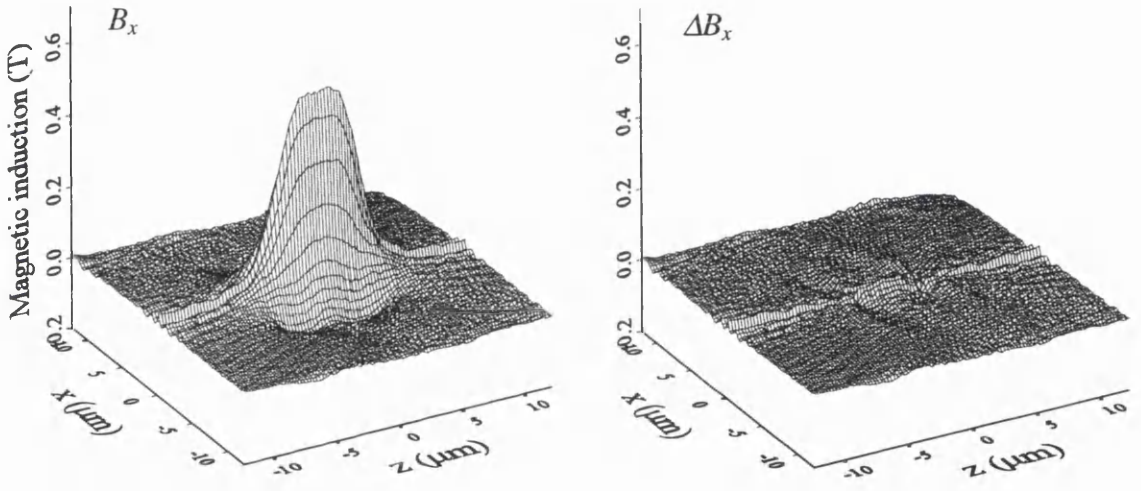

(b) 120°; m_θ=24

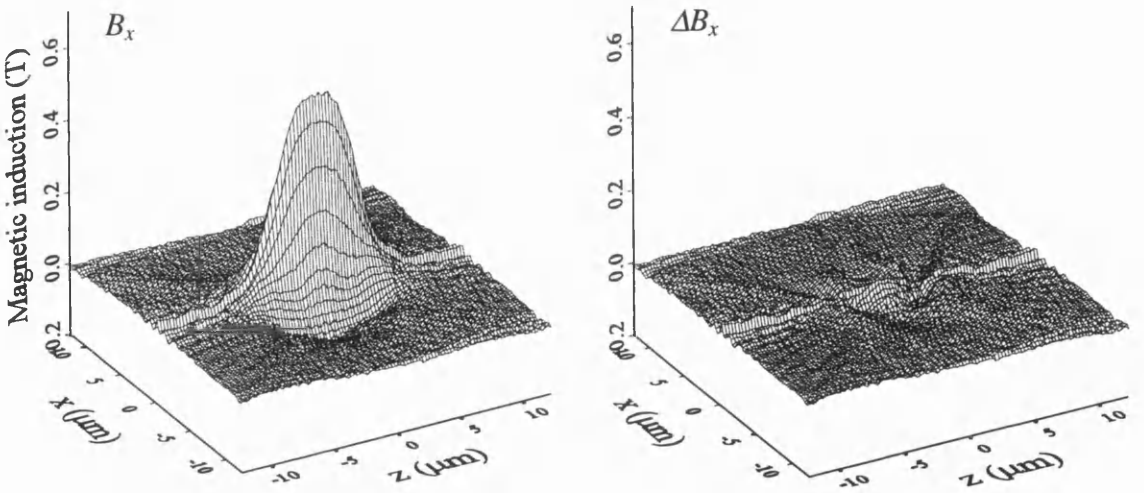

(c) 90°; m_θ=18

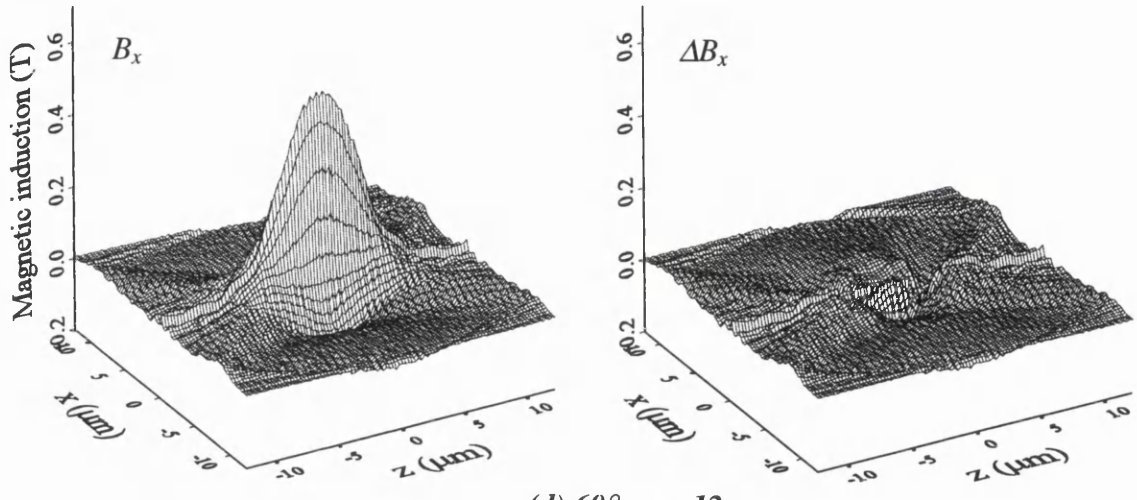

(d) 60°; m_θ=12

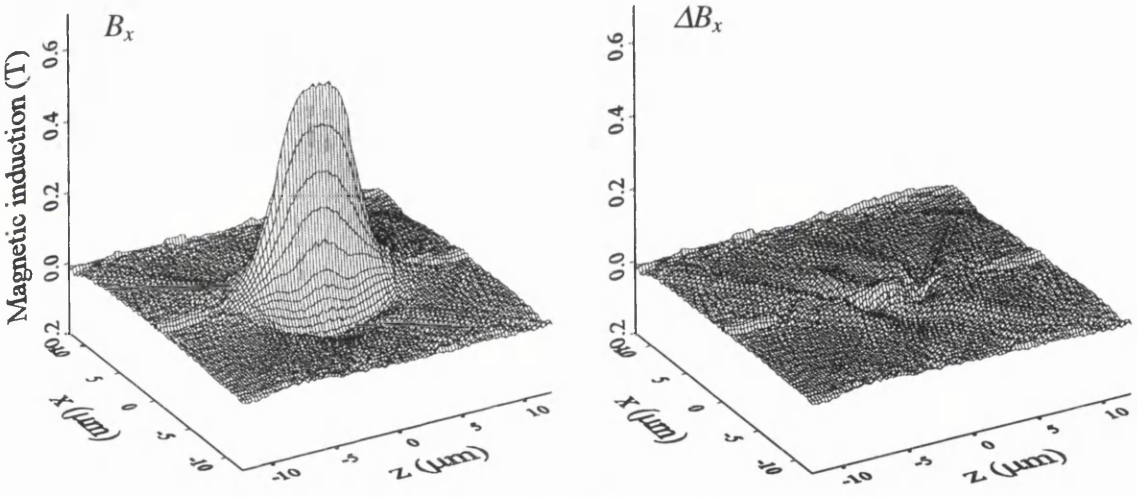

(e) 90°; m_θ=36

***Fig. 4.11**. The writing field component Bx reconstructed using ART and its absolute error for different rotation angles.*

Table 4.2

	a	b	c	d	e
Acceleration voltage (kV)	200	200	200	200	200
Camera length (m)	6	6	6	6	6
Number of scanning points m	99	99	99	99	99
Number of angular positions m_θ	30	24	18	12	36
Rotation angle (°)	150	120	90	60	90

Fig. 4.11 shows the writing field component B_x and its absolute error ΔB_x for different rotation angles. It can be see that even if the rotation angle declines to 120°, the reconstruction is still quite acceptable for the writing component. Continuing to decrease the rotation angle, the reconstructed field begins to lose the original features, *e.g.*, as measured by the field width at half maximum, the field peaks become narrower in Fig. 4.11.(c) and (d). It is also interesting to note that the ripples along the polegap remain almost unchanged from Fig. 4.11.(a) to (d), as that is a feature connected to the angular interval rather than the rotation angle. Indeed we see less ripples in Fig. 4.11.(e), for an angular interval half the original value (2.5°).

The quantitative evaluation of the effect of rotation angle is shown in Fig. 4.12. The extra points at the 90° position just below the curves are the errors for the reconstruction parameter set e in Table 4.2. It shows little improvement by decreasing the angular interval for the same rotation angle.

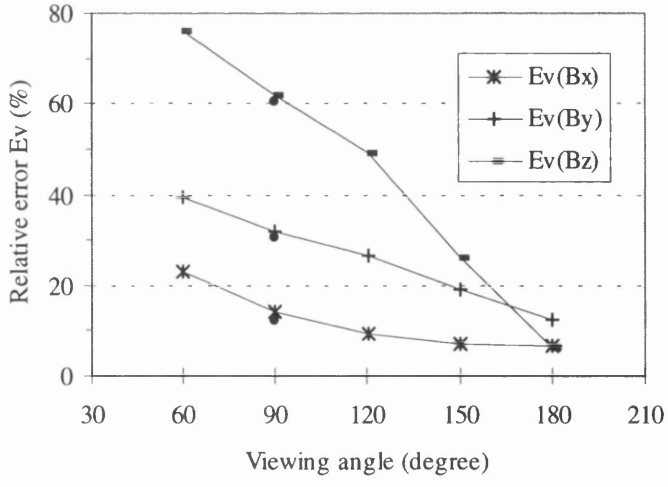

Fig. 4.12. *Reconstruction error of the ART as a function of the rotation angle.*

4.3.4 Reconstruction using different number of angular positions and scanning points

The reconstruction simulations were also carried out for different numbers of angular position m_θ, whilst the rotation angle is kept at ±90°. This implies the use of different angular intervals. The reconstruction parameters are listed in Table 4.3 and the corresponding reconstruction errors are shown in Fig. 4.13.

Table 4.3

	a	b	c	d	e
Acceleration voltage (kV)	200	200	200	200	200
Camera length (m)	6	6	6	6	6
Number of scanning points m	99	99	99	99	99
Number of angular positions m_θ	18	24	36	44	72
Rotation angle (°)	180	180	180	180	180
Angular interval $\Delta\theta$ (°)	10	7.5	5	4	2.5

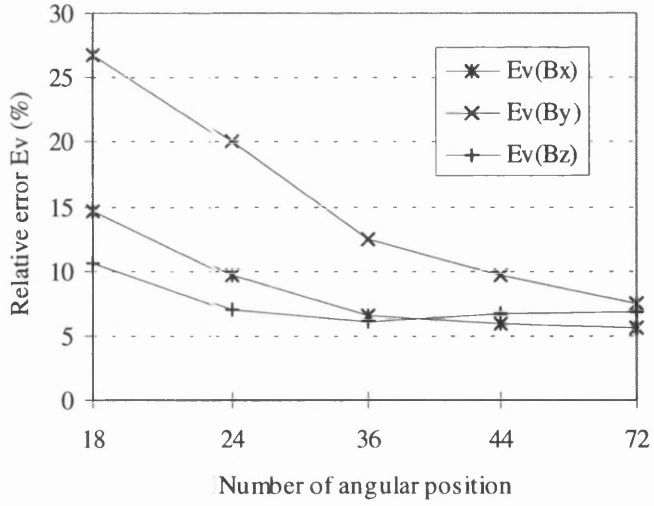

Fig. 4.13. Reconstruction error of the ART for different numbers of angular positions.

It is shown in Fig. 4.13 that the overall reconstruction errors decrease with the increase of the number of angular positions, but after 36 angular positions this decrease becomes very small, especially for components B_x and B_y. The field reconstruction for 72 and 18 angular positions are shown in Fig. 4.14. Together with the field reconstruction shown in Fig. 4.7, we can see that the more the angular positions the less the ripple in the background.

The reconstruction errors using different numbers of scanning points are listed in Table 4.4. These reconstructions are performed using rotation angle of ±90° and angular interval of 5°. We see very small differences between them even the number of scanning points has large change. It should be pointed out that in Table 4.4, ΔB_y increasing with the scanning points is a spurious effect. It arises because when fewer discrete points are used to determine the stray field where its gradient changes rapidly, the gradient will appear smaller and therefore the reconstruction accuracy increases.

Table 4.4

Number of scanning point *m*	Reconstruction error *Ev* (%)		
	ΔB_x	ΔB_y	ΔB_z
33	7.59	7.3	11.0
49	7.2	7.49	7.85
99	6.59	12.45	6.02

4.3.5 Reconstruction using truncated data sets

In experimental field determination from recording heads the field distributions seldom go to zero at the perimeter of the measurement plane and hence reconstruction has to be carried out from truncated data sets. We simulate this situation by omitting one quarter of the data point on each side of the electron beam deflection data shown in Fig. 4.2. The reconstructed field by both ART and RTM using such a truncated data set are given in Fig. 4.15 for field components B_x and B_y, together with the absolute errors of the ART

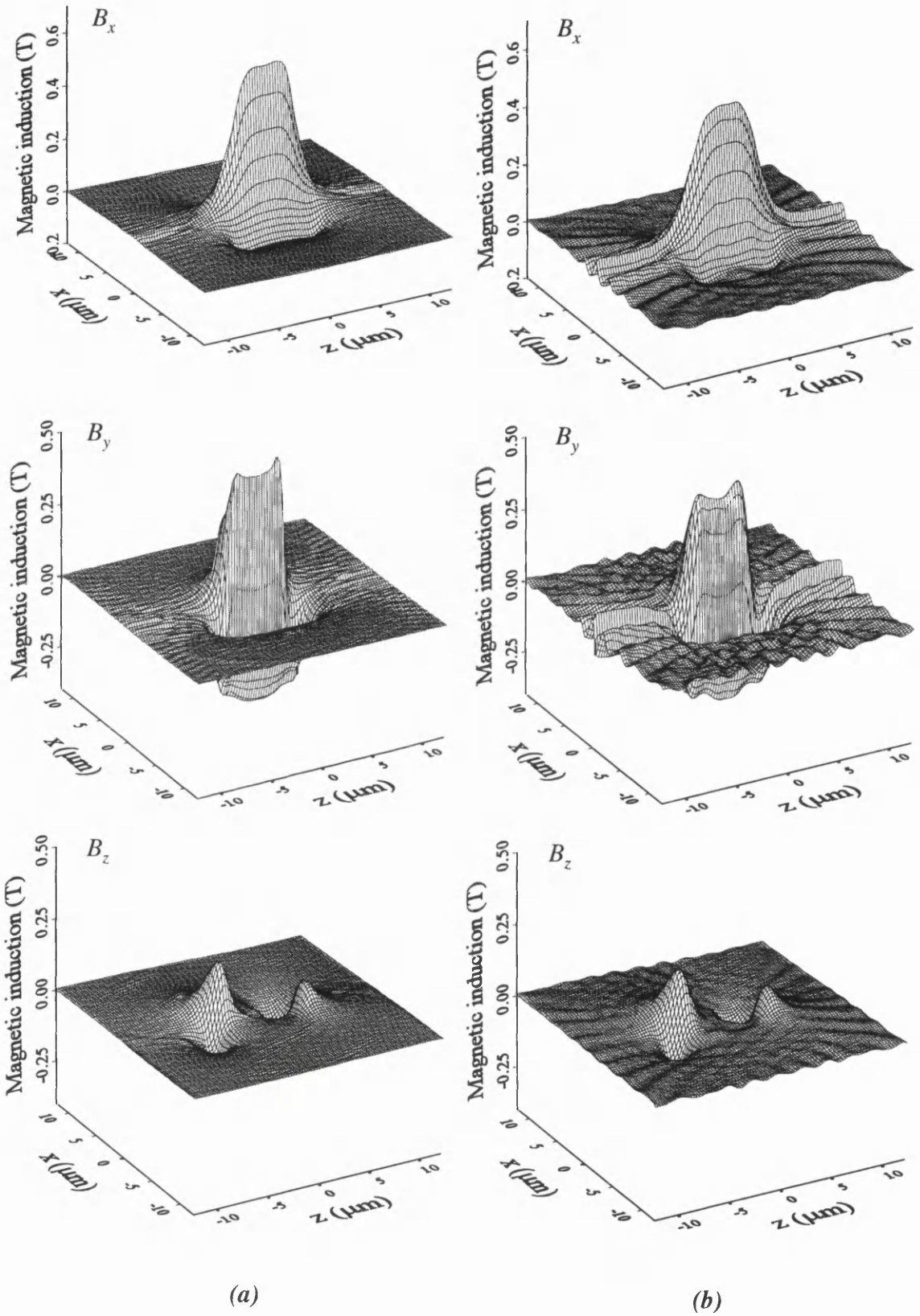

***Fig. 4.14**. Reconstruction of the model thin film head field at a distance of 0.5 μm from the ABS by ART using (a) 72 angular positions and (b) 18 angular positions.*

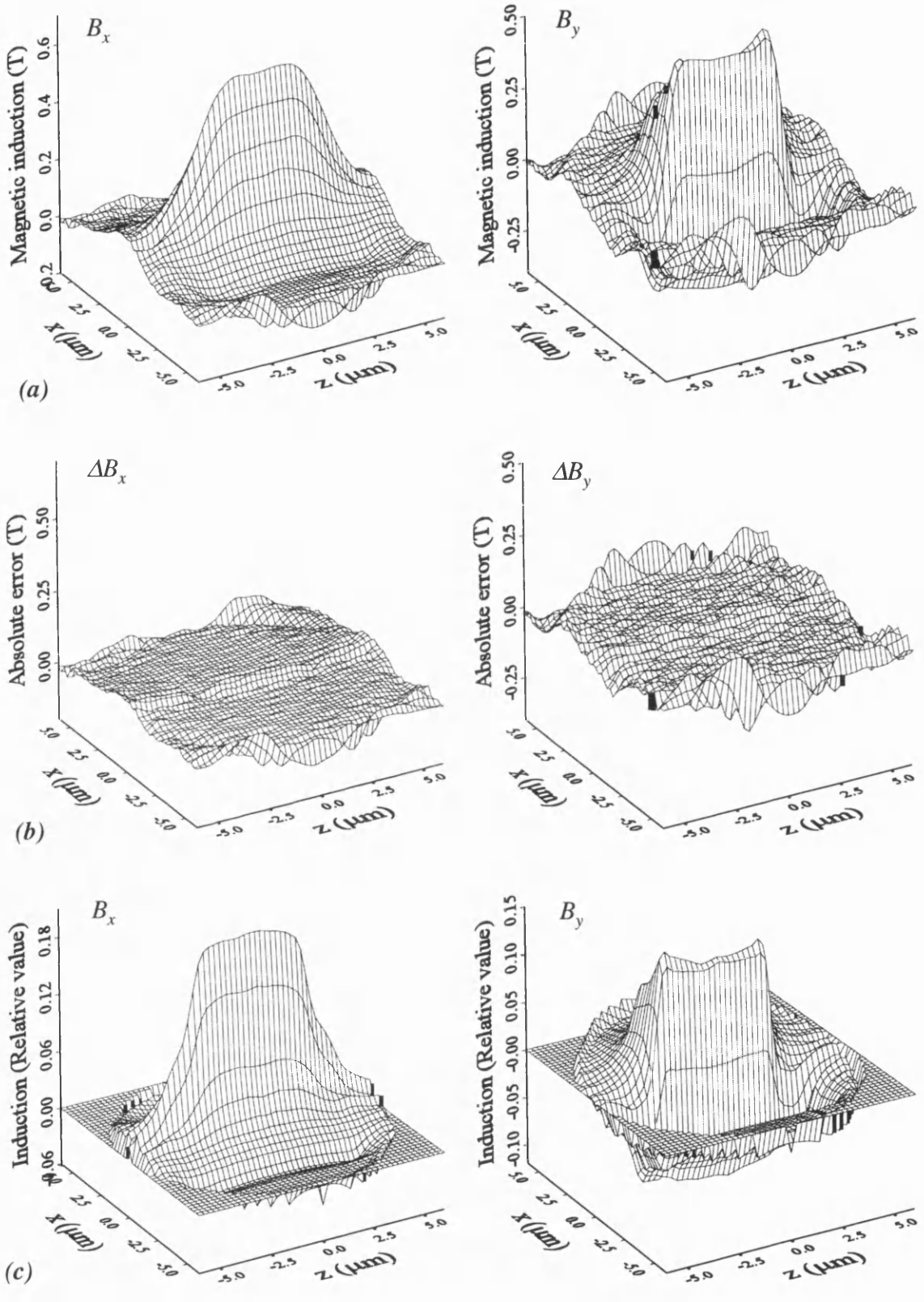

***Fig. 4.15**. The field components of B_x and B_y reconstructed using truncated data sets by (a) ART and (c) RTM, together with (b) the absolute errors of ART reconstruction.*

results. Since the field peak is the dominant factor for the electron beam deflection and the principle contribution remains within the area selected, and hence the information loss on the peak field is relatively small. The major reconstruction errors locate around the edge of the reconstructed region as the result of the restricted region of input data. Nevertheless, if our principle interest is the field peak, the reconstruction from truncated data set may still provide considerable information.

4.4 Conclusion

Computer simulations confirm that both the ART and RTM can provide satisfactory reconstruction of the recording head fields up to field magnitude of more than 1 T (field gradient ~2.5T/pixel). The reconstruction accuracy improves rapidly with lower field magnitude and gradient.

Our ART tomography program converges to steady solution at about 20 iterations. The reconstruction error is determined by the reconstruction parameters used. For the ART, detailed reconstruction requires that the rotation angle be bigger than 120°; using more angular positions m_θ (smaller angular interval $\Delta\theta$) at smaller rotation angle does not result in any clear improvement of the reconstruction. Having fixed the rotation angle, more angular positions m_θ helps to obtain smoother reconstruction and less ripples in the background. In general, 180° rotation angle and 36 angular positions (5° interval) are a good compromise for both the ART and RTM tomography programs.

Reconstruction from truncated data sets will result in bigger errors in the background, but the effect on the profile of the field is small provided the measurement plane is still large enough to cover the major field distribution.

References

Brebbia, C. A. and S. Walker (1980), *Boundary Element Techniques in Engineering*, Newnes-Butterworths, London.

Chari, M. V. K. and P. P. Silvester (1980), *Finite Elements in Electrical and Magnetic Field Problems*, Wiley, New York.

Ferrier, R. P. (1992), *Report on SUR Contract SL91459.*

Hoole, S. R. H. (1989), *Computer Aided Analysis and Design of Electromagnetic Devices*, Elsevier, New York.

Liu, Y. and J. Yi (1988), *IEEE Trans. Magn.*, **24**, 2994.

Steck, M. (1990), *Ph.D. thesis*, Duisburg University.

Trowbridge, C. W. (1988), *IEEE Trans. Magn.*, **24**, 13.

Chapter 5

Investigations of the stray fields from inductive thin film recording heads

5.1 Introduction

Since its advent in 1950's, the magnetic recording industry have constantly and dramatically increased the performance and capacity of hard disk drives to meet the computer industry's never-ending demand for smaller, faster, denser and cheaper storage. The read-write head technology that has sustained the hard disc drive industry to date is based on an inductive element, namely the head, to write data on the disc and retrieve previously-written data. These conflicting tasks have made the inductive head technology eventually approach performance limitations. Magnetoresistive (MR) head technology overcomes this problem by separating the write and read function into two physically distinct heads; an inductive head, optimized for writing information, is integrated with a MR structure optimized for reading. It is believed that this fundamental change in read-write technology will enable advances capable of carrying the disk drive industry well into the 21st century. Therefore the investigation of the inductive stray field, which is associated particularly with the writing performance, has become even more important with the emergence of MR head.

This chapter describes the experimental application of electron beam tomographic reconstruction methods to the studies of stray fields from production thin film heads. The input data are collected using DPC imaging in a STEM instrument. The contents of this chapter include the specimen preparation and the head mounting technique, the determination of experimental parameters as well as the results analysis.

5.2 Specimen preparation and head mounting technique

Advanced thin film read-write heads in volume manufacturing are fabricated using semiconductor-style processing technology [Miura *et al.*, 1980]. The head structures are built on top of a substrate (TiC) wafer. The wafer is then cut into individual heads and air bearing pattern is etched on the polefaces side of the substrate. The head and the ABS assembly is called a slider, which flies over the disk on a self-pressurised air bearing; with earlier technology flying heights are of the order of ~75 nm. A typical IBM thin film head is shown schematically in Fig. 5.1. This is a 50% comprising nano TiC/alumina slider with an etched pattern tri-rail MR head (1990), The size of the slider is of the order 2.5×1.6×0.45 mm and the dimensions of the poletips are ~7×4 and ~5×4 μm for the lower (P1) and upper pole (P2) respectively. We have dealt with several batches of IBM thin film heads, the geometries of the ABS and the dimensions of the poletips vary.

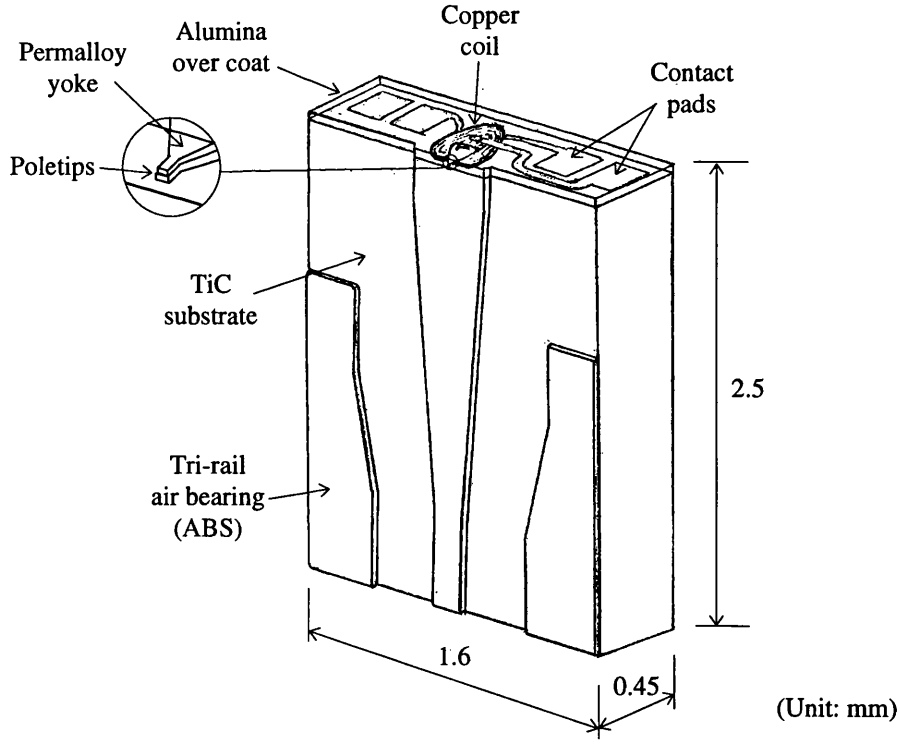

Fig. 5.1. Sketch of an IBM thin film head slider.

The head-to-medium spacing is commonly considered to be the principal limiting factor for areal density improvement, as the exponential decay of the writing signal with spacing over magnetisation wavelength places a strong upper bound on the spacing that can be tolerated. Therefore scaling the physical spacing between the head and the medium is as important as any other aspect of magnetic recording head design. With the progress in wear-resistant coatings for the head and the disk as well as in poletip recession or warped surface, the magnetic spacing could be scaled down to ~25 nanometers and eventually to "contact recording", which is defined as 10 nm [Grochowski and Thompson, 1994]. Hence the measurements of the stray fields need to be conducted as close to the ABS as possible.

Ideally we require to maintain the ABS strictly parallel to the electron-optic axis over the total angle of rotation (~180°) required to collect the complete data set for tomographic reconstruction. For a standard thin film head, such as the one shown in Fig. 5.1, the ABS is relatively extensive in comparison to the area occupied by the poletips, and in the severely restricted space available to us in the microscope in the vicinity of the specimen, it proved extremely difficult to construct a specimen rod with goniometer movement of sufficient precision to achieve the required accuracy of alignment. It is likely that similar difficulties have prevented some field reconstructions [Steck *et al.*, 1990] from approaching the ABS to a distance of less than ~3 μm, thus severely limiting the practical usefulness of the results.

There are in fact two experimental difficulties, the shadowing effect due to any misalignment of the ABS as the head is rotated over 180° and the determination of the single tilt axis of the specimen, which is ideally on the centre of the polegap and coincident with the specimen rod axis. A straightforward solution is to remove some of the material in the ABS and therefore make the poletips stand proud of the ABS plane, thus the shadowing effect can be eliminated and the alignment of the single tilt axis becomes more straightforward. Shinada *et al.* [1992] addressed this problem by using a combination of mechanical polishing and focused ion beam milling to create a 20 μm square region centered on the middle of the head polegap and standing ~5 μm proud of the previous ABS. In this way they managed to perform a field reconstruction as close

as 0.5 μm to the polefaces. Nevertheless, polishing of the rigid slider would be very difficult and time-consuming.

To avoid over-elaboration in specimen preparation, we have followed a different approach to the problem [Ferrier *et el.*, 1995]. Rather than attempt very precise alignment of the slider ABS, we have engineered a specimen holder in which the slider, separated from its cantilever support, is mounted on the end face of a specimen stub cut at a small angle to the normal. This small ramp, 5° in current studies, allows the slider to be mounted so that the electron beam passes parallel to the poletips as it traverses in the direction of polegap. In this way the shadowing effects from the ABS is eliminated. The specimen stub together with a schematic diagram of the mounting arrangement is shown in Fig. 5.2.

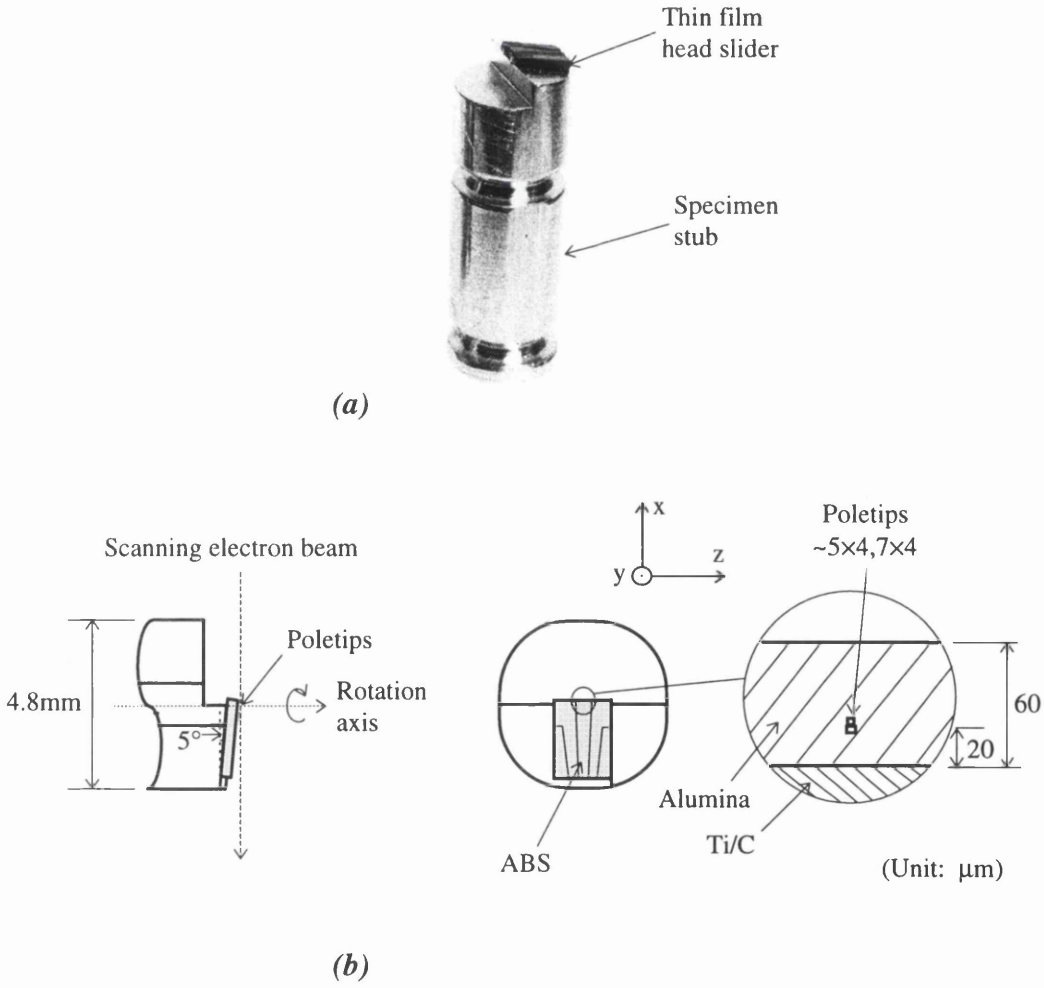

Fig. 5.2. *(a) The specimen stub and (b) the mounting arrangement of the thin film head.*

To achieve the required 180° rotation and obtain a full set of DPC images as the head is rotated at angular intervals about the specimen rod axis, four flats are milled on the stub parallel to its axis and at 90° to each other. These are used to locate the stub in a 'V' groove in the specimen rod and two positions at right angles can then easily be selected. This together with the accurate ±45° rotation of the goniometer stage permitted by the JEOL 2000FX allows us to collect a full data set with only one position change of the stub.

As can be seen from Fig. 5.1, the head structures are covered by a thin layer of alumina, which must be partially etched to prevent additional shadowing given that the slider is mounted at a small angle to the normal. The etching of alumina is performed by using heated *tri*-Sodium orthophosphate ($Na_3PO_4,12H_2O$) solution and the etching conditions are listed in Table 5.1. The etching rate of alumina is affected dramatically by the solution temperature and regular check is required using optical microscopy to obtain the desired depth of alumina etching. The etching solution has no effect on the permalloy yoke and the copper coils. An SEM image of the poletip region of a mounted thin film head following partial removal of the alumina is shown in Fig. 5.3. From the view point that the electron beam traverses at a small angle to the ABS, the poletips are now proud of the slider structure and this gives us an ideal reference to adjust the specimen tilt axis through the alignment of the eucentric height of the poletips. Therefore the two experimental difficulties in specimen preparation for the tomographic study of thin film recording head fields have been overcome.

Table 5.1

Composition of etching solution	0.2 Mol $Na_3PO_4,12H_2O$ in 1000ml distilled water
Temperature of etching solution	~80°C (using a hot plate stirrer)
Etching time	~50 minutes

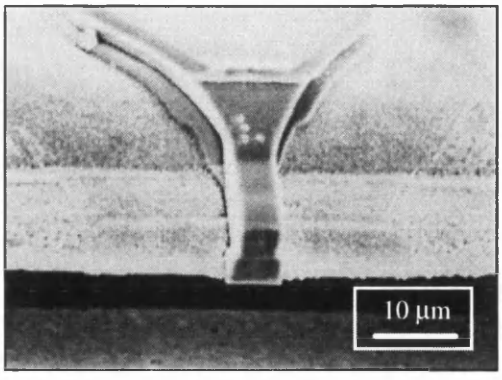

Fig. 5.3. *SEM image showing the poletip region of a mounted thin film head after partial removal of the alumina coat.*

After the etching process, the slider is mounted on the stub along a machined edge on the mounting plane to locate the slider so that the centre of the polegap is coincident with the stub axis. To avoid electrostatic charging, small amount of silver dag is applied to make the electrical connection between the slider and the stub. This mounted assembly is then coated with gold using a sputter coater. The coating process is performed twice from different directions to ensure that the whole poleface is covered with a layer of ~150 angstrom gold. After that the coated assembly is mounted in the 'V' groove in the tomographic rod and the wires, which are connected to the head coils, are soldered to the connection pads on the rod to permit the head to be driven with ac or dc current. The specimen is now ready for tomographic study.

The method described above does mean that the field reconstruction is strictly at a small angle to the ABS; we do not believe that this is a serious drawback and it certainly removes major experimental difficulties. In fact, since the stray field from the thin film head is concentrated in the polegap region, the field reconstruction at a small angle to the ABS only brings about a very small change to the field peak and this effect can be minimized by varying the angle of the line scan relative to the pole-edges [Liu and Ferrier, 1995]; further detailed discussion about this will be given in section 5.4. In addition, etching of the alumina has the benefit that the field escaping from the steeply sloping regions away from the poletips may now be explored (section 5.4).

5.3 Experimental parameters and magnetic contrast

The principle and technique for DPC image collection have been discussed in chapter 3. The emphases of this section are placed upon the determination of experimental parameters and the acquisition of correct magnetic contrast.

The resolution and precision of DPC Lorentz microscopy are determined by the probe size of the electron beam in the stray field region and the signal-to-noise ratio. Using the digital technique of DPC Lorentz microscopy to acquire the contrast image of the magnetic stray field, the image resolution and precision are also dependent on the scanning step length and the precision set for A/D conversion. For recording head field study, 16 bit (65536 grey scales) precision is sufficient compared to the S/N ratio, whilst the choice of imaging resolution is connected to the image magnification used. Under the same imaging resolution higher image magnification provides finer resolution of the measured object, but the requirement that the field distribution has to remain within the reconstructed or the DPC image area puts an upper bound on the image magnification which can be used. In some cases the stray fields from recording heads extend so that the reconstructions have to be performed from truncated input data sets, e.g. the tape head fields which will be discussed in chapter 6. As has been discussed in section 4.3.5, so long as the principal contribution to the stray field remains within the area selected, the reconstruction may still provide considerable information. In extreme situations more than one DPC image at each angular position may have to be acquired to cover wider field distributions but this adds difficulty in terms of the amount of data processing and the image adjustment required.

To reduce the statistical error, the pixel dwell time of the electron beam and the image integration must be adjusted; however account has to be taken to the total sampling time for a full set of DPC images. A typical set of imaging conditions for the study of recording head fields is listed in Table 5.2 and gives rise to a total acquisition time of ~5 hours, to which must be added time for microscope adjustment, specimen changes etc. Therefore the stability of the DPC signals is crucial. Any possible variations in the signal level of the DPC image pairs must be recorded to act as a

reference for later data processing. In practice, for the JEOL 2000FX after about one and half hours warming up with the filament switched on, the DPC signals become stable and the variations of the signals on the oscilloscopes are usually undetectable.

Table 5.2 *Typical DPC imaging parameters*

Image resolution	256×256 pixels
Image A/D conversion precision	16 bit/pixel
Pixel dwell time	500 μs
Image integration	4 times

Non-magnetic contrast is another source of 'noise' in the DPC imaging technique; this is usually due to de-scan effects or electrical interference. Ideally when the DPC image is formed, in the absence of any driving current in the head, the intensity of the image in free space should be uniform; this requires a de-scan correction to be applied in the microscope (section 2.4.1). Unfortunately at the relatively low magnification (5000× ~ 10000×) at which we must operate, it is very difficult to achieve satisfactory de-scan performance and hence contrast does arise, unrelated to the head stray field. Electrostatic charging may also produce additional modulation to the phase of the electron wave. Since most of the noise is basically time independent, they can easily be removed by digital recording of a pair of DPC images with the direction of the dc current in the head coil reversed between image acquisitions. The magnetic contrast will be reversed in these images, but any other time-independent noise contrast will not and hence image subtraction provides a corrected image contrast. If hysteresis effects are suspected or indeed to be studied, subtraction of a pair of images, one with the head excited and the other with no driving current following an ac demagnetisation processing will also achieve a satisfactory result. As an example, Fig. 5.4 shows how the de-scan and the non-magnetic contrasts are removed by such image subtraction.

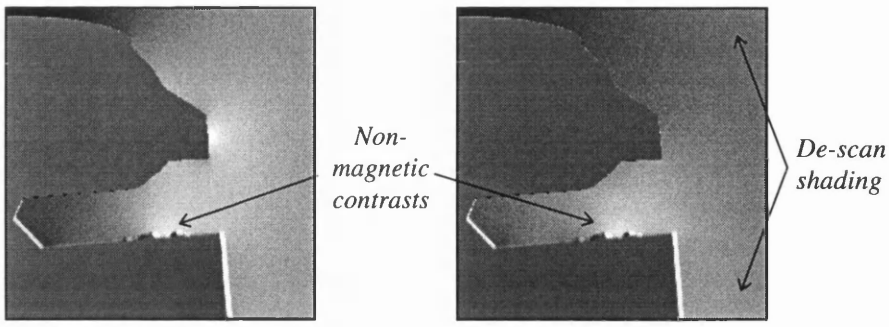

(a). $I_a = I^+ + I_{noise}$ (b). $I_b = I_{noise}$

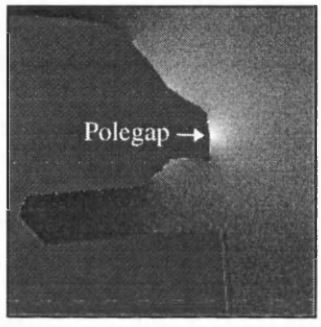

(c). $I_c = I_a - I_b = I^+$

Fig. 5.4*. Subtraction of a pair of DPC images (a) and (b) with time-independent non-magnetic contrasts (I_{noise}) but different dc driving currents (I^+, 0) gives rise to the corrected image (c) with pure magnetic contrast.*

5.4 Experimental results

The thin film heads studied in this section were of a conventional OEM type supplied to us by IBM Storage System Division, and had poletip dimensions ~5.0×4.0 μm and ~7.0×4.0 μm, with a polegap of 0.25 μm. There were 36 turns in the head coil. The heads were investigated using DPC Lorentz microscopy and the experimental conditions are listed in Table 5.3.

Stray field reconstruction on a plane at 5° to the ABS

The small ramp of the head mounting plane means that the head field is reconstructed on a plane at 5° to the ABS as shown schematically in Fig. 5.5. The reconstruction plane

in Fig. 5.5 is parallel to the P2 poletip edge along the polegap direction and at an angle ~80° to the image raster lines (section 3.4.2). Hence the closest distance to the centre of the polegap is restricted by the upper edge of P2 and can be calculated to be 0.35 μm in this case. Using 256×256 imaging resolution the digital step length is 0.25 μm, thus the nearest distance we can go to the centre of the polegap is between 0.35 to 0.6 μm.

Table 5.3: Experimental conditions of DPC Lorentz microscopy

Acceleration voltage (kV)	200
Image magnification	5000
Condenser aperture (μm)	200
Imaging resolution	256×256
Imaging A/D conversion precision	16 bit/pixel
Imaging integration	4
Head drive current (dc-mA)	±1, ±2, ...±14

Lens set up	C1	C2	CM	OBJ	OM	I1	I2	I3	Proj
	7.83	5.28	0.02	3.65	4.18	3.03	2.76	0.07	8.07

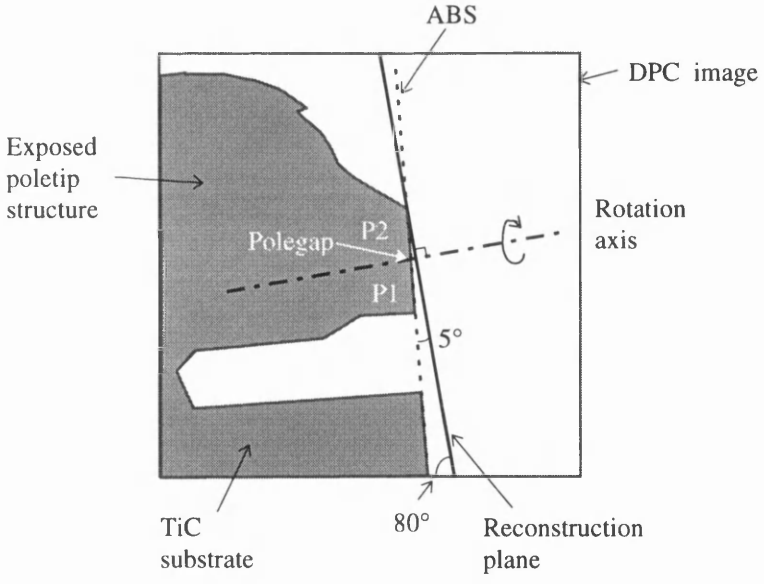

Fig. 5.5*. Schematic of the geometric elements in the DPC image, in which the optic axis is parallel to the polegap and normal to the image plane.*

All the DPC images were rotated by 10° clockwise to make the reconstruction plane normal to the image raster lines, and then vertical line scans were extracted from pairs of DPC images over the 180° tilt region at one pixel from the upper pole edge. As small translational drift was unavoidable from image to image, the line scans were aligned by visual inspection of superimposed line traces on a graph (section 3.4.3) to obtain a common single tilt axis. The aligned line scan data sets form the input for tomographic calculation and the field components reconstructed by using the ART and the RTM tomography programs are displayed in Fig. 5.6 in relative values.

Using a quadrant detector to acquire DPC signal the contrast in the image is a relative value, which provides information on the in-plane variation of the stray field. For recording head field study, it is equally important to have quantitative determination of the stray field. This requires the contrast calibration during the DPC image acquisition and will be discussed in chapter 7.

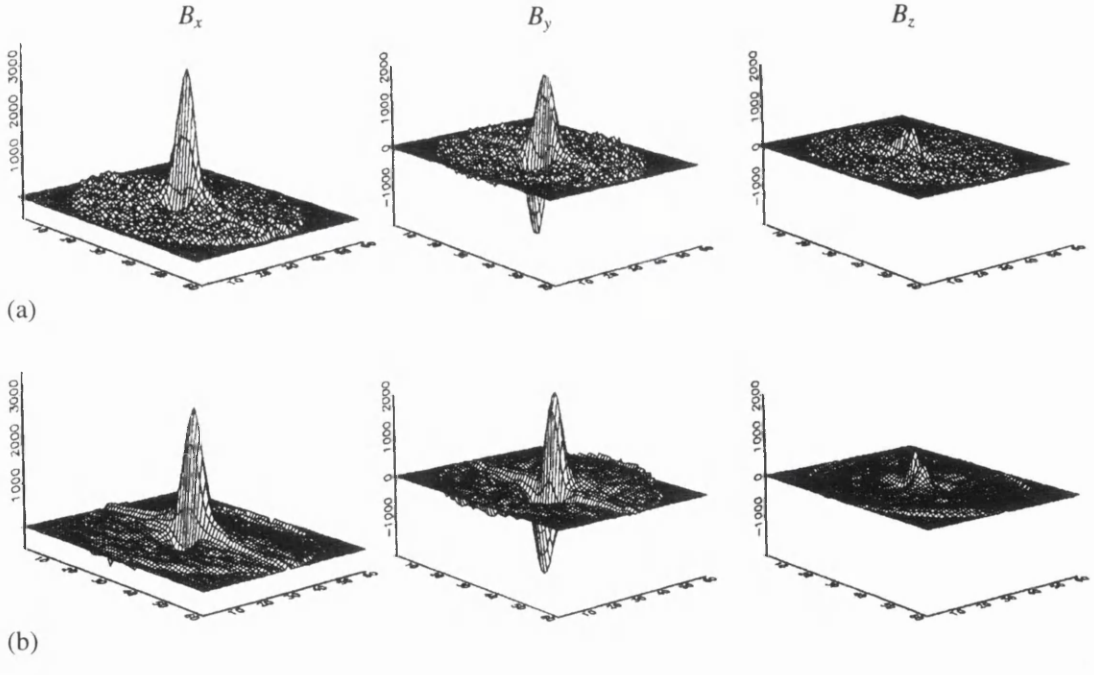

***Fig. 5.6**. The values of the components of an OEM thin film head field on a plane at 5° to the ABS and ~0.35~0.6 μm from the centre of the polegap: (a) reconstructed using the ART method, and (b) the averaged values from the RTM method .*

Stray field reconstruction at a closer distance to the polegap

In analysing the DPC images of the head field we found that we can vary the angle of the line scan relative to the poletip edges without substantial error in the reconstruction. In particular for the angular region of ±15° about the position where the polegap is parallel to the optic axis the line scans can be essentially parallel to the ABS, see Fig. 5.5. DPC Line scans taken at 5° and parallel to the ABS at the same distance (two pixels) to the centre of the polegap in the head orientation shown in Fig. 5.5 are presented in Fig. 5.7. As can be seen from Fig. 5.7, the difference of such line scans is very small indeed. Since the DPC data from these angular positions have the dominant influence to the field amplitude, we believe that the reconstruction from such line scan data sets will to a very good approximation represent the field distribution on that plane.

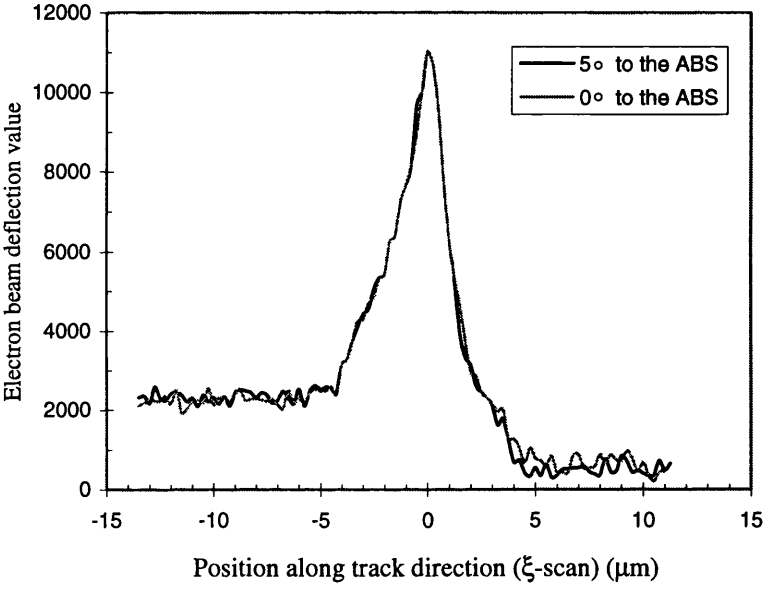

Fig. 5.7. *DPC Line scans taken at two different angles to the ABS but the same distance to the centre of the polegap.*

According to above-mentioned assumption, the reconstruction from such line scan data sets may be regarded as the stray field distribution on a plane essentially parallel to the ABS, therefore the minimum distance from the reconstruction plane to the centre of the polegap is one pixel which is equivalent to 0 ~ 0.25 μm. A complete set of the DPC line scans taken at one pixel away and parallel to the edges of the polefaces

are shown in Fig. 5.8. The field components reconstructed using the ART are displayed in Fig. 5.9; graphic plots together with grey scale images, in which grey represents zero field, are shown together with an indication of the relation to the poletips. As has been proved by the simulation (section 4.3.5), although the stray field did not go to zero at the edge of the reconstructed area, especially the component normal to the poleface as shown in Fig. 5.8, the reconstructed field is quite satisfactory as the result that the principal distribution of the stray field is within the reconstructed area.

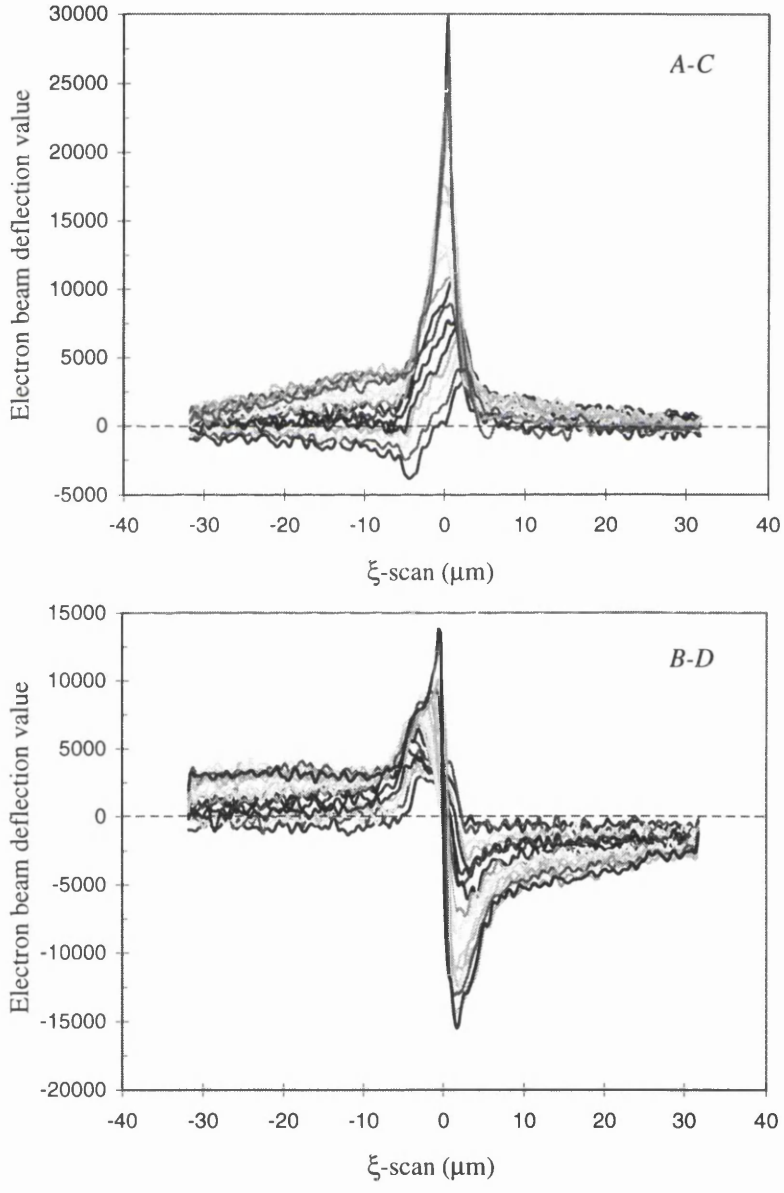

Fig. 5.8. *Line scans taken from the experimental DPC image pairs at ~0.25 μm from and parallel to the ABS around the polegap orientations or to the poleface edges elsewhere.*

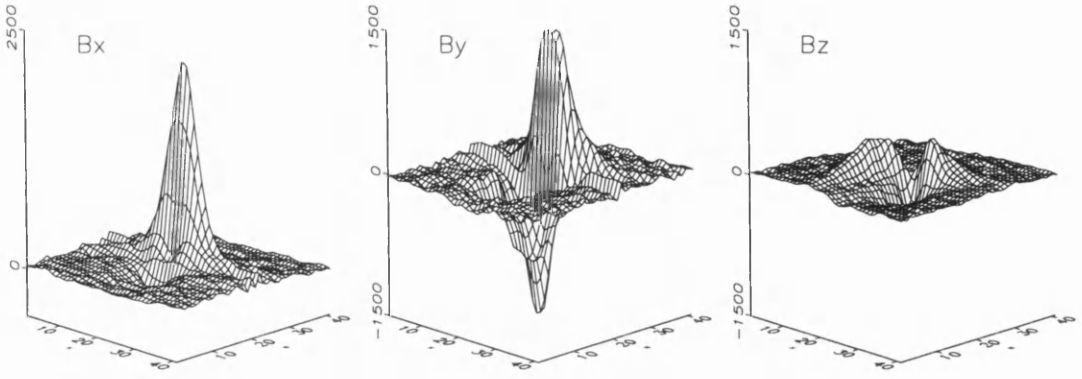

(a)

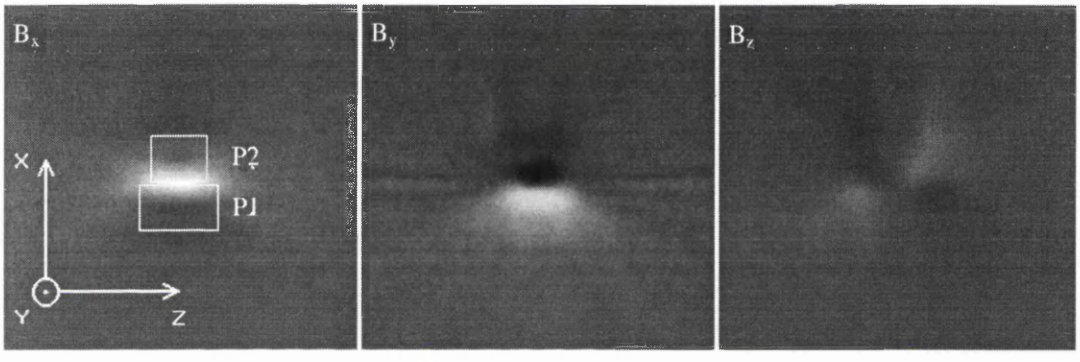

(b)

***Fig. 5.9**. Reconstructed field values of the OEM thin film head field on a plane ≤0.25 μm from the polegap and a dc current of 2 mA using the ART; (a) in the form of 3-D surface plots; (b) in the form of 2-D grey scale image with an approximate location of the poletips and coordinate axis.*

In principle field reconstruction on a plane with even closer distance to the polegap is possible by using higher image magnification, given that the image resolution determined by the electron probe size in the stray field region is smaller than that distance. As required by the tomographic algorithm, the principal field distribution must be within the area covered by the DPC images, this means that image overlapping at each angular position may be required to cover the extent of the stray field. However in practice this will add difficulty to image alignment and bring about enormous increase in data processing.

Analysis of the reconstructed field

From the reconstructed field data, further detailed analysis may be carried out to obtain more information about the field features. Achievement of higher areal density of information storage involves both linear density improvement and track density improvement [Tsang, 1991]. From the point of view of recording head fields, linear density improvement needs stronger and sharper writing fields which are required for higher coercivity media; track density improvement requires tight side-writing and side-reading behaviour [Tsang *et al.*, 1996]. Information on both features can be extracted from the reconstructed data in the form of the amplitude/gradient and contour of the writing component.

The profiles of the reconstructed fields along the centre line of the poles at ~0.5 and ~0.25 μm from the ABS are shown in Fig. 5.10 together with an indication of the location of the poletips. The general forms of these profiles are as we expect and are compatible with many modeling results [e.g., Mee and Daniel, 1987]. The reverse fields associated with the leading pole and trailing pole edges cut into the extent of the fields associated with the gap, in this way the gap field is narrowed and gradient of the field made sharper, significantly affecting resolution in writing. The negative portions of the writing fields at the poletip edges are obvious and due to the magnetisation at the edges being not of phase with the magnetisation at the polegap region. These extra pulses may cause anomalous amplitude variations in bit response of the inductive thin film head as linear density increases, however these oscillations in head output can be decreased by beveling the head edges [Yoshida *et al.*, 1993] or by applying an additional low permeability layer on both sides of the poletips [Shakurai *et al.*, 1994].

It is also noted that there are small peaks in the x and y distribution near the corner of the poletip edges (P, P' in Fig. 5.10.(b)) as the reconstruction plane is ≤0.25 μm from the ABS. Although the origin of these field features remains unknown, they are certainly very localised and may be linked to domains near the edges which are effectively pinned and provide flux closure resulting in distortion of the writing field. An attempt to carry out detailed study on the domain structure and domain wall dynamics of the head by backscattered electron imaging [Ferrier *et al.*, 1990] was aborted after the head was damaged accidentally.

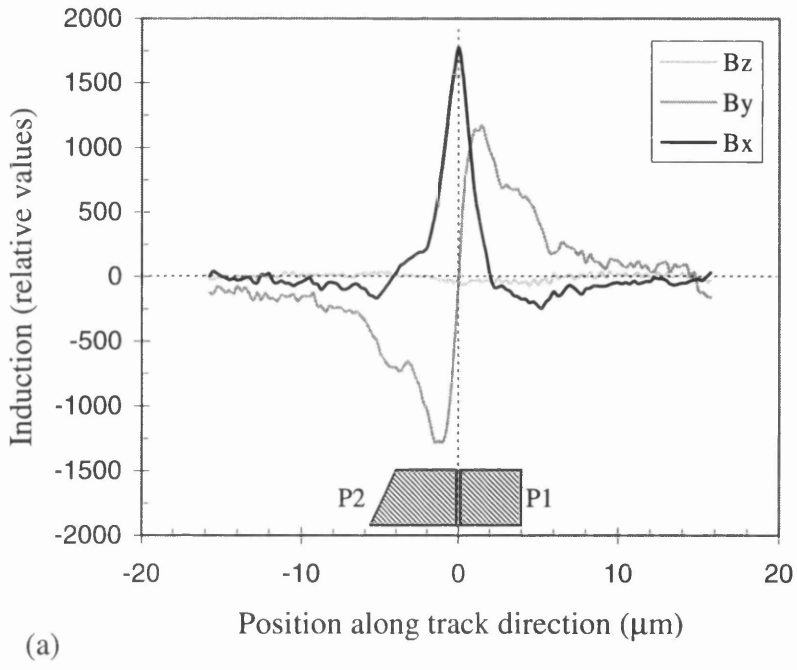

(a)

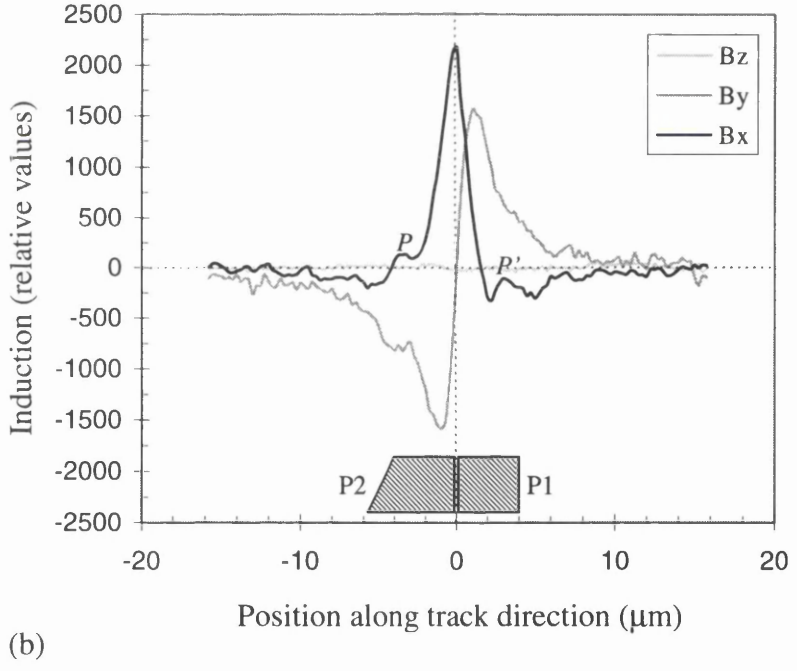

(b)

***Fig. 5.10**. Line traces of the reconstructed stray fields along the centre line of the poles, at distances of (a) ~0.5 μm and (b) ~0.25 μm from the ABS and a dc current of 2 mA.*

As the poletip dimensions of the thin film head continue to shrink, the side fringing field from the write head becomes increasingly important [Arnoldussen *et al.*, 1991]; the head writes to the side as far as the stray field is equal to the coercive force of

the medium, $|H|=H_c$, and degrades any old information slightly beyond that point in the process. To study the side write effect of a recording head, the contour map of the writing field at the level of the coercive field of the medium is essential. The amplitude contours of the writing field at ~0.25 μm from the ABS are shown in Fig. 5.11, where the ABS view of the poletips is also superimposed on the field contours. If the amplitude of the stray field is calibrated, which will be discussed in chapter 7, these writing field amplitude contours can provide useful information for the studies of side read/write effects.

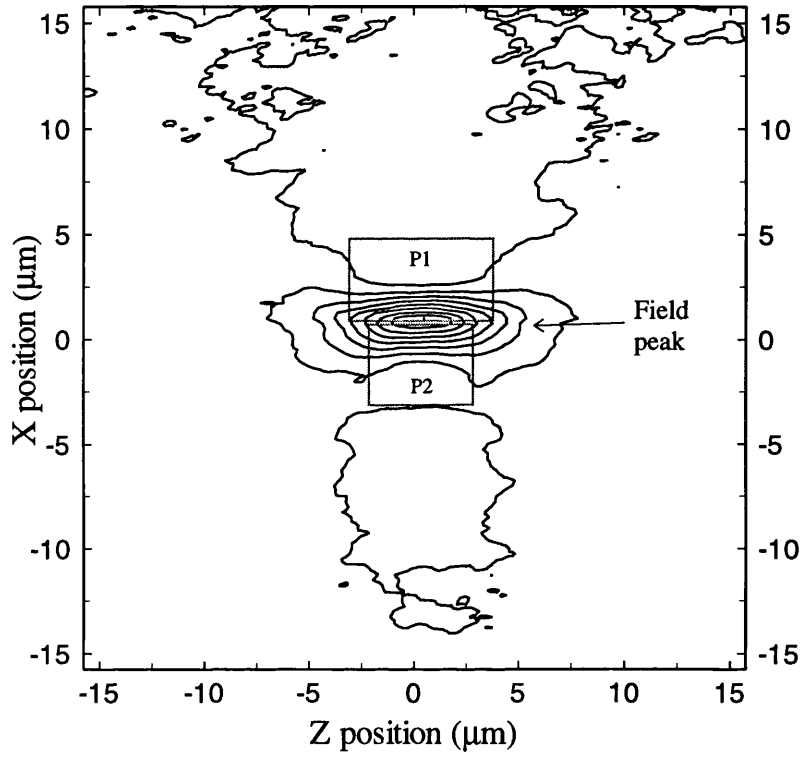

Fig. 5.11. Contours of the writing field B_x on a plane of ~0.25 μm from the polegap together with an indication of the ABS view of the poletips.

The saturation behaviour of the poletips

The collection of the complete data sets for 3-D reconstruction is time-consuming. Much additional information about the integrated stray field can be obtained in a very straightforward manner by detailed study of the head orientation where the optic axis is parallel to the polegap. Since we have chemically etched much of the alumina in the vicinity of the poles, we can now in this orientation observe not only the effect of the

field beyond the ABS, but also the effect of flux leakage from the sloping region of P2 and quantify this as a function of dc driving current. A series of DPC images in this head orientation for different driving currents is shown in Fig. 5.12, the contrast in the case of Fig. 5.12.(a) being sensitive to the component of magnetic induction in the write direction (x-axis), that for Fig. 5.12.(b) being sensitive to induction in the y direction. It is immediately obvious that there is a development of the magnetic flux escaping from the sloping region of the poles. Line traces of Fig. 5.12.(a) at ~0.25 μm (one pixel) from and parallel to the poleface are shown in Fig. 5.13 and clearly demonstrate that the influence on the profile on the P2 pole side is very large. It should be noted that because we are plotting the integral of the field along the electron beam trajectory the peak is broader than shown in Fig. 5.10. It can be seen from Fig. 5.13 that the stray field on the P2 side increases linearly with the driving current and this is an indication of saturation. This observation is consistent with some modeling work [e.g., Zak *et al.*, 1996] and experimental results that the magnetic saturation takes place earlier in the sloping region of P2. The intensity of the integrated x field component at the middle of the polegap as a function of the driving current is shown in Fig. 5.14 and indicates that the onset of saturation of the poletips occurs at a current around 7 mA, which is equivalent to 0.25 ampere turns. Similar partial "BH" loops may be obtained for any other point in the distribution.

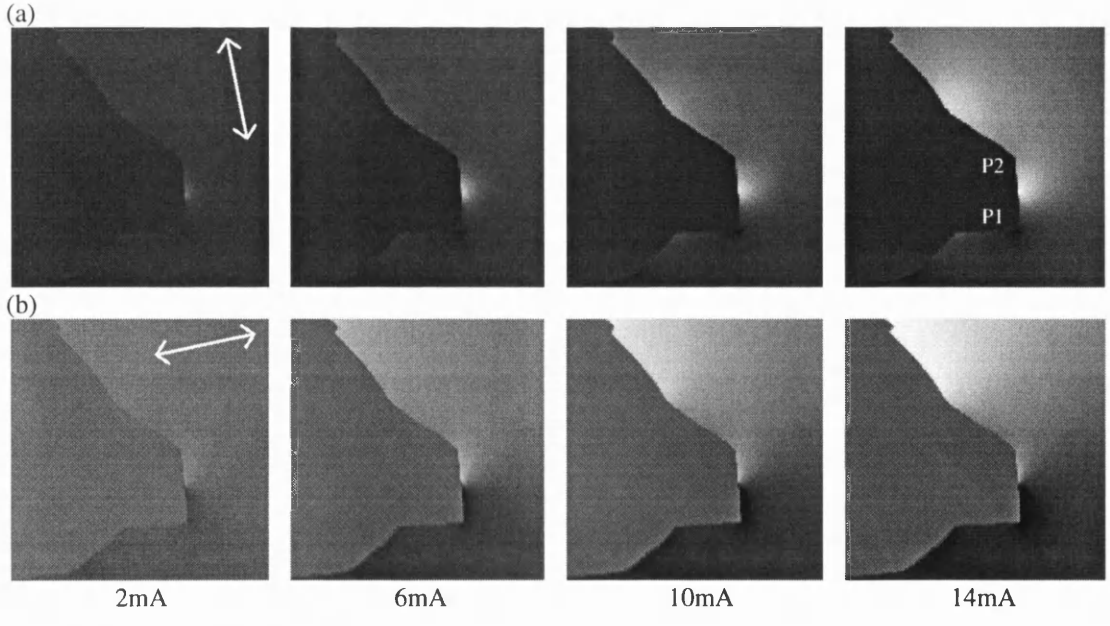

Fig. 5.12. *Series of DPC images for different dc driving currents, the contrasts are sensitive to the components of magnetic induction indicated by the arrows.*

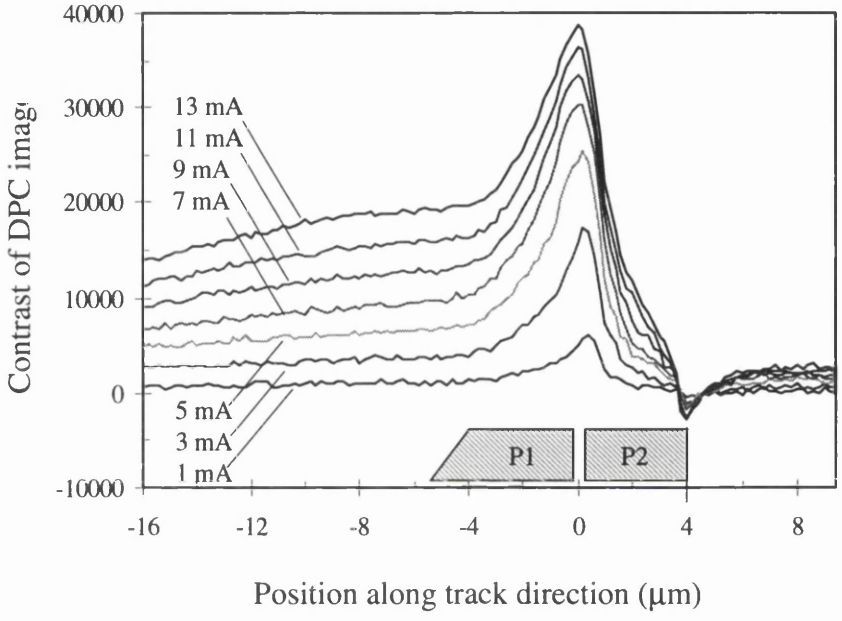

Fig. 5.13. Line traces of Fig. 5.12.(a) at ~0.25 μm from and parallel to the poleface.

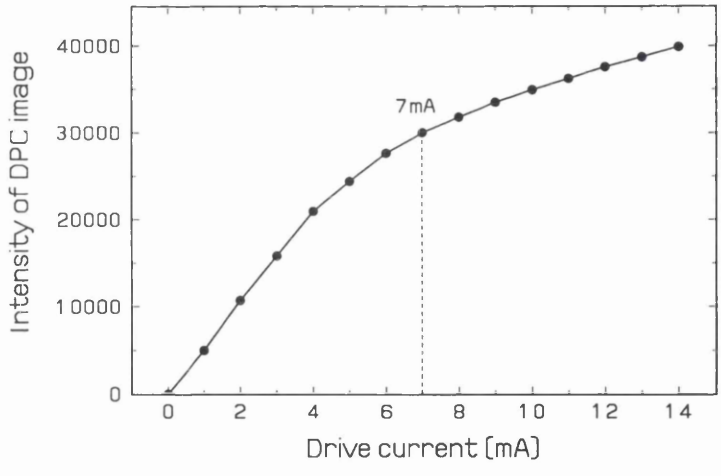

Fig. 5.14. The integrated field component B_x as a function of the dc driving current at the middle of the polegap in Fig. 5.12.(a), the dotted line indicates the onset of the saturation of the writing field.

5.5 Discussions and conclusions

The ART and RTM tomographic reconstruction methods have been applied to data from production thin film heads, collected using DPC Lorentz microscopy in a STEM instrument. The novel method of mounting the thin film head for data collection does mean that the stray field is reconstructed at a small angle of 5° to the ABS. However the simplification of collecting a full data set close to the ABS is considerable and should extend greatly the applicability of the technique. Since the writing characteristic is dominated by field along the head moving direction (x-axis) and we can do reconstruction including that data, the 5° tilt is of even less disadvantage. With the thin film head processed to remove partially the alumina in the vicinity of the poletips, the effect of stray flux escaping from regions away from the poletips has also been explored and these studies open up wider realms in microfield determination.

In the past there have been many electrical and magnetic methods for characterisation employed in recording head research, but none of them can provide direct information on the stray field and even the relationship with the micromagnetic structures. This is however possible by using combination of electron beam tomography of recording head fields and backscattered imaging of domain structure and domain wall dynamics in the same STEM instrument. Inasmuch as todays head-to-medium spacing are approaching 50 to 25 nm, it becomes very important to understand such local micromagnetic effects, as any of the finite element methods fail to do.

References

Arnoldussen, T. C., L. L. Nunnelley, F. J. Martin and R. P. Ferrier (1991), *J. Appl. Phys.* **69** (8), 4718-4720.

Ferrier, R. P., Y. Liu, J. L. Martin and T. C. Arnoldussen (1995), *J. Mag. Magn. Mater.*, **149**, 387-397.

Ferrier, R. P., S. McVitie and W. A. P. Nicholson (1990), *IEEE Trans. Magn.* **26**, 1337.

Grochowski, E. and D. A. Thompson (1994), *IEEE Trans. Magn.* **30**, 3797-3800.

Liu, Y. and R. P. Ferrier (1995), *IEEE Trans. Magn.* **31**, 3373-3375.

Mee, C. D. and E. D. Daniel (1987), *Magnetic Recording Vol. I: Technology*, Mcgraw-Hill.

Miura, Y. *et al.* (1980), *IEEE Trans. Magn.* **16**, 779.

Shakurai, Y. et al. (1994), *IEEE Trans. Magn.* **30**, 3894-3894.

Shinada, H. *et al.* (1992), *IEEE Trans. Magn.* **28**, 1017.

Steck, M., H. Schewe and E. Kubalek (1990), *IEEE Trans. Magn.* **26**, 1343.

Tsang, C. (1991), *J. Appl. Phys.* **69** (8), 5393-5398.

Tsang, C. *et al.* (1996), *IEEE Trans. Magn.* **32**, 7-12.

Yoshida, M. *et al.* (1993), *IEEE Trans. Magn.* **29**, 3837.

Zak, B. S. *et al.* (1996), *IEEE Trans. Magn.* **32**, 74.

Chapter 6

Investigations of the stray field from tape heads

6.1 Introduction

Storage capacity has increased dramatically in all applications of magnetic recording. This push for more capacity has been driven by several factors, including the increasing size of operating systems and applications as well as the falling price per Mbyte of data storage products, and has resulted in great demand for high density, high transfer rate tape recording systems for both data back-up and image storage.

High capacity is accomplished by increasing both the linear density and track density. To increase the linear density, high coercivity media, like metal particle or metal evaporated tapes, are needed. This, in turn, requires higher saturation magnetisation materials for the tape recording heads. The high data transfer rate demands fast relative head-to-tape speed coupled with high recording frequency, which put additional demands on the head material, both for reproduction as well as recording. To meet these requirements, the design of tape heads has developed in two different directions: the Metal-in-Gap (MIG) composite head and the laminated alloy film head.

In this chapter we present some of experimental results on MIG and laminated alloy film tape head fields. With its high sensitivity and resolution, the DPC technique can provide direct visualisation of the detailed stray field structure which other techniques fail to do.

It should be noted that the studies reported in this chapter on the MIG head were part of a collaboration with University of Regensburg, but only the work performed by the author is reported here.

6.2 The MIG write and ferrite read head fields

The main interests of this section focus on the spatial width and strength of the head fields, which define effectively the size of the magnetic information bit that can be written or read, and on the maximum achievable stray field before saturation of the ferrite material occurs.

6.2.1 The specimens and specimen preparation

The Metal-in-Gap (MIG) configuration of a ferrite tape head was introduced [Jeffers *et al.*, 1982] to achieve a more highly concentrated writing field and enable a ferrite head to write information on a high-coercivity media and produce higher linear density. With the advent of high-magnetisation and high-coercivity media, MIG heads have received interest by both rigid disk and tape industries. In disk applications, a low inductance structure MIG nano composite slider of single crystal Mn-Zn ferrite with 5.5 μm track width and 0.25 μm gap length for 1800 Oe (H_c) media has been reported [Goto *et al.*, 1994]. The performance of this head should lead to 250 Mb/in^2 recording.

Eventually the combined requirements of wider bandwidth and higher recording density limit recording performance for 'all-in-one-place' tape head designs. Consequently, there is a trend toward using separate heads for write and read functions, especially in stationary-head applications, such as tape drives, where the total mass and the electrical connections are less important than in moving-head applications. To achieve better read/write performance separate heads can be designed either for optimum reading or for optimum writing. Improved performance over inductive designs for reading are now possible by using magnetoresistive or Hall effect transducers.

The earlier recording heads were made from laminated magnetic alloys. Three of the most outstanding examples are molybdenum Permalloy (4 wt % Mo, 17 wt % Fe-Ni), Alfenol (16 wt % Al-Fe) and Sendust (5.4 wt % Al, 9.6 wt % Si-Fe) [Chin and Wernick, 1980]. All these three materials have high initial permeabilities at low

frequencies and high saturation magnetization as well as low coercivities. Permalloy has been used successfully in thin film disk heads. The principal advantages of Sendust are its high saturation magnetization and physical hardness. These lead to good writing performance and head wearability. But like other magnetic alloys, Sendust has a low resistivity and will be subject to losses of permeability due to eddy currents even at moderate frequencies, unless the head is made in a laminated structure or in thin film form.

The resistivities of ferrite materials are at least three orders higher than that of most metallic magnetic materials, hence the eddy currents and the associated permeability losses are relatively small. Similarly, ferrite materials have extremely good wearabilities with their Vickers hardness even higher than those of metallic alloys. Given these advantages, ferrite materials have dominated the field of high frequency applications, such as video heads, for the last 20 years. On the other hand, the theoretical upper limit in saturation magnetisation of ferrite materials is 0.6 T (6 kGs), which is significantly lower than that of magnetic alloys, such as Sendust which has a saturation magnetization of 1.0 T (10 kGs). This indicates a limitation in the use of ferrite materials with the trend toward higher areal density and shorter recording wavelength. But this limitation has been largely mitigated through the use of magnetic alloy pole tips, either on the head-tape surface or deposited on the pole-gap faces; the latter (Metal-in-Gap) has better mechanical stability and wearability.

Since the magnetic circuit of the MIG head has interfaces near the recording gap, it is very important to ensure a good magnetic contact between the metal pole tip and the ferrite core. Otherwise, undesirable secondary pole effects occur if the additional stray fields are of comparable magnitude to that from the primary gap [Ruigrok, 1984].

A pair of ferrite read and MIG write heads were used for a comparative study. The heads, based on ferrite material, had the same geometric structure as shown schematically in Fig. 6.1. Each of them consisted of a C-core and an I-core ferrite, which were glass bonded together to form a magnetic circuit with a finished gap length of 0.2 μm. The two heads have the same track width of 18 μm and 17 turns of thin wire for the writing and reading respectively. The azimuth angle φ for both heads is 20°. The difference between these two heads was in the gap configurations. The read head consisted of the ferrite material only, while the MIG write head had a 7 μm thick high

permeability and high saturation magnetization Sendust film deposited on the gap faces of the ferrite head before gap spacer deposition. The MIG write head was desired to produce high gradient writing field and high saturation magnetomotive force.

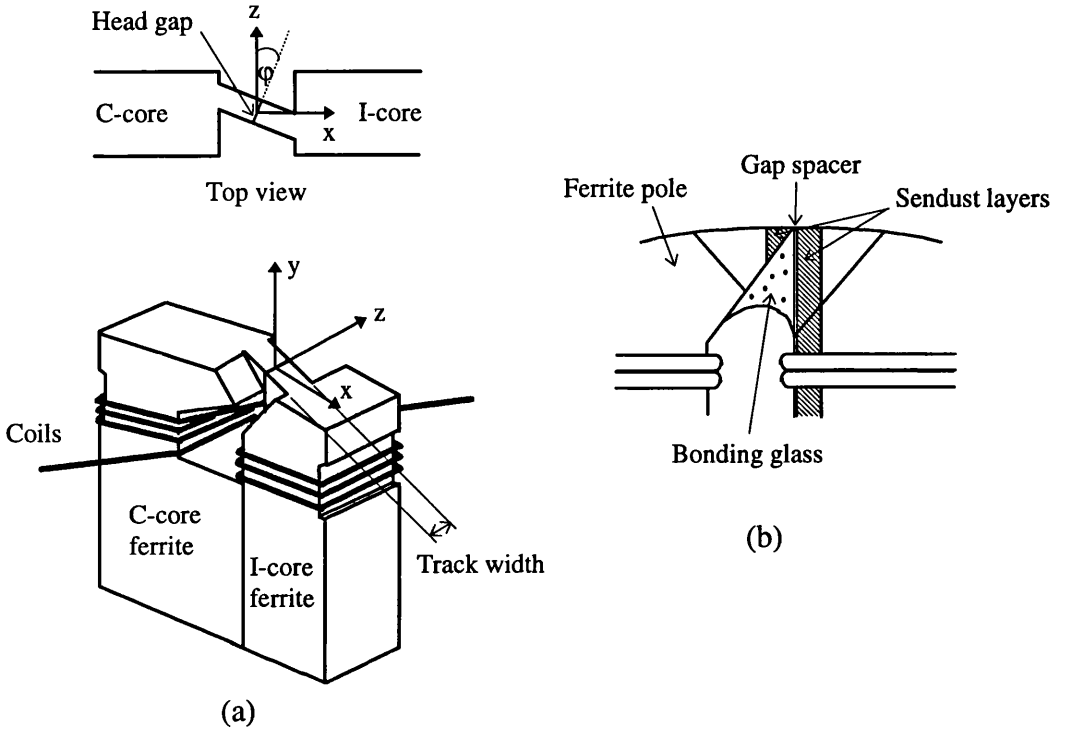

Fig. 6.1. *Schematic diagram of (a) the ferrite read and (b) the MIG write tape heads.*

Before using DPC Lorentz microscopy to study the tape head fields, the ferrite and the MIG heads have to be mounted on a specimen holder which is similar to the one used for the thin film head (c.f. Fig. 5.2). In the specimen holder the ferrite magnetic core, separated from its copper cantilever support, is mounted on a plane with the centre of the head gap coinciding with the axis of the specimen holder as shown in Fig. 6.2. This allows the electron beam to traverse parallel to the head-tape surface as the head is rotated about the axis of the specimen stub. Four flats are also milled on the stub parallel to its axis and at 90° to each other to locate the stub in a 'V' groove in the tomographic rod, and the required 180° rotation is thus achievable in conjunction with the use of the goniometer stage of the JEOL 2000FX. The two contact pads on the

mounting plane of the stub beside the ferrite core are used to make the connection to the head driving wires and reduce the risk of wire breakage.

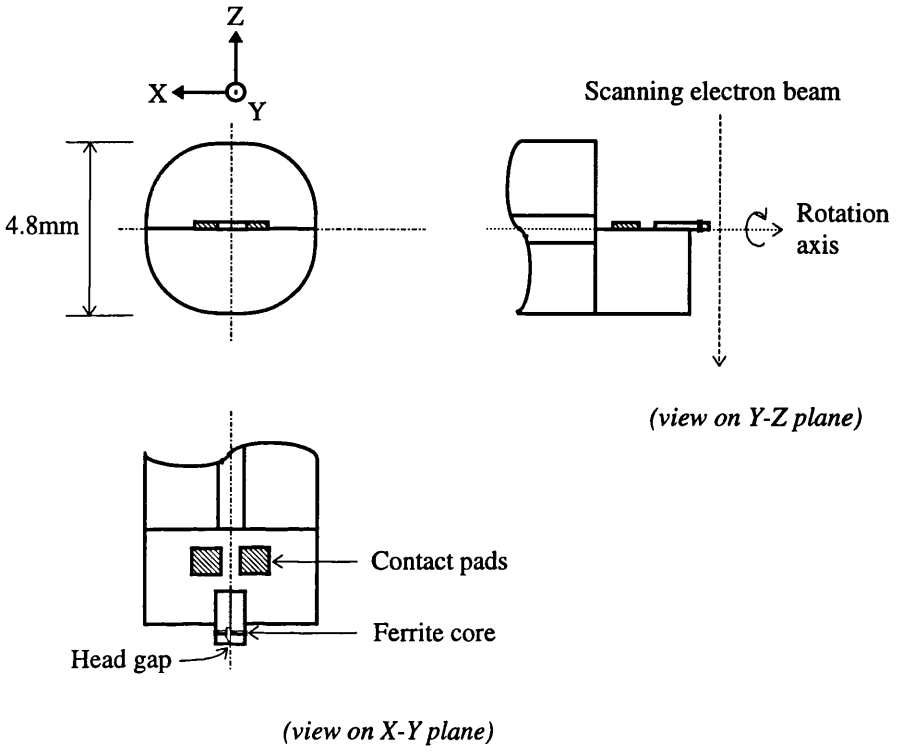

***Fig. 6.2.** Schematic diagram of the specimen stub for tape heads*

Since a ferrite material has very high resistivity, it must be coated with a thin layer of conductor to prevent electrostatic charging. This was done by sputtering the head and the mounting pill assembly with gold using a sputter coater. The head was coated twice from orthogonal directions to ensure that the whole surface was deposited with a layer of ~150 angstrom gold. Finally the head and the specimen stub assembly were mounted into position on the tomographic rod and the connections between the contact pads on the tomographic rod and the specimen stub were made. The top and the side views of the ferrite and the MIG heads before gold coating are shown in Fig. 6.3.

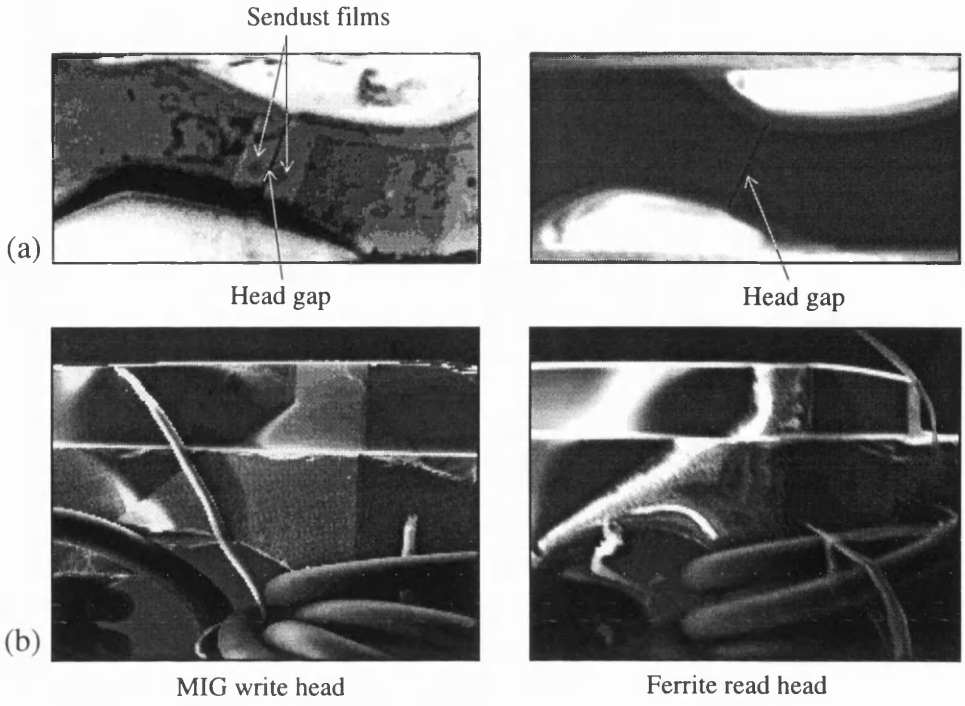

***Fig. 6.3**. The top (a) and the side (b) view of the MIG write and the ferrite read tape heads, before sputtering with gold layers.*

6.2.2 The field gradient and the half height of the field amplitude

In section 5.4 it was shown that useful information on the integrated stray field behaviour can be obtained from the DPC image in the polegap direction. It is even more reasonable to use this technique to study the tape head fields in this head orientation, since the gap length of the ferrite read and the MIG write heads as shown in Fig. 6.1 is only one ninetieth of the track width, and hence the stray field component along the head gap direction is much smaller than the field components in the plane perpendicular to the head gap. Therefore the major features of the integrated stray field can be revealed from the DPC images in the head orientation where the optic axis is parallel to the head gap.

By sputtering high permeability and high saturation magnetisation Sendust thin films onto the gap faces of the ferrite head, it is desired that the magnetic flux will be concentrated to the gap region and thus the MIG head can produce a writing field with a

higher gradient and amplitude. A comparison of the integrated stray fields from the MIG and the ferrite heads is shown in Fig. 6.4. The DPC images, taken under identical experimental conditions with a dc driving current of 10 mA, were recorded in the orientation that the electron beam was parallel to the head gap. The line scans below the images were taken at 3 pixels away and parallel to the head-tape surface, which was typically ~0.375 (0.125/pixel) μm from the surface if any misalignment of the head was ignored. The directions of the field components mapped are indicated by the arrows in the images. It can be seen from the line scans that the MIG head produces a writing field about 30~40 % higher and 30~40 % narrower than the normal ferrite head. The full width at half amplitude (FWHA) are about 2.6 μm and 3.8 μm for the MIG and the ferrite heads respectively (Fig.6.4 (a)). From the field component, which is normal to the head surface (Fig.6.4 (b)), it also can be seen that the magnetic flux is gathered to the gap region by the Sendust films, while the magnetic flux from the ferrite head is more widely dispersed.

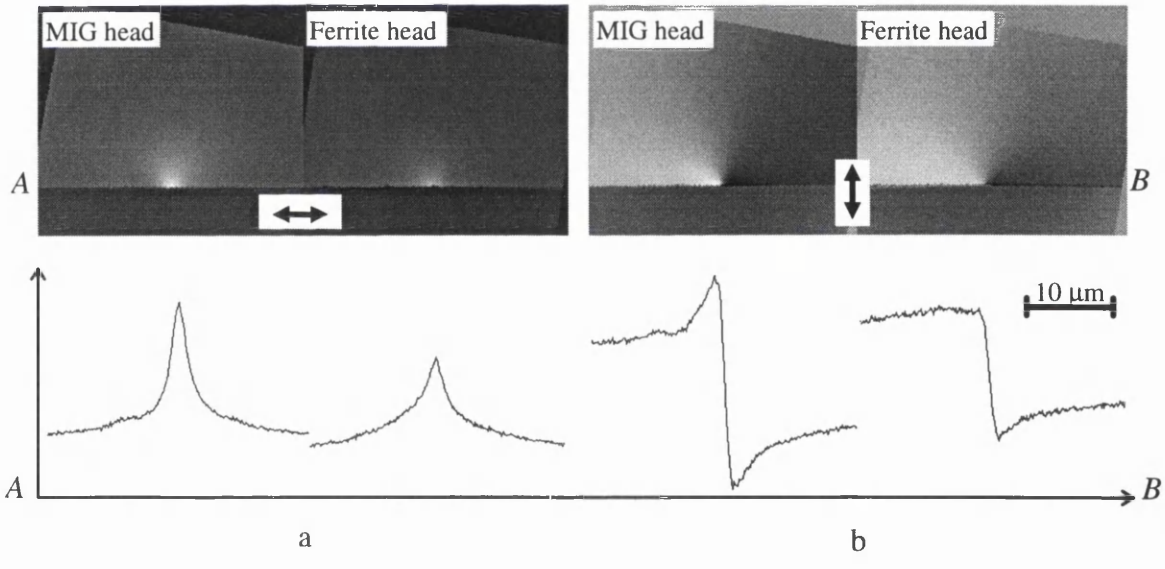

Fig. 6.4. *Comparison of the integrated stray fields from the MIG and the ferrite tape heads. The DPC images were taken under identical conditions with a dc driving current of 10 mA, the directions of the components of the fields mapped are indicated by the arrows. The line scans were taken at 3 pixels away from and parallel to the head-tape surface, a distance typically ~0.375μm.*

Because of a major experimental difficulty which will be discussed in section 6.3.2, a three dimensional field reconstruction was performed only for the ferrite tape head. Line traces of the writing field component and the field component normal to the head-tape surface are shown in Fig. 6.5. These line traces were extracted from the centre of and normal to the head gap, and revealed very similar field profiles to the integrated stray fields as shown in Fig. 6.4. From Fig. 6.5, The actual FWHA for the writing field component was measured to be ~2.7 μm, which was as expected. As the head gap dimensions of the MIG write and the ferrite read heads are basically the same, the comparison study shown in Fig. 6.4 is valid, especially when a full 3-D reconstruction is difficult to achieve.

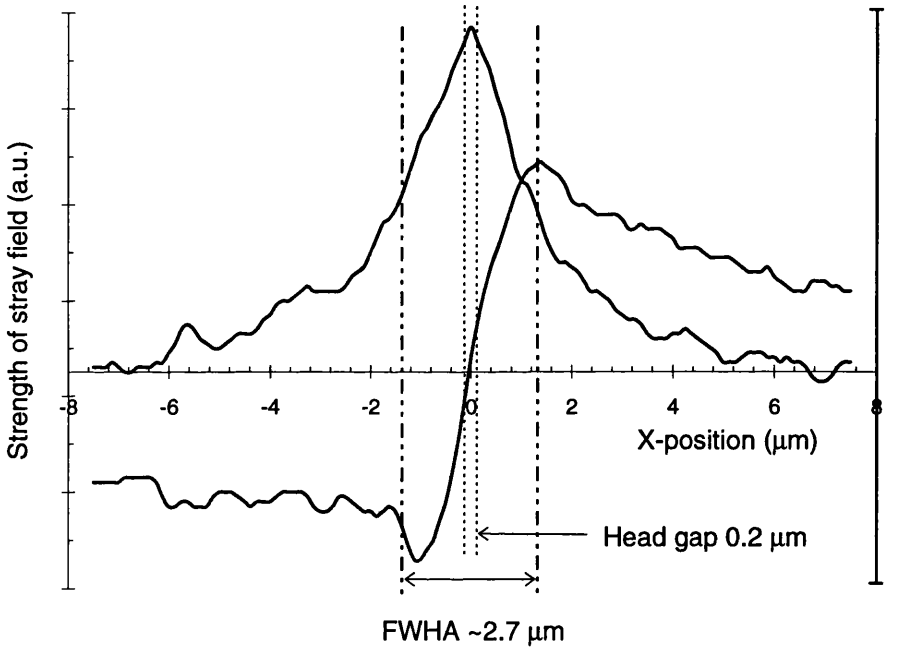

Fig. 6.5. *Line traces of the three-dimensional reconstructed field of the ferrite head extracted from the centre of the head gap and at ~0.375μm from the head surface. The driving current was 10 mA. The gap length and the FWHA of the writing field component are indicated.*

6.2.3 The secondary gap of the MIG head

As the dc driving current for the MIG head was increased to 15 mA, an additional magnetic flux leakage was observed beside the primary gap. After a driving current of 30 mA, a second flux leakage appeared on the other side of the primary gap. The evolution of these additional stray fields and their driving current dependence are shown in Fig. 6.6 and Fig. 6.7. A schematic diagram of the corresponding head geometry is also displayed at the bottom corner of Fig. 6.6. The locations of these additional stray fields were consistent with the extents of the Sendust layers in the MIG head. Therefore these stray fields did escape from the interfaces between the Sendust film and the ferrite substrate material. The effect of such secondary gaps may be explained due to the imperfect coupling between the two soft magnetic materials [Ruigrok, 1984].

A TEM investigation was carried out by colleagues in Regensburg [Petri *et al.*, 1996] to investigate structural reasons for the undesirable secondary gap effects. Two head materials with and without a functional layer at the interface were prepared for this purpose; the nature of this layer has not been revealed to us. The cross-sectional TEM images of the interface between the ferrite substrate and the Sendust thin film showed a clear difference in lattice strain. There was a broad region of strain contrast at the interface between the Sendust coating and the ferrite material when no functional layer was present. However, this strained region was dramatically reduced by inclusion of a functional interface layer. The strain concentration degraded the magnetic performance and therefore produced a high magnetic resistance region which introduced an additional gap. The existence of this kind of additional stray fields may lead to background noise and result in poor frequency response.

It is theoretically impossible to obtain perfect coupling between two magnetic materials and the effect of secondary gap will remain to a greater or lesser extent. However, the secondary gaps of the MIG head clearly have been reduced by the insertion of functional layers and improved frequency response of the MIG head has been achieved [Petri *et al.*, 1996]. With these functional layers, the effect of the additional stray fields is no longer detectable via electrical characterisation, but the remaining effect of the secondary gaps is still visible by using the DPC mode of Lorentz microscopy; this illustrates the high sensitivity and resolution of the DPC technique.

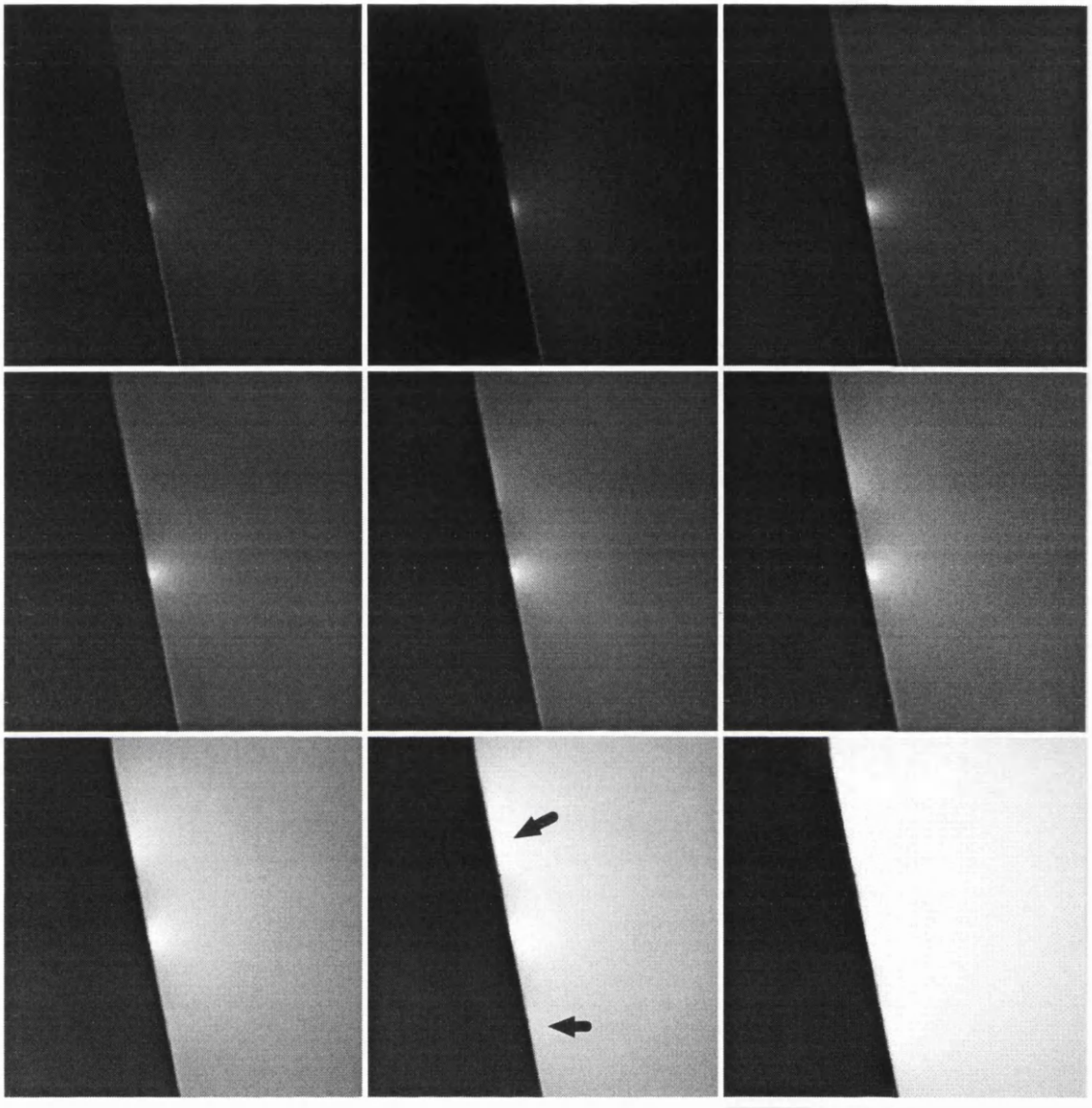

5mA	10mA	15mA
20mA	25mA	30mA
40mA	50mA	70mA

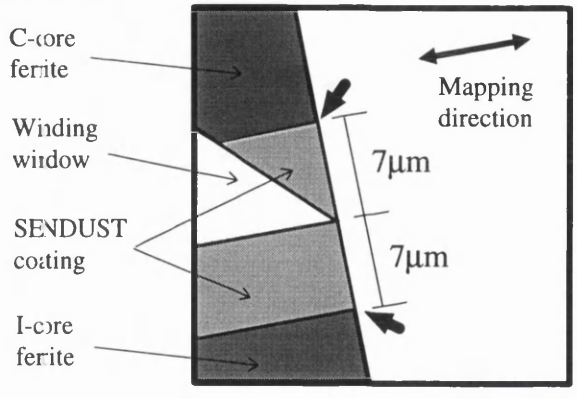

Fig. 6.6. *DPC images of the integrated writing field of the MIG write head for different driving currents. The development of the stray fields escaping from the secondary gaps indicated by the black arrows is coincident with the Sendust/ferrite boundaries.*

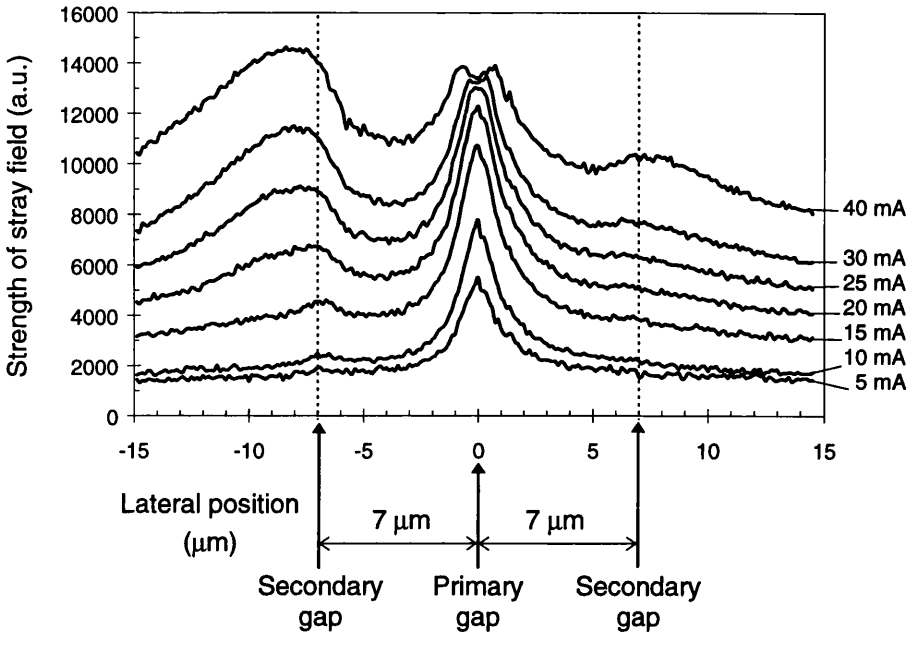

Fig. 6.7. *DPC line scans, taken parallel and at ~0.375 μm from the MIG head surface for different driving currents. For a driving current of 10 mA, only the primary gap can be observed. With the increase of the driving current, additional secondary gaps can be detected from their stray fields, the dotted lines indicate the Sendust/ferrite boundaries.*

6.2.4 The saturation behaviour of the MIG head

It has already been noted from Fig. 6.7 that the amplitude of the writing field tends to saturate with the increase of the head driving current. By recording the DPC signal, which is proportional to the stray field strength of the writing field component at the gap centre position for different driving currents, the saturation behaviour of the MIG write head can be studied. The driving current dependencies for both the primary gap and the first secondary gap (C-core side) are shown in Fig. 6.8. The writing component of the stray field from the primary gap initially strengthens fairly linearly with the increase of the driving current. However, at currents ≥10 mA the slope of the curve becomes smaller and tends gradually to a saturation of the ferrite material, which is reached for

values slightly above 30 mA. Further increase of the driving current leads to the stray field from the first secondary gap also saturating. Apart from the material factor, the geometric structure of the MIG head in the gap region also plays a role in the saturation behaviour. This can explain why the stray field from the first secondary gap (C-core side) increases much faster and saturates at a much lower current than that from the second secondary gap (I-core side) as shown in Fig. 6.7. Although the interfaces on both sides of the primary gap are essentially the same, the cross-sectional area of the magnetic circuit on the C-core side is much smaller, and this probably explains the early saturation of the ferrite material on the C-core side.

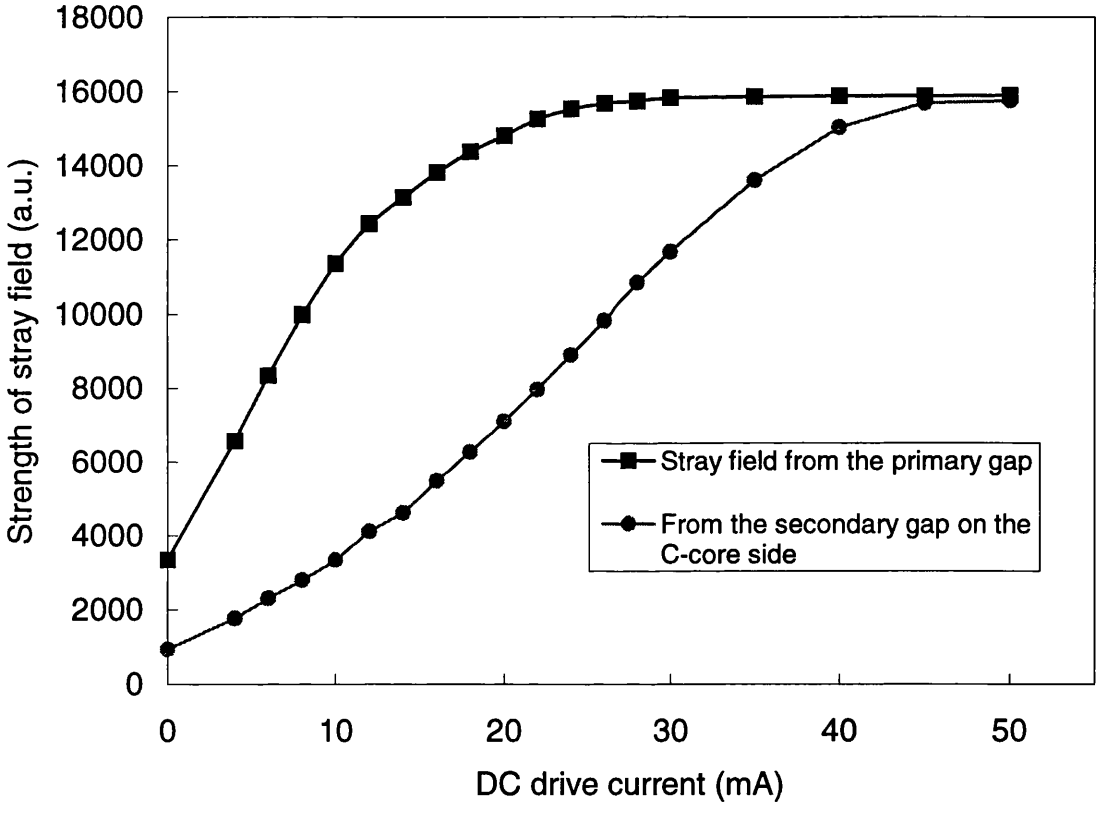

Fig. 6.8. *Saturation behaviour of the MIG write head, the stray fields from both the primary gap and the secondary gap on the C-core side are displayed.*

Attention is also drawn to the non-zero intensity of the stray field when no driving current is applied to the MIG head as shown in Fig. 6.8. This may indicate that the materials used to construct the MIG head are not 'soft' enough and therefore

noticeable magnetic remanence arises. Similar remanent effects have also been observed from the laminated alloy film tape head which will be discussed in section 6.3.3.

6.3 The laminated alloy film tape heads

Although the main interest for laminated tape head fields is the high frequency response, currently we can only study the dc characteristics due to the present implementation of DPC Lorentz microscopy. The three-dimensional reconstruction of the head fields excited by a dc driving current and the observation of the remanent fields from the laminated tape heads are presented in this section.

6.3.1 The specimens and the specimen preparation

The improved recording performance on high coercivity media using MIG heads has been obtained through the higher gradient and amplitude of the writing fields. However, because of the ferrite substrate, MIG heads suffer from the same limited frequency response as conventional ferrite heads (<10 MHz). Layered metal and thin film tape heads, on the other hand, use high saturation magnetisation materials and can work well at high frequencies.

In a laminated film tape head, the magnetic core is sandwiched between non-magnetic substrates. The thin film magnetic cores are made from alloys such as FeSiAl, FeTaN, CoZrNb, FeNbSiN or amorphous materials. These materials have higher electrical resistivities and better wear resistance than permalloy. The layered thin magnetic films lie along the recording direction and therefore the eddy current effects are minimised. These give rise to excellent high frequency performance. Advances in composite alloy materials have made laminated film tape heads write well at 150 MHz [Ash *et al.*, 1990], and have been of especial interest for use in high definition television (HDTV) recorders.

The DPC experiments described in this section are based on two laminated tape heads supplied to us by Philips Research Laboratories in Eindhoven and shown schematically in Fig. 6.9. The two tape heads are made from different magnetic alloys and are of different structures. The head gap regions of these two heads on the head-tape surface are displayed in Fig. 6.10. The head R374 was made from CoZrNb alloy with a four-layer magnetic core structure and an azimuth of 20°, while the head R416 had an eight-layer structure with no azimuth. It can be seen from Fig. 6.10 that both heads, especially R416, have notable displacements of magnetic cores across the head gaps.

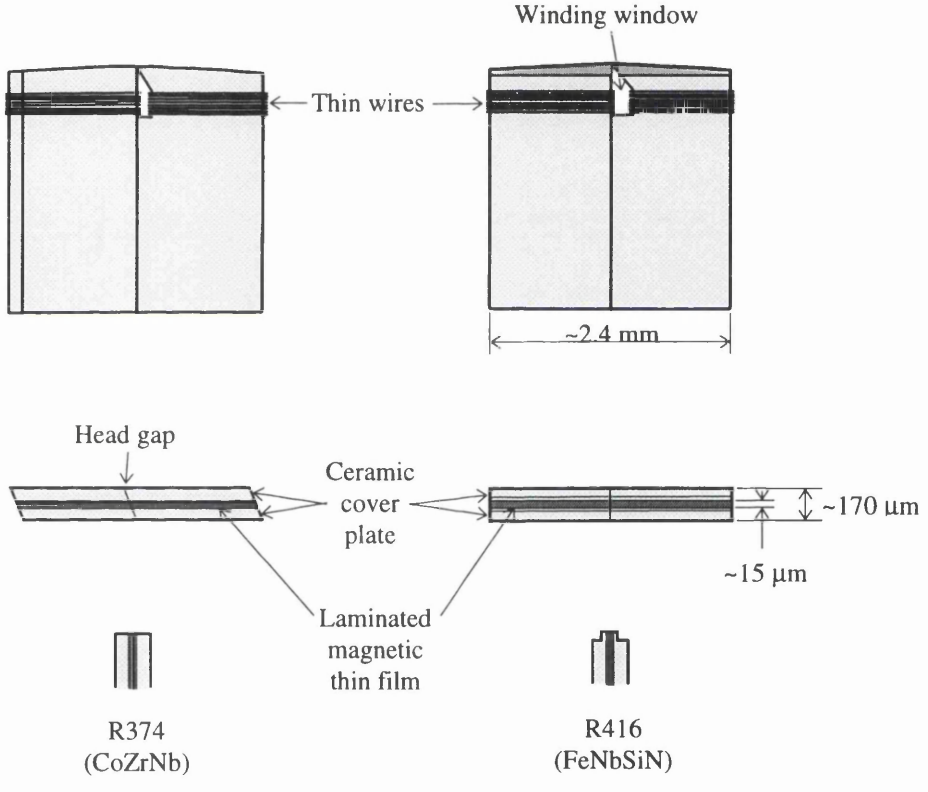

***Fig. 6.9**. Schematic diagrams of the laminated alloy film tape heads (not in scale).*

The shape of the laminated film tape heads is similar to the MIG write and the ferrite read tape heads, therefore the specimen mounting technique and the pre-experimental sample preparation are essentially the same as described in section 6.2.1.

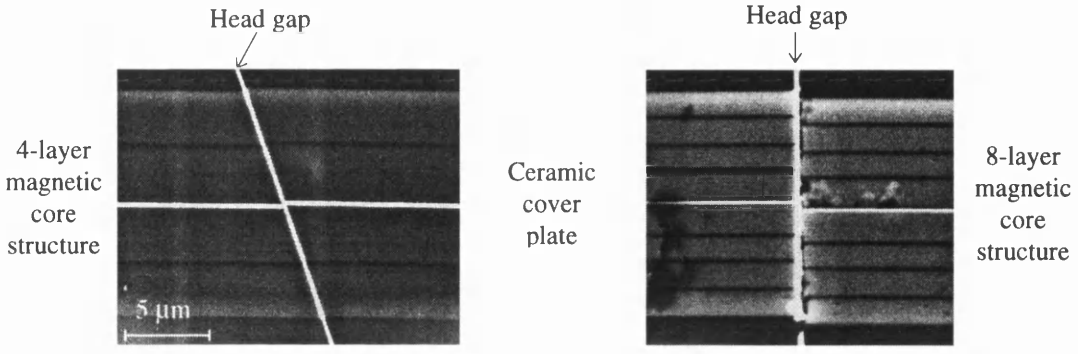

(a) Head R374 (CoZrNb) (b) Head R416 (FeNbSiN)

***Fig. 6.10**. SEM images of the head gap region of the laminated alloy film tape heads on the head-tape plane.*

6.3.2 3D reconstruction of the stray fields

During the DPC experiments to obtain full data sets for tomographic reconstruction, there were three experimental difficulties encountered for tape heads. First of all, the tape heads shown in Fig. 6.1 and Fig. 6.9 have head-tape surfaces which are much longer in one dimension than the other. This makes the adjustment of the eucentric height extremely difficult as there is no reference available to indicate the centre of the head gap. The eucentric height must be adjusted to achieve acceptable precision of the specimen single tilt axis. Secondly, and for the same reason, it is also impossible to focus the electron beam exactly on the geometric centre of the head gap. The nearest reference to the head gap centre are the side edges of the tape head close to the gap, which is still about ~10 μm (for head R416 and the MIG head) or ~80 μm (for head R374) away from the centre of the head gap. Failing to focus the sample properly will cause a loss of image resolution. Finally, when the head is rotated to the direction that the electron beam traverses parallel to the laminate layers, i.e. close to the surface in contact with the tape, any small stray field distribution or electrical charging can introduce huge DPC contrast. It has been proved that this contrast has little effect on the

field distribution in the head region, but as it is integrated over a much longer stray field region the contrast is so high that in some cases it conceals totally the contrast from the head gap field. Thus the alignment of the line scan data sets based on visual inspection of the superimposed line traces, which has been described in section 3.4.3, became difficult.

A reasonable eucentric height adjustment can be made by further decreasing the image magnification to ~2000; at such a magnification the winding window and both corners of the tape heads are visible on the STEM viewing screen, and thus can be used as the references in two orthogonal directions. In this way a less accurate eucentric height can be achieved at a lower magnification. Next, by tilting the tape heads through a small angle from the orientation where the electron beam is perpendicular to the head track direction, we can note the focus currents for imaging two extreme corners and then take the average value of the objective lens current as the focus current for the centre of the head gap. As has been discussed in section 4.3.3, the ART tomographic program allows the stray field to be reconstructed with a smaller field rotation angle than 180°. Therefore ignoring the DPC signal along the head track direction will not involve major reconstruction error, especially when the field component of the tape heads along the head gap direction is expected to be very small. In fact as the DPC contrast in that head orientation is from a long region stray field distribution, it has little effect on the reconstructed stray field in the gap region.

Following the above mentioned procedures, full data sets for tomographic reconstruction of tape head fields have been obtained except for the MIG head. As has been discussed in section 3.4.3, we have to use the field profiles shown in the line scan series to align any small translational displacement of the single tilt axis. The first DPC experiment on the MIG head failed to produce such line scan series due to an unsuccessful initial adjustment of the sample position. We did not have a chance to redo the experiment before the sample was accidentally damaged.

The stray field components of the laminated alloy film tape heads R374 and R416 shown in Fig. 6.9, are presented in Fig. 6.11 and Fig. 6.12 respectively. The field reconstruction for both heads have been performed using the ART with and without considering the DPC signal along the head track direction and it is proved from these experimental results that the difference is unnoticeable. Both heads were driven by a dc

current of 10 mA. The fields were reconstructed on a plane ~0.5 μm above the head-tape surface. It can be seen from the 2D grey scale images in Fig. 6.11 and Fig. 6.12 that the head R374 has wider transitions for field components B_x and B_y; this is confirmed by the measurement of the actual FWHA as shown in Fig. 6.13. The line traces in Fig. 6.13 were taken along the centre line and perpendicular to the head gap of the reconstructed stray fields; and the FWHA for R374 and R416 are measured to be ~3.3 and ~2.5 μm respectively.

6.3.3 The remanence effects for the laminated tape heads

An interesting observation for the laminated alloy film heads during the DPC experiments was a magnetic remanence effect. It has been confirmed that the head R374 revealed obvious magnetic remanence as shown in Fig. 6.14, while the head R416 shows little effect of such a permanent magnetic field. This suggests that some magnetically hard defects exist in the magnetic cores of head R374 and the fluxes from these magnetised parts concentrate in the head gap region [Van Kesteren, 1995]. The undesirable magnetic remanence may bring about non-linear distortion while recording and retrieving.

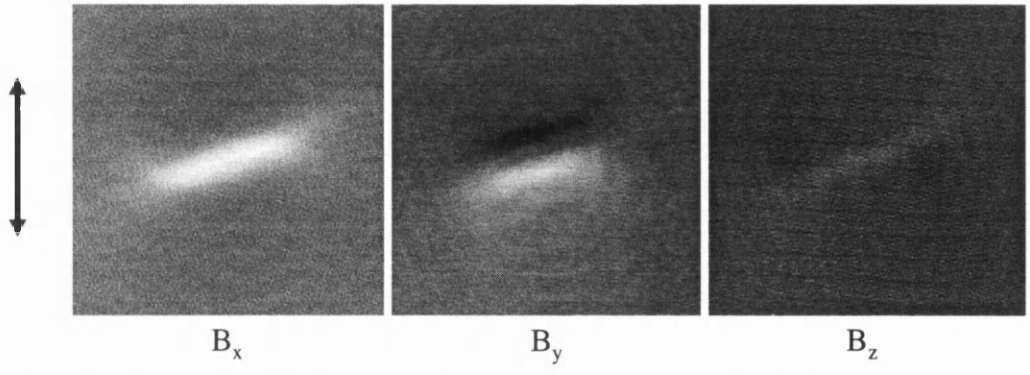

Fig. 6.11. *Reconstructed field components of the laminated alloy film tape head R374 (CoZrNb) by using the ART; the dc current was 10 mA and the track direction is indicated by the arrow.*

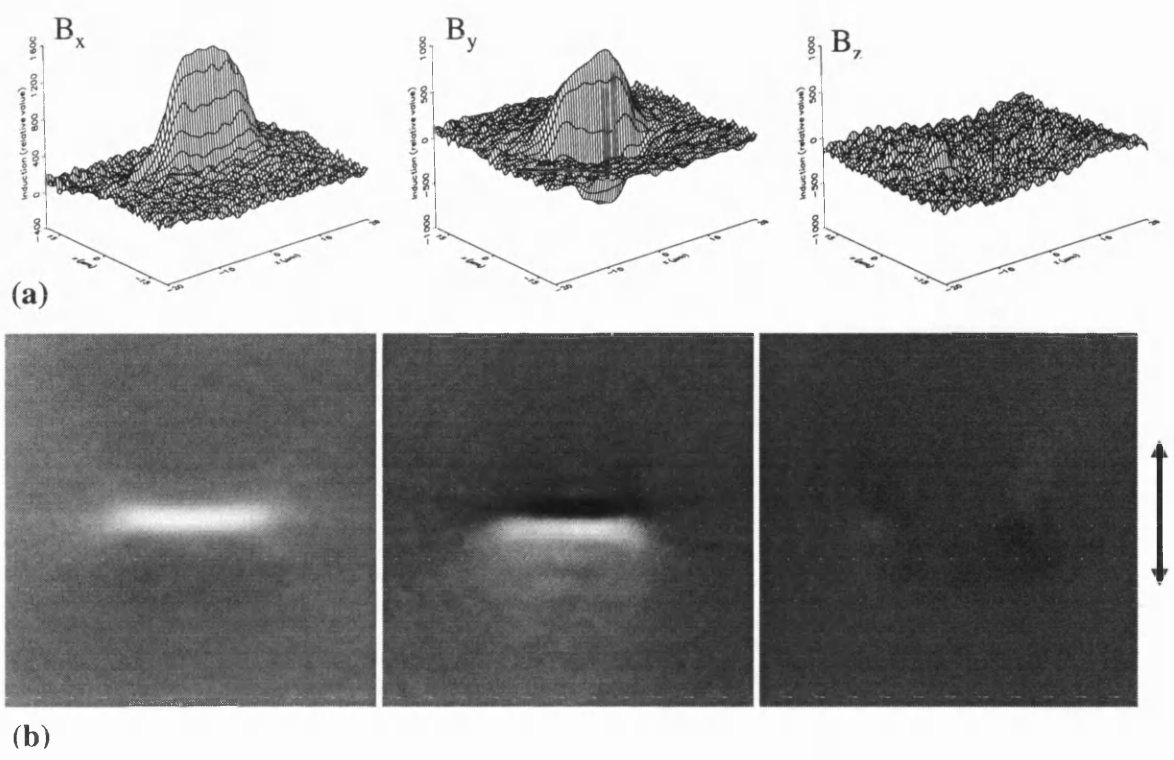

Fig. 6.12. *Reconstructed field values of the laminated head R416 (FeNbSiN) for a dc current of 10 mA using the ART, in the form of (a) 3-D surface plot, (b) 2-D grey-scale image; the track direction is indicated by the arrows.*

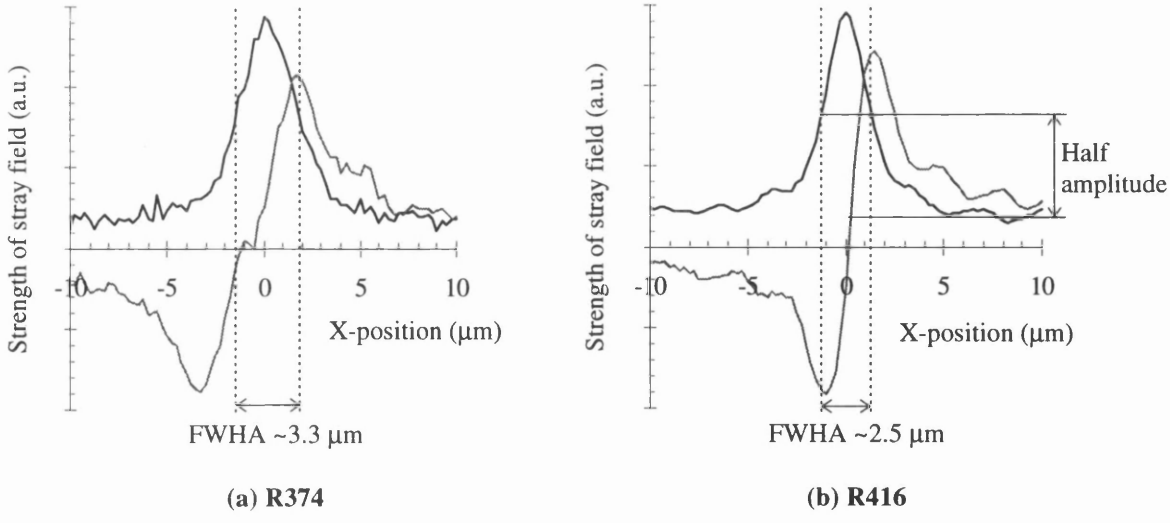

Fig. 6.13*. Line traces of the reconstructed stray fields of the heads R374 and R416 extracted from the centre of the head gaps. The FWHA for both heads are indicated.*

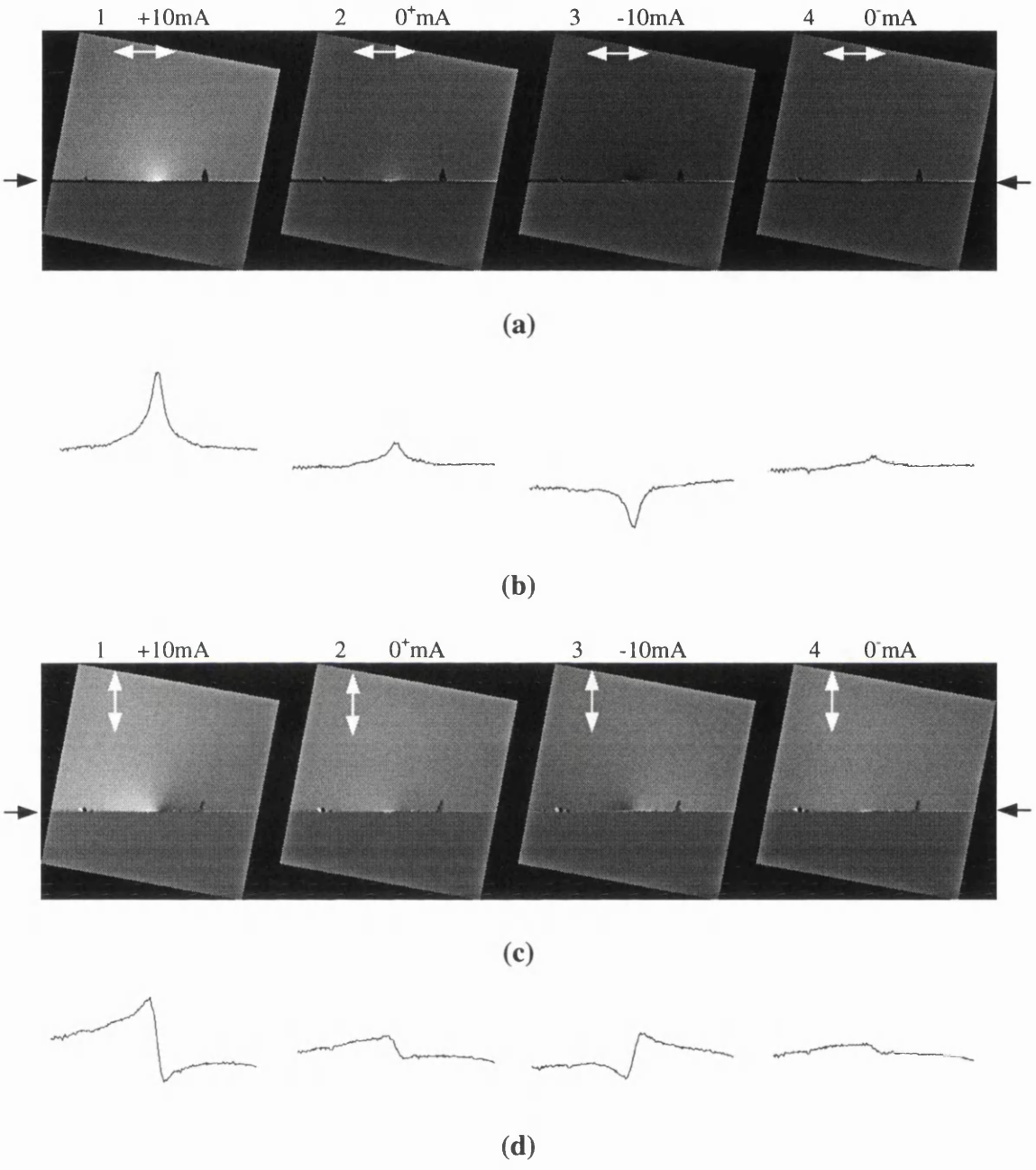

***Fig. 6.14**. a), c) DPC images of the stray field from the laminated tape head R374 with the contrast sensitive to the magnetic fields in the directions indicated by the arrows, b), d) the corresponding line scans of a) and c) across the marked positions indicated by the black arrows, the obvious discontinuity caused by the dust sitting on the head-tape surface of the head have been smoothed out from the line scans.*

6.4 Conclusions

From the experimental results presented in this chapter, it is clear that DPC Lorentz microscopy for imaging the stray field can provide valuable and quantitative information on the dc features of the stray field in the head gap region for different head designs. DPC Lorentz microscopy with its high sensitivity and resolution is especially useful in demonstrating stray field defects, such as the secondary gap effects and the presence of the magnetic remanence. Three dimensional reconstruction of the tape head fields from a tilting series of DPC images can provide quantitative information on the head gap field at the head-tape surface, from which the actual half amplitude field width can be obtained as a guide to evaluating the performance of different head designs.

References

Ash, K. P. *et al.* (1990), *IEEE Trans. Magn.* **26**, 2960-2965.

Chin, G. Y. and J. H. Wernick (1980), "Soft Magnetic Metallic Materials", *Ferromagnetic Materials*, North-Holland, Amsterdam, vol.2.

Goto, R. *et al.* (1994), *IEEE Trans. Magn.* **30**, 3909-3911.

Jeffers, F. J. *et al.* (1982), *IEEE Trans. Magn.* **18**, 1146-1148.

Petri, I., Y. Liu *et al.* (1996), *Submitted to IEEE Trans. Magn.*

Ruigrok, J. M. (1984), *IEEE Trans. Magn.* **29**, 872.

Van Kesteren, Hans (1995), *private conversation.*

Chapter 7

Calibration of DPC Lorentz microscopy for recording head field study

7.1 Introduction

DPC Lorentz microscopy has been successfully used to investigate recording head fields. The contrast of the DPC image provides information about the in-plane variation of the field component integrated along the electron beam trajectory; from such images the electron beam deflection data at different angular positions required for tomographic calculation can be extracted and many aspects of integrated stray field behaviour can be carried out. However, using a quadrant detector to acquire the DPC signal, the contrast behaviour is relative rather than absolute. For the study of the recording head field, it is highly desirable to have an absolute determination of the field distribution, since the write performance of a recording head is determined by the magnitude of the write field at the recording medium plane.

This chapter describes a technique to calibrate the reconstructed stray field from a thin film head. This is realised through the study of the response characteristic of the quadrant DPC detector (section 7.2) and the image contrast calibration during the DPC experiment (section 7.3). The thin film head field reconstructed with absolute values and further results analyses are presented in section 7.4.

7.2 Investigation of the response characteristic of the DPC detector

To calibrate the experimental data of the recording head field using the DPC mode of Lorentz microscopy, it is essential to study the response characteristic of the quadrant detector.

The annular quadrant DPC detector

The detector used in the DPC experiments described in this thesis is an annular quadrant position sensor made from photodiodes. A schematic diagram of the detector together with the definition of the detector parameters is shown in Fig. 7.1. The detector is located between the projector lens and the viewing screen in the column of the JEOL 2000FX STEM (c.f. Fig. 2.6). The DPC detector can be inserted into and removed from the electron optic axis with a cantilever handle outside the column to allow the DPC experiment and the normal (S)TEM operation. Details of the electronics set up for DPC signal processing and acquiring have been described in section 3.4.

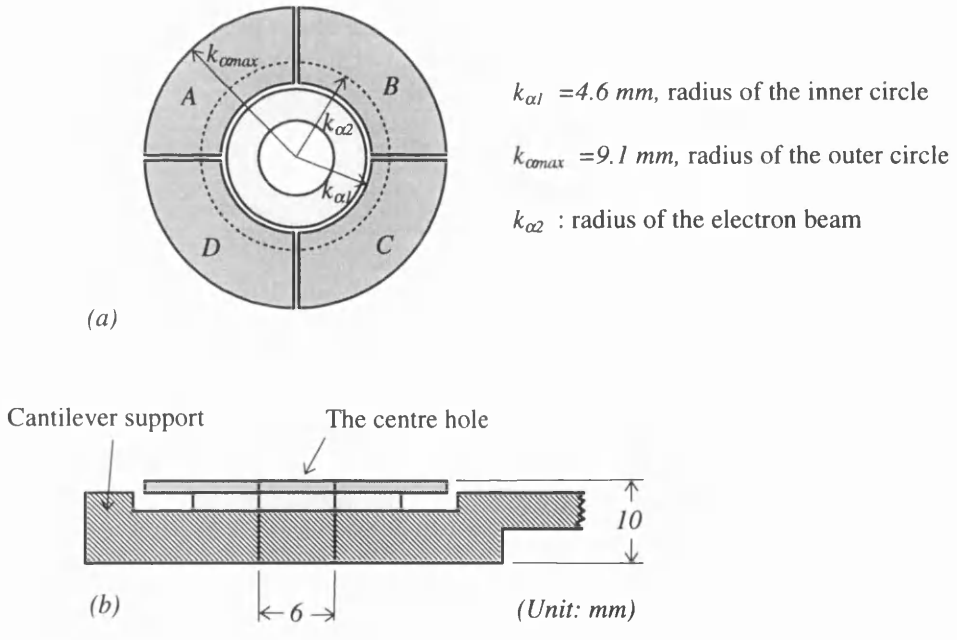

***Fig. 7.1**. Schematic diagram of the annular quadrant detector; (a) top view, the shaded part is the active detector area, (b) the cross sectional view.*

The signals from the four segments are displayed on the oscilloscopes. The zero point, non-field status, is achieved through the adjustment of the external image shift and scan amplitude control to obtain equal signals from the four segments in a full scanning cycle; this is known as the de-scan correction. The size of the electron beam on the detector plane is controlled by the free lens current unit and is set so that in a full scanning cycle the maximum deflection of the beam is restricted within the active detector area to avoid any signal discontinuity. When a magnetic field is present, the signal difference between opposite detector segments provides a direct measurement of the local deflection angle and hence the magnetic induction experienced by the electron beam for a given scanning position. Because of its geometry, the detector responds linearly to the magnetic induction only if the deflection of the electron beam is much smaller than the size of the beam, and this will be discussed quantitatively in the following.

One dimensional dc response of the detector

As we are dealing with the stray field in a free space, there is no need to consider the phase modification due to the specimen material and therefore a dc response is relevant in this case. We assume that the electron beam deflection only occurs in one orientation, e.g. (*A-C*), thus the one dimensional dc response of the annular quadrant detector can be calculated simply from the area difference of the electron probe on opposite segments. There are three possible electron beam deflection situations as shown in Fig. 7.2, which divides the response curve into three periodicities. It is convenient to use the detector parameter K ($K = k_{\alpha 1} / k_{\alpha 2}$) and the spatial frequency k_r ($k_r = k_x / k_{\alpha 2}$) to describe the detector geometry and the electron beam deflection.

In Fig. 7.2, we assume that the outer diameter of the active detector area $k_{\alpha max}$ (c.f. Fig. 7.1) is infinite, therefore the signal difference saturates only after the electron beam resides completely within one segment. From the planar geometry shown in Fig. 7.2, the one dimensional dc response of the annular quadrant DPC detector as a function of the spatial frequency k_r and the detector parameter K is calculated as (7.1) (c.f. Appendix) and shown in Fig. 7.3.

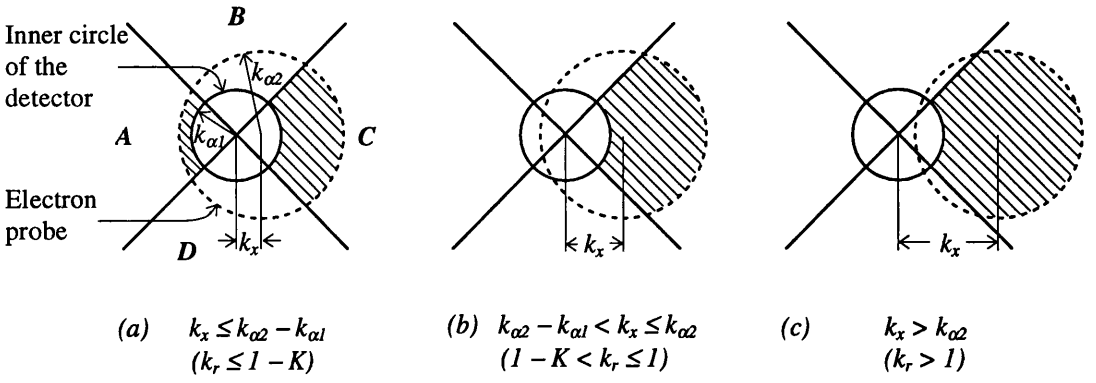

Fig. 7.2. *The electron intensity distributions in the plane of an annular quadrant detector of three different periodicities. The information carrying signals arise from the subtraction of the hatched areas on opposite segments.*

$$I(k_r) = k_{\alpha 2}^2 \left[\pi - 2\tan^{-1}\frac{\sqrt{2-k_r^2}}{k_r} + k_r\sqrt{2-k_r^2} \right] \qquad k_r \le 1-K$$

$$I(k_r) = k_{\alpha 2}^2 \left[\pi - 2\tan^{-1}\frac{\sqrt{2-k_r^2}}{k_r} + k_r\sqrt{2-k_r^2} - \frac{\pi}{4}\left(1+K^2\right) - \frac{k_r^2}{2} + \sin^{-1}\frac{k_r}{\sqrt{2}} + \frac{k_r}{\sqrt{2}}\cos\cdot\sin^{-1}\frac{k_r}{\sqrt{2}} \right]$$

$$1-K < k_r \le 1$$

$$I(k_r) = k_{\alpha 2}^2 \left[\pi - 2\tan^{-1}\frac{\sqrt{2-k_r^2}}{k_r} + k_r\sqrt{2-k_r^2} - \frac{\pi}{4}K^2 - \frac{k_r}{\sqrt{2}}\cos\cdot\sin^{-1}\frac{k_r}{\sqrt{2}} + \frac{k_r^2}{2} + \frac{3\pi}{4} - \sin^{-1}\frac{k_r}{\sqrt{2}} \right]$$

$$k_r > 1 \qquad (7.1)$$

As determined by the detector geometry, perfect linearity of the signal response is impossible. However when the electron beam deflection is very small compared with the size of the bright field cone, i.e. $k_r = k_x/k_{\alpha 2} << 1$ thus $I(k_r) \approx \sqrt{2}k_{\alpha 2}^2 \cdot k_r$, the signal

response becomes very close to a straight line as indicated graphically in Fig. 7.3 by the reference dash and dot line. The approximated linear region of the annular quadrant DPC detector is determined by the detector parameter K, which represents the size of the bright field cone for a given detector. As shown in Fig. 7.3, a smaller K, in other words a bigger bright field cone, provides a longer linear dynamic region of the signal response. On the other hand, as the random noise is proportional to the square of the signal level, a larger K gives rise a higher signal-to-noise ratio [Chapman *et al.*, 1990]. This is crucial for the study of a thin film magnetic sample, as the contrast cancellation between the magnetisation and the stray field decreases significantly the information carrying signals. Nevertheless, for recording head field studies, the objects of measurement are the stray fields in free space, therefore the signals are much stronger than that from a typical thin film sample and thus the signal-to-noise ration becomes a minor problem compared with the signal linearity.

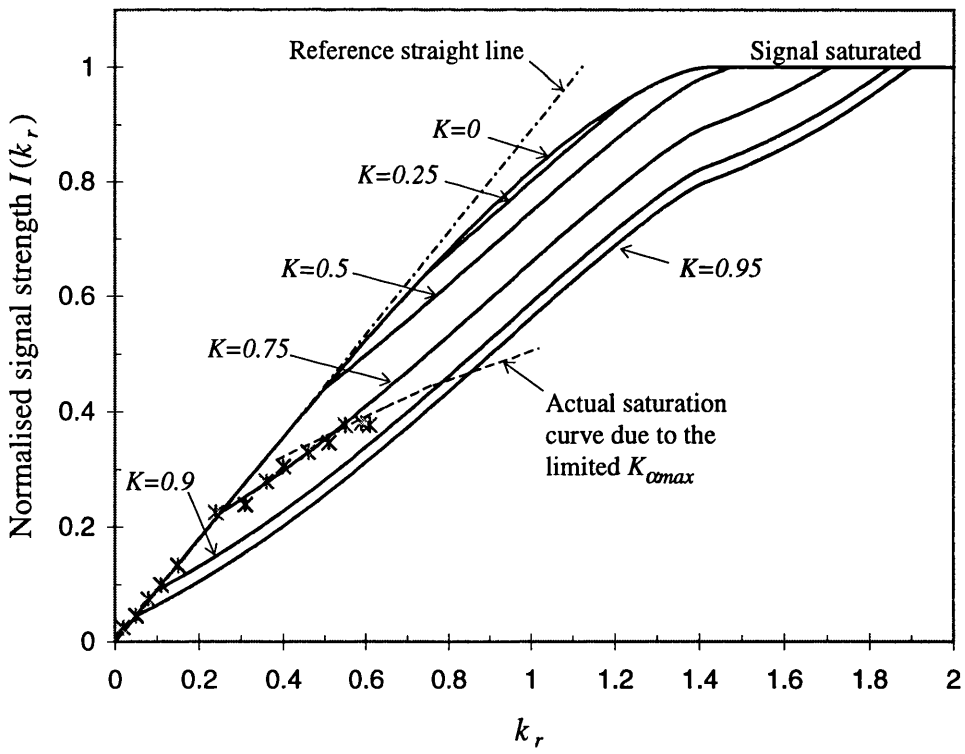

Fig. 7.3. *One dimensional dc response of the annular quadrant DPC detector for different values of detector parameter K as a function of the special frequency k_r; the star dots are normalised experimental data, which will be introduced in next section.*

From the above discussion, it seems that one solution to obtain a longer linear response is to use a bigger bright field cone, which is equivalent to an increase in the camera length L of the imaging system. This is true only if the outer radius of the detector k_{comax} is big enough compared with the bright field cone, otherwise the finite size of the detector will result in an earlier saturation of the DPC signal as the bright field cone is deflected to reach the outer edge of the detector. In practice, the annular quadrant detector has a outer radius of 9.1 mm, and this gives rise to a saturated signal which appears at a much smaller spatial frequency than that if we assume that the size of the detector is not limiting as shown in Fig. 7.3 by the dashed line. The possible parameter variations for the detector shown in Fig. 7.1 are listed in Table 7.1, which indicates that a detector parameter of $K \approx 0.7$ is a compromise choice as far as the linear dynamic region and the signal saturation are concerned.

Table 7.1

Detector parameter K	0.95	0.9	0.75	0.7	0.5	0.25	0
Radius of bright field cone $k_{\alpha 2}$	4.84	5.11	6.13	6.57	>9.1	>9.1	×
Approximated linear region	0.06	0.11	0.25	0.34	0.5	>0.5	>0.5
Actual saturation point	0.88	0.78	0.49	0.38	×	×	

So far all the discussions are based on the annular quadrant detector. However, as can be seen in Fig. 7.3 that a solid quadrant detector, which is equivalent to a detector parameter of $K=0$, has the widest dynamic response region ($k_r>0.5$) and therefore is the preferable detector for recording head field studies. The signal saturation point of a solid quadrant detector will depend on the size of the detector and of the bright field cone used and it is certainly possible to exceed the dynamic signal response region.

7.3 DPC experiments with contrast calibration

DPC experiments were carried out to acquire the input for tomographic calculation and to obtain the data set to calibrate the contrast of the image. The specimen used was an

IBM Tanba thin film head, which had been prepared following the procedures described in section 5.2. An ABS view of the poletip region of the head after partial removal of the alumina is shown in Fig. 7.4. The dimensions of the poletips were ~7×4 and ~9×4 μm for P1 and P2 respectively, and there were 36 turns of the head coil. The imaging conditions of the DPC experiment were the same as listed in Table 5.3 except for the condenser aperture and the head drive current. The head was driven by a dc current of 10 mA, which was about one-third of the maximum driving current allowed. The condenser aperture was 120 μm.

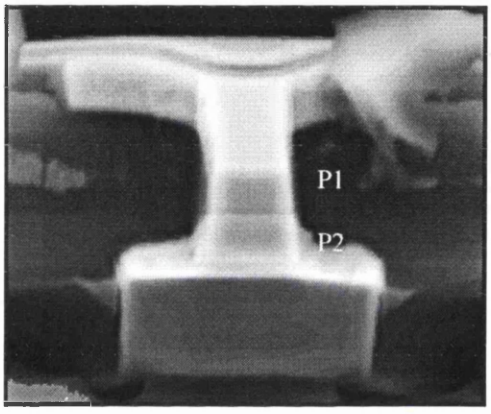

***Fig. 7.4**. SEM image of Tanba thin film head in the poletips region after partial removal of the alumina.*

The line scans extracted from the experimental DPC images at different angular positions are shown in Fig. 7.5, the measurement plane represented by these line scans is at 5° to the ABS and ~0.3 μm from the centre of the head gap. The intensity in Fig. 7.5 are still relative values.

To calibrate the contrast of the DPC image, one needs to find out the relation between the intensity and the corresponding electron beam deflection at a certain point in the image. So long as the DPC image is recorded digitally, the intensity of the image is known. By switching the scanning to 'spot mode' and removing the DPC detector away from the electron beam path, the actual electron beam deflection at a certain point can be recorded using the standard TEM camera under the viewing screen; the film is

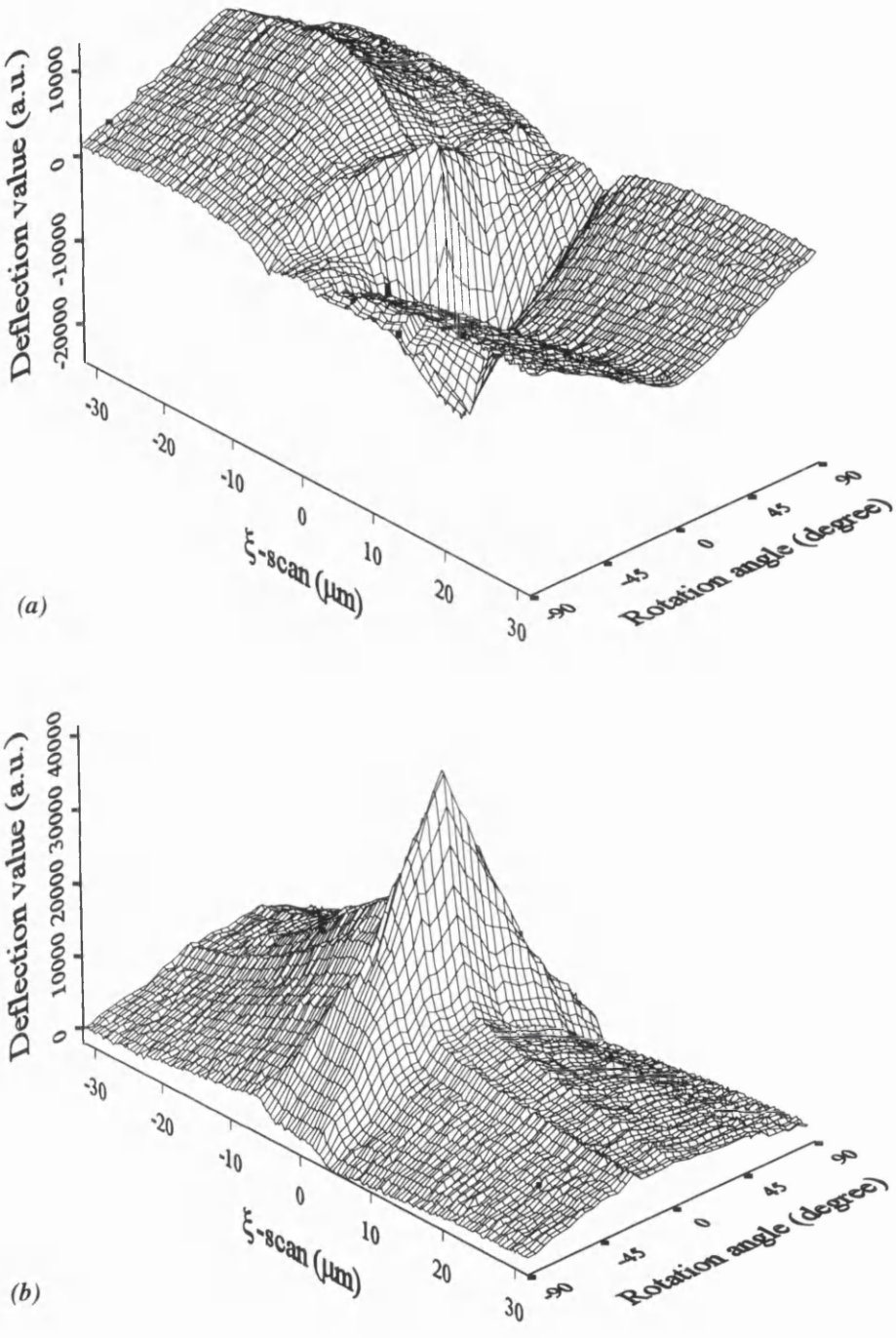

Fig. 7.5. *3D surface plots of the line scans taken at 5° to the ABS and ~0.3 μm to the gap centre of Tanba thin film head, (a) deflection in the measuring plane and (b) deflection normal to the measuring plane.*

exposed twice for two different head driving conditions, one with the required dc current and one without the driving current. The measurement of the displacement of the bright field cone on the double exposed film and the corresponding intensity in the DPC image provide one data point for contrast calibration. Repeating this procedure a series of data for different spatial frequencies can be obtained.

As the contrast of the DPC image is a function of the particular lens set up and digital image acquisition conditions, the calibration data have to be recorded in conjunction with the acquisition of the DPC images for magnetic field tomography. It is convenient to gather the calibration data for the head orientation where the electron beam is parallel to the head gap, since this gives the highest contrast and hence the highest signal-to-noise ratio. In addition, a wider selection of suitable data points can be obtained in this head orientation.

The Link system which we have used to acquire the digital DPC image can also perform x-ray analysis, and this means that accurate electron beam positioning is available in the spot scanning mode. In the calibration procedure, after a suitable DPC image of the stray field in the head gap direction was acquired with 256×256 resolution, the scanning beam was switched to spot mode and the Link system turned its x-ray analyses mode. A quarter of the acquired DPC image (128×128 pixels) was then picked up and re-displayed to 512×512 resolution as shown in Fig. 7.6, in this way the position accuracy of the beam was increased by four times. The electron beam was moved manually in the vicinity of the head gap to choose such a point where one pair of the subtraction signals, e.g. (*B-D*), was equal to zero, hence the detector response at that point only had one component. The beam was gradually moved away from the gap region to set the positions for different values of the one dimensional signal. After each of such positions was chosen, the DPC detector was removed from the beam path and the actual electron beam deflection was recorded by double exposing the film using the standard TEM camera of the JEOL 2000FX with the head excitation switched between a certain dc current and zero. These procedures were repeated until sufficient number of data points were obtained.

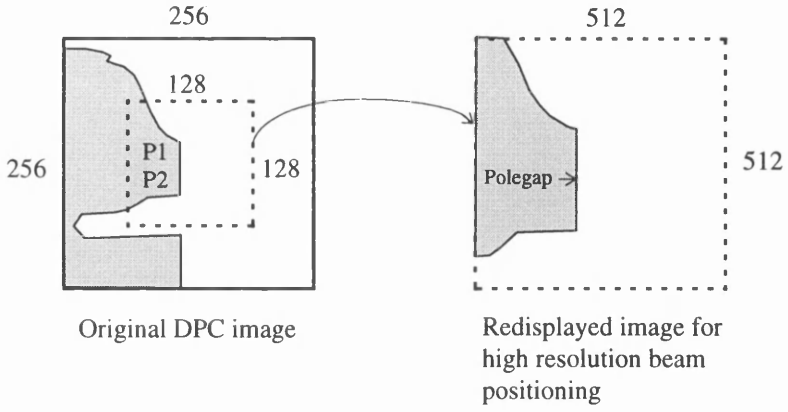

Fig. 7.6. *Schematic diagram showing the image conversion in beam positioning*

A set of experimental results from the Tanba thin film head for contrast calibration of the DPC image are presented in Fig. 7.3 as star dots. These data points have been normalised by fitting the data with small k_r with the reference straight line, since the linearity is guaranteed when the spatial frequency is small. It can be seen in Fig. 7.3 that the experimental data agrees very well with the theoretical curve of $K \sim 0.75$ and the signal saturates at $k_r \sim 0.54$. The highest point in this experimental data set was obtained under a head drive current of 60 mA, which is about six times higher than the current we normally used in the DPC experiments of thin film head fields and about two times higher than the point from which the linear region of the response curve ends. Therefore the signal linearity in previous DPC experiments is guaranteed.

The camera length for the set up of the DPC experiment is also needed to allow the absolute determination of the head field by tomographic calculation. The principle for calculating the camera length L is shown in Fig. 7.7. The probe semi angle α is a function of the condenser aperture (section 2.4.3) and can be measured precisely by means of an electron diffraction experiment using a suitable standard specimen. Thus the camera length can be calculated as: $L = R / \tan\alpha - l$, and therefore, $k_{\alpha 2} = L \times tan\alpha$. The L and $k_{\alpha 2}$ were calculated to be 6.17 m and 5.93 mm respectively in this calibration. The actual detector parameter was also obtained to be 0.776 and was consistent with the experimental curve shown in Fig. 7.3.

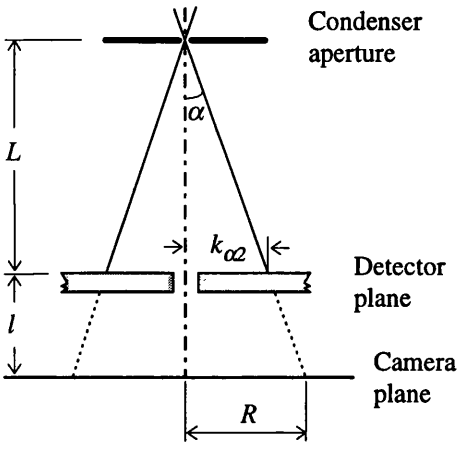

Fig. 7.7. Schematic diagram for determining the camera length L and the radius of the bright field cone on the detector plane $k_{\alpha 2}$.

7.4 Analysis of results and conclusions

Through the calibration procedures described in section 7.3, the electron beam deflection values and the camera length of the imaging system are known. Hence the fundamental equations of ART tomographic calculation (3.34)~(3.36) are now provided with the absolute values of the input data. Thus the iteration result will now produce the absolute 3D determination of the recording head field. The reconstruction results of the DPC experiment on the Tanba thin film head field discussed in section 7.3 are presented in Fig. 7.8. The field components are shown in 3D surface plot format together with their centre line traces. As introduced in section 5.4, the reconstructed field distribution is on a plane at 5° to the ABS and ~0.3 μm from the centre of the head gap.

It has been confirmed in section 7.3 that the electron beam deflections in the DPC experiments for thin film head field studies were within the linear area of the detector response. Thus the calibration of the experimental DPC image has been done simply by scaling the contrast with a constant, and this has nothing to do with the field profiles. Therefore all the discussions in chapter 4 about the field reconstruction

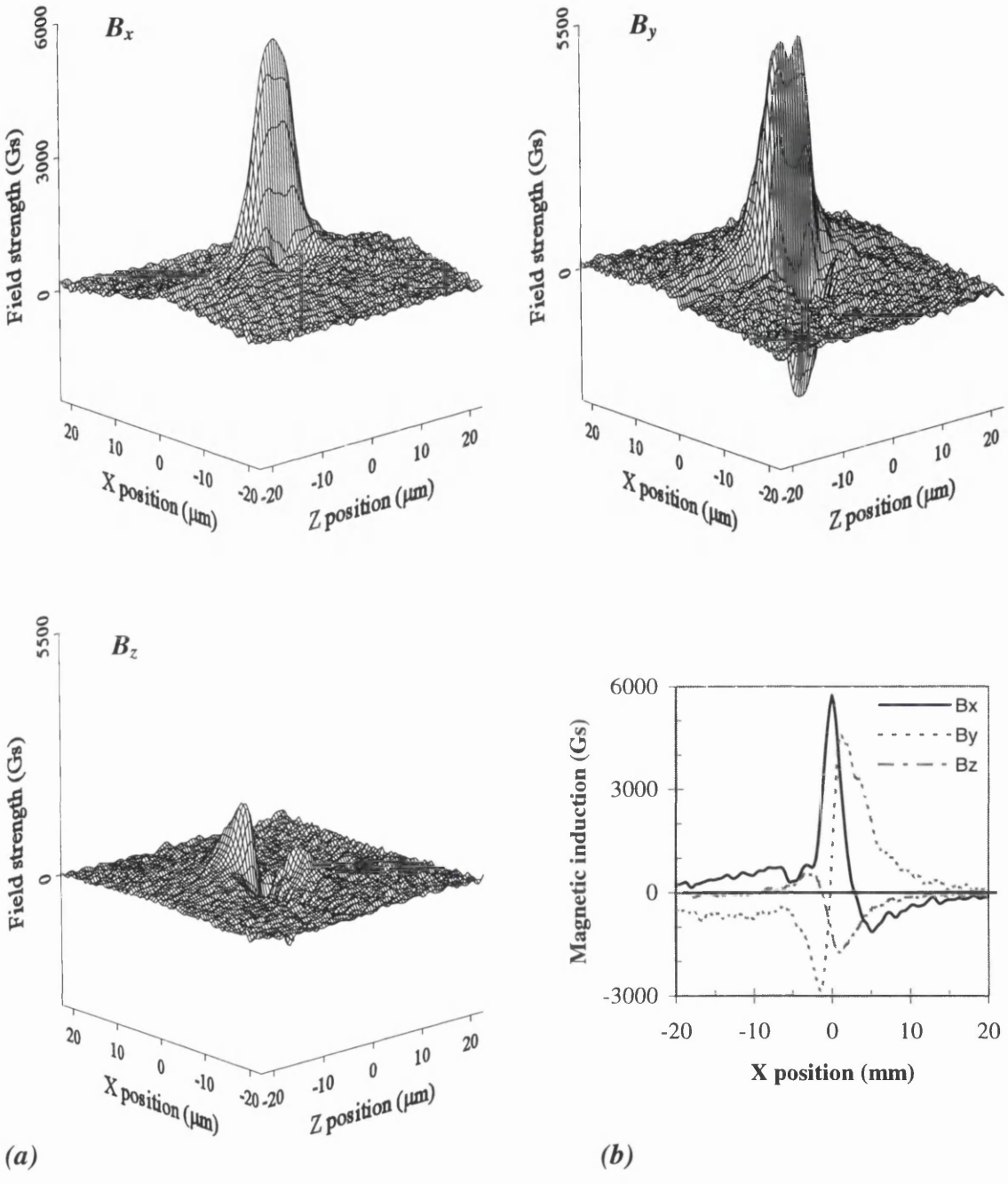

Fig. 7.8. *Reconstructed field values of the Tanba thin film head from the input data shown in Fig. 7.5, (a) in 3D surface plot format, (b) line traces of the field components taken from the centre of the poletips except for B_z which is taken from the edge of the poletips. The head is driven by a dc current of 10 mA.*

accuracy based on relative values still hold. For a field distribution with such a gradient/magnitude as shown in Fig. 7.8, both the ART and RTM tomography programs can provide reconstruction with high accuracy of <10%. Whilst the calibration error is determined by the experimental technique, the major factors are the drifting of the DPC signal and the beam location accuracy. So far it is not possible to determine directly the calibration accuracy, but the fact that the experimental data set used for the calibration are in good agreement with the theoretical analysis, as shown in Fig. 7.3, can at least in part verify the validation of the calibration.

The Tanba thin film head field was also reconstructed using the RTM. The comparison of the reconstructed results from the ART and RTM in the form of 2D grey scale image is shown in Fig. 7.9 and reveals very close agreement for the field distribution apart from the existence of more noise from the RTM results. The agreement of the RTM reconstructions from different components of electron beam deflection confirms the consistency of the two independently acquired input data sets, which in turn verifies the validity of the ART result, since the ART reconstruction is based on both electron beam deflection components. The centre line traces of the reconstructed field components from the ART and RTM are displayed in Fig. 7.10, which again reveals very good agreement in the field profiles. The field reconstruction from the ART is purely the result of algebraic synthesis from both components of the electron beam deflection data, while that from the RTM is the deconvolution of the Fourier transform of the universal magnetic field equations. The fact that both results from totally different reconstruction algorithms are consistent provides justification for the reliability of the experimental data as well as the reconstruction result.

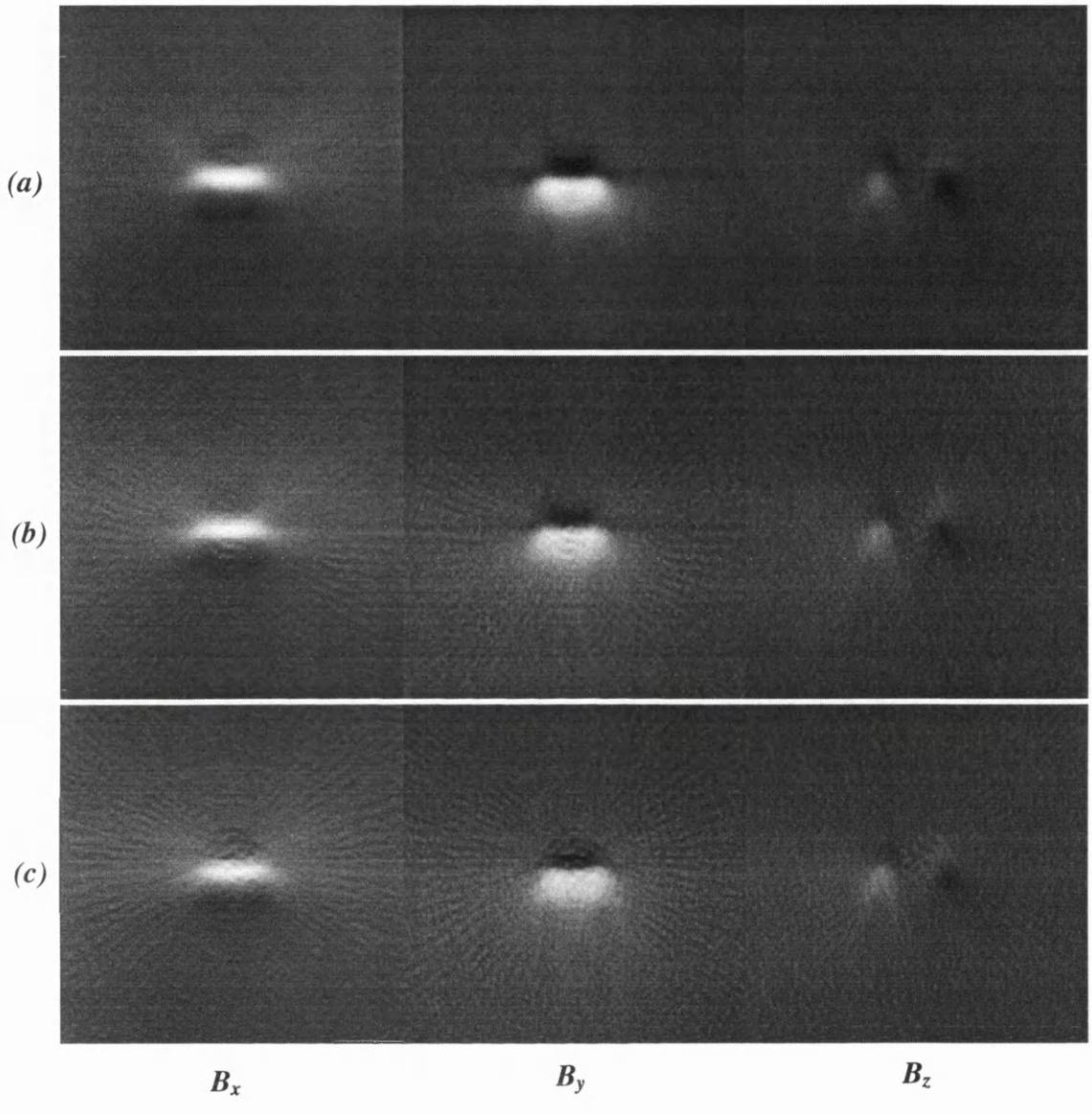

Fig. 7.9. *Field components of Tanba thin film head reconstructed by: (a) the ART, (b) the RTM using the tangential component of the deflection data and (c) using the normal component of the deflection data as shown in Fig. 7.5.*

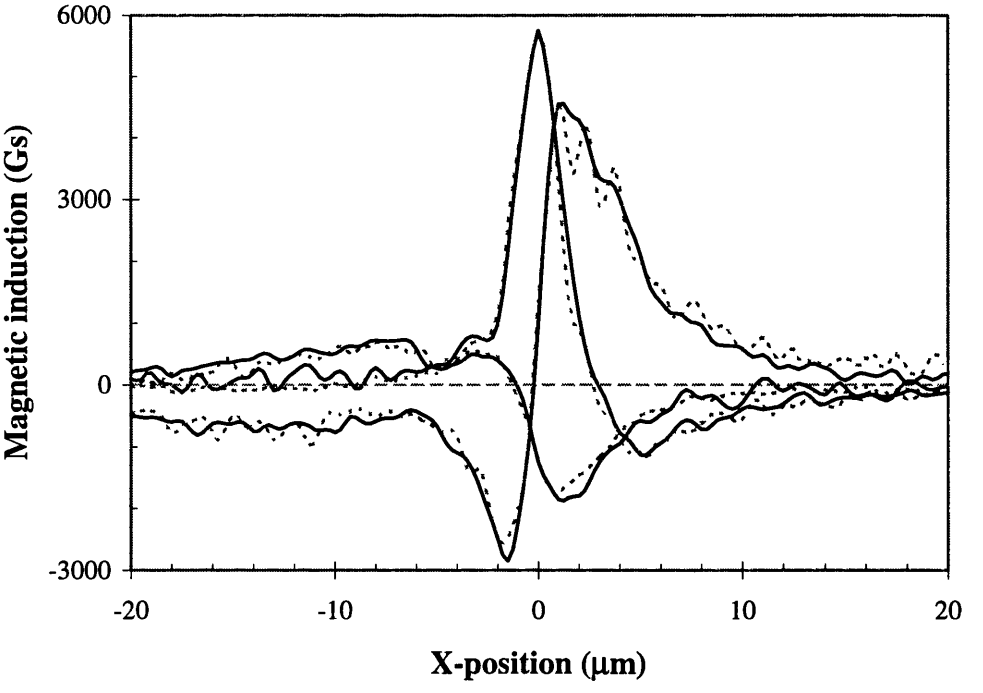

Fig. 7.10. *Comparison of the reconstruction results between the ART (solid lines) and the RTM (dot lines).*

References

Chapman, J. N. (1984), *J. Phys. D: Appl. Phys.* **17**, 623.

Chapman, J. N., I. R. McFadyen and S. McVitie (1990), *IEEE Trans. Magn.* **26**, 1506.

Chapter 8

Conclusions and future work

Electron beam tomographic reconstruction methods and their application in the study of recording head fields have been discussed in this thesis. The main body of the work described the development of the algebraic reconstruction technique (ART) for the study of micromagnetic stray fields by means of the electron beam tomography and the utilisation of the differential phase contrast (DPC) mode of Lorentz microscopy for the experimental investigations of the inductive recording head fields. The computer simulations and the experimental reconstruction results have given an insight into the nature of the micromagnetic stray field structure and extended progress in experimental analysis of recording head fields.

Among the experimental techniques of magnetic stray field measurement, the electron beam has been proved to be the most suitable probe. Electron probe techniques can provide sub-micron spatial resolution and have the potential to achieve even higher resolution than currently demonstrated. The DPC mode of Lorentz microscopy can provide quantitative information on the integrated stray field distribution and permit us to acquire the data sets necessary for the determination of the three dimensional recording head fields using the electron beam tomography. The modified JEOL 2000FX (S)TEM with its magnetic-field-free objective lens is capable of a spatial resolution of ~50 nm and is a suitable instrument to realise the required experimental arrangement.

The magnetic vector field tomographic methods of the ART and the RTM were described in chapter 3. The nature of the ART allows it to be applied to any continuous or non-continuous stray field distribution and the reconstruction can be performed with projections covering less than the full rotation range of 180°. The major advantage of the RTM is that each of the orthogonal input data sets allow independent determination of all three components of the reconstructed field and therefore provides a direct evaluation of the consistency of the experimental input data. Utilising computer

simulations of the field from a model recording head, the performance of our ART tomography program was investigated and compared with the RTM in chapter 4. It is confirmed by these simulations that the ART program can provide reconstruction of recording head fields with satisfactory accuracy and rapid convergence even when the reconstructed field has very large gradient and magnitude compared to the actual stray field generated by production recording heads. Reconstructions of the model thin film head field using ART for different reconstruction parameters suggest that 180° rotation angle and 36 different angular positions are a good compromise for both the ART and the RTM tomography programs. However, with reduction of the rotation angle to 120°, the ART could still produce acceptable reconstruction. In practice the field reconstruction may have to be performed from truncated input data sets (i.e. the DPC intensity at the line scan extreme are not negligible). However computer simulation shows that this has a relatively small effect on the major features of the field distribution, but larger background noise around the periphery of the reconstruction area may be present.

In chapter 5 the experimental investigations of the stray fields from inductive thin film heads were discussed. The investigations were limited to the dc characteristics of the stray field due to the present implementation of DPC Lorentz microscopy. The reconstruction of the stray field distribution near the polegap was made possible by a novel method of mounting the thin film head for data collection, which allows the field reconstruction to be conducted on a plane at ~0.25 μm from the polegap but at a small angle of 5° to the ABS. Stray field reconstruction at a closer distance to the ABS would be possible if larger image frame memory was available. The 3D reconstruction results of the stray field in the polegap region can be used as the verification of predications made by finite element methods, which are commonly used in the recording industry for inductive element design purposes. Since in disk recording the head-to-media spacing is approaching 25 nm to 50 nm, it becomes very important to understand the influence of local micromagnetic structure on the stray fields. It has been shown that experimental reconstruction exhibit field features which may reflect the local domain structure. The stray field behaviour of the average longitudinal and vertical field components could be studied from the DPC image with the electron beam incident along the head gap

direction and the field leakage around the poles has been investigated. It is believed that this is the first time such information has been open to experimental investigation.

The stray fields from MIG/ferrite and laminated alloy film tape heads have been investigated in chapter 6. The 3D reconstruction of the stray fields produced quantitative information on the field distributions along the relatively large head gap dimensions and the field gradients along the media movement direction. For the MIG head there is a secondary gap effect arising from head design/manufacturing; it is suggested by the experimental results that DPC Lorentz microscopy is the most suitable tool to observe this effect and the development of the secondary gaps as a function of the driving current has been studied. Along the head gap direction, the saturation and the remanence effects of the integrated writing field from the laminated alloy film tape heads were investigated. The experimental results obtained served to verify the results from the electrical characterisation of the recording head fields.

The calibration method for the contrast of the DPC image was described in chapter 7. Since the actual contrast in the DPC image is associated with the specific lens set up, the calibration has to be performed in-situ as part of the DPC experiment. The high resolution x-ray analysis function of the Link-system, which controls the scanning unit and DPC image acquisition, provides the possibility to quantify the actual electron beam deflection at certain point(s) in the DPC image. The results show very good agreement with the theoretical analysis of the detector response. Using the calibration absolute values of the recording head field are made available.

For further studies of recording head fields, improved spatial resolution and consequently a reconstruction distance closer to the head surface must be given high priority. This is required by the ever present desire for greater areal density of information storage and the continuously decreasing head-to-media spacing. The stray field behaviour at such a microscopic distance to the poletip will certainly be affected by the local domain structure in the poles. A better understanding of the stray field behaviour and its relation to the micromagnetic structure may be possible by carrying out domain studies in parallel with the stray field tomography. Attempts to investigate the domain structure and domain wall dynamics by backscattered electron imaging have already been carried out on the P2 pole of the thin film head by the author, but have not been included in this thesis. It appeared that the backscattered electron signal was

unlikely to be able to provide sufficient spatial resolution due to the nature of contrast formation. An alternative approach would be to use spin polarised SEM, but it would be necessary to ensure that the pole surface(s) were completely free of any contamination.

In any recording system the performance of both the transducer to read/write the data and the medium which stores the data are crucial. In the case of the latter no absolute determination of the magnetisation distribution associated with the written tracks has yet proved possible; electron beam tomography might be able to provide this information-certainly its applicability would be well worthy of investigation.

Appendix One dimensional dc response of the annular quadrant DPC detector

This section describes the derivation of equation set (7.1). Details of the detector geometry and the definition of the detector parameters have been introduced in section 7.2. Based on the assumption that the electron intensity is uniformly distributed on the detector plane, the one dimensional dc response $I(k_r)$ of the annular quadrant DPC detector can be obtained from signal subtraction between opposite segments. There are three possible electron beam deflection situations which divide the response curve into three regimes.

(I). $k_r \leq 1-K$

The information carrying signal arises from the difference of the electron intensity on the opposite segments (the shaded areas) as shown in Fig. A.1.

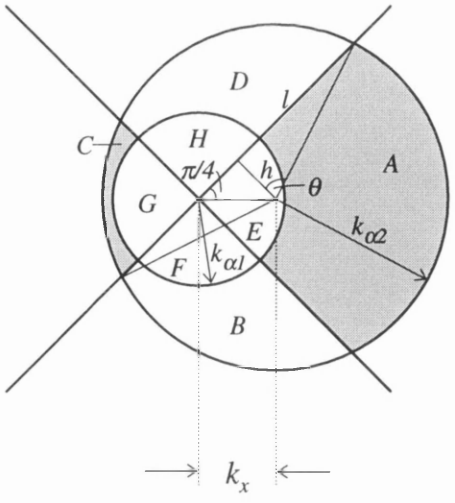

k_x : one-dimensional electron beam deflection.

$k_{\alpha 1}$: radius of the inner circle of the detector.

$k_{\alpha 2}$: radius of the bright field core.

$k_r = k_x / k_{\alpha 2}$: normalised spatial frequency.

$K = k_{\alpha 1} / k_{\alpha 2}$: detector parameter.

A, B, C, D, E, F, G, H : areas in each segments covered by the bright field core.

Fig. A.1. $k_r \leq 1-K$ or $k_x \leq k_{\alpha 2} - k_{\alpha 1}$

$$I(k_r) = A - C$$

$\because$ $\quad E = F = G = H \quad$ *and* $\quad B = D$

$\therefore$

$$\begin{aligned} A - C &= (A + E) - (C + G) \\ &= \pi k_{\alpha 2}^2 - (C + G + H + D) - (B + F + G + C) \\ &= \pi k_{\alpha 2}^2 - 2SA \end{aligned}$$

in which SA is the area of the sector and is given by

$$SA = \theta k_{\alpha 2}^2 - \frac{1}{2} \times 2l \times h$$

where

$$h = k_x \sin\frac{\pi}{4} = \frac{k_x}{\sqrt{2}}$$

$$l = \sqrt{k_{\alpha 2}^2 - h^2} = \frac{k_{\alpha 2}}{\sqrt{2}} \sqrt{2 - \left(\frac{k_x}{k_{\alpha 2}}\right)^2}$$

$$\theta = \tan^{-1}\frac{l}{h} = \tan^{-1}\left(\frac{k_{\alpha 2}}{k_x}\sqrt{2 - \left(\frac{k_x}{k_{\alpha 2}}\right)^2}\right)$$

$\therefore$

$$SA = k_{\alpha 2}^2 \tan^{-1}\left[\frac{k_{\alpha 2}}{k_x}\sqrt{2 - \left(\frac{k_x}{k_{\alpha 2}}\right)^2}\right] - \frac{k_x k_{\alpha 2}}{2}\sqrt{2 - \left(\frac{k_x}{k_{\alpha 2}}\right)^2} \qquad \text{(A.1)}$$

thus

$$I(k_r) = A - C = k_{\alpha 2}^2 \left\{ \pi - 2\tan^{-1}\left[\frac{k_{\alpha 2}}{k_x}\sqrt{2-\left(\frac{k_x}{k_{\alpha 2}}\right)^2} \right] + \frac{k_x}{k_{\alpha 2}}\sqrt{2-\left(\frac{k_x}{k_{\alpha 2}}\right)^2} \right\}$$
$$= k_{\alpha 2}^2 \left[\pi - 2\tan^{-1}\frac{\sqrt{2-k_r^2}}{k_r} + k_r\sqrt{2-k_r^2} \right] \qquad \text{(A.2)}$$

(II). $1 - K < k_r \leq 1$

The DPC signal intensity is proportional to the shaded area as shown in Fig.A.2.

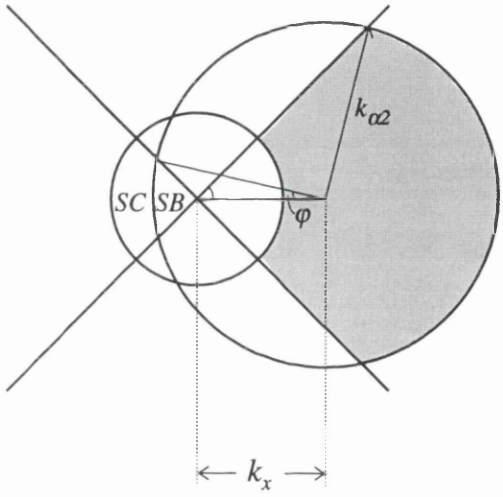

Fig. A.2. $1 - K < k_r \leq 1$ or $k_{\alpha 2} - k_{\alpha 1} < k_x \leq k_{\alpha 2}$

$$I(k_r) = \pi k_{\alpha 2}^2 - 2SA - SC$$

in which *SA* is given by equation (A.1) and

$$SC = \frac{\pi}{4}k_{\alpha 1}^2 - SB$$

and

$$SB = \varphi k_{\alpha 2}^2 - k_{\alpha 2} \cdot k_x \cdot \sin\varphi$$

where φ is determined by

$$\frac{\sin 3\pi/4}{k_{\alpha 2}} = \frac{\sin\left(\pi/4 - \varphi\right)}{k_x}$$

$$\therefore \qquad \varphi = \frac{\pi}{4} - \sin^{-1}\left(\frac{k_x}{\sqrt{2}k_{\alpha 2}}\right)$$

thus

$$SB = k_{\alpha 2}^2\left[\frac{\pi}{4} - \sin^{-1}\left(\frac{k_x}{\sqrt{2}k_{\alpha 2}}\right)\right] - \frac{k_x k_{\alpha 2}}{\sqrt{2}}\left[\cos\cdot\sin^{-1}\left(\frac{k_x}{\sqrt{2}k_{\alpha 2}}\right) - \frac{k_x}{\sqrt{2}k_{\alpha 2}}\right]$$

$$I(k_r) = k_{\alpha 2}^2\left[\pi - 2\tan^{-1}\frac{\sqrt{2-k_r^2}}{k_r} + k_r\sqrt{2-k_r^2} - \frac{\pi}{4}(1+K^2) - \frac{k_r^2}{2} + \sin^{-1}\frac{k_r}{\sqrt{2}} + \frac{k_r}{\sqrt{2}}\cos\cdot\sin^{-1}\frac{k_r}{\sqrt{2}}\right]$$

(A.3)

(III). $k_r > 1$

$$I\left(k_r\right) = \pi k_{\alpha 2}^2 - 2SA - SD$$

where *SA* is again given by equation (A.1) and

$$SD = \frac{\pi}{4}k_{\alpha 1}^2 - SE$$

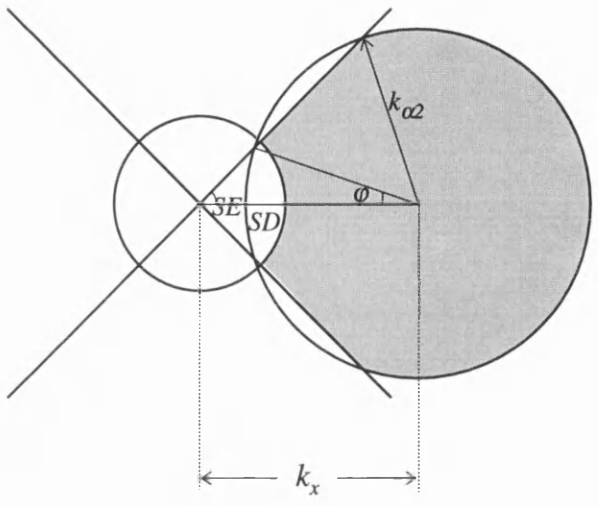

Fig. A.3. $k_r > 1$ or $k_x > k_{\alpha 2}$

in which

$$SE = k_x \cdot k_{\alpha 2} \cdot \sin\varphi - \varphi k_{\alpha 2}^2$$

φ is defined by

$$\frac{\sin \pi/4}{k_{\alpha 2}} = \frac{\sin\left(3\pi/4 - \varphi\right)}{k_x}$$

hence

$$\varphi = \frac{3\pi}{4} - \sin^{-1}\frac{k_r}{\sqrt{2}}$$

$\therefore$ $$SE = k_{\alpha 2}^2\left[\frac{k_r}{\sqrt{2}}\cos\sin^{-1}\frac{k_r}{\sqrt{2}} - \frac{k_r^2}{2} - \frac{3\pi}{4} + \sin^{-1}\frac{k_r}{\sqrt{2}}\right]$$

thus

$$I(k_r) = k_{\alpha 2}^2 \left[\pi - 2\tan^{-1}\frac{\sqrt{2-k_r^2}}{k_r} + k_r\sqrt{2-k_r^2} - \frac{\pi}{4}K^2 - \frac{k_r}{\sqrt{2}}\cos\sin^{-1}\frac{k_r}{\sqrt{2}} + \frac{k_r^2}{2} + \frac{3\pi}{4} - \sin^{-1}\frac{k_r}{\sqrt{2}} \right]$$

(A.4)

Equations (A.2), (A.3) and (A.4) are the one dimensional dc response of the annular quadrant DPC detector.